FROM CLASSICAL TO QUANTUM STOCHASTIC RESONANCE

Von der Fakultät 8 Mathematik und Physik der
Universität Stuttgart zur Erlangung der
Würde eines Doktors der Naturwissenschaften (Dr. rer. nat.)
genehmigte Abhandlung.

Vorgelegt von

Gregory MCMURTRIE
aus Alicante, Spain

Hauptberichter:	Prof. Dr. S. Loth
Mitberichter:	Prof. Dr. T. Pfau
Tag der mündlichen Prüfung:	07.09.2021

Institut für Funktionelle Materie und Quantentechnologien
der Universität Stuttgart, Deutschland
2022

The true delight is in the finding out rather than in the knowing.

Isaac Asimov

CONTENTS

SUMMARY

The open quantum system presented by atomic spins on surfaces is a unique platform to investigate the interplay between stochastic and deterministic behavior. This work investigates this interplay at the transition from classical to quantum behavior in tailored magnetic nanostructures. The structures are assembled with Fe atoms on a Cu_2N surface grown on Cu(100) by using atom manipulation with a cryogenic-temperature scanning tunneling microscope. The spin state of the structures can be resolved with a spin-polarized tip, allowing their dynamic response to be measured. The stochastic evolution of the spin states is brought into a resonant regime by means of either a modulated exchange field or a modulated voltage applied with the tip. Undergoing this stochastic resonance yields insight into how these structures interact with their environment, with clear signatures of classical, semi-classical and quantum behavior being observed. This work sets the stage for a new way of interacting with incoherently evolving spin systems, by synchronizing their dynamics, and tailoring their interaction with their environment.

ZUSAMMENFASSUNG

Das offene Quantensystem von Atomspins auf Oberflächen ist eine einzigartige Plattform, um das Zusammenspiel zwischen stochastischem und deterministischem Verhalten zu untersuchen. Diese Arbeit untersucht dieses Zusammenspiel am Übergang vom klassischen zum Quantenverhalten in maßgeschneiderten magnetischen Nanostrukturen. Die Strukturen werden mit Fe-Atomen auf einer auf Cu(100) aufgewachsenen Cu_2N-Oberfläche durch Atommanipulation mit einem Rastertunnelmikroskop bei kryogener Temperatur aufgebaut. Mit einer spinpolarisierten Spitze lässt sich der Spinzustand der Strukturen auflösen und so deren dynamisches Verhalten messen. Die stochastische Entwicklung der Spinzustände wird entweder durch ein moduliertes Austauschfeld oder eine an der Spitze angelegte modulierte Spannung in einen resonanten Zustand gebracht. Wenn man sich dieser stochastischen Resonanz unterzieht, erhält man Einblicke in die Wechselwirkung dieser Strukturen mit ihrer Umgebung, wobei klare Signaturen von klassischem, semiklassischem und Quantenverhalten beobachtet werden. Diese Arbeit bereitet die Bühne für eine neue Art der Interaktion mit sich inkohärent entwickelnden Spinsystemen, indem ihre Dynamik synchronisiert und ihre Interaktion mit ihrer Umgebung angepasst wird.

1

INTRODUCTION

Randomness, stochasticity, chance. We have many different words for it, and at first glance it may seem like a relatively straightforward concept. Rolling a dice is a game of chance, the outcome is unknown before you roll it. Dropping a ball is not, it will always accelerate towards the floor, as Newton described [1]. Yet there is a rich degree of grey between these black and white situations. The Brownian motion [2] of each molecule in a fluid is random, yet macroscopic quantities such as pressure and temperature can be readily defined. Likewise, through careful annealing cycles [3] one can push the random domains in an amorphous crystal towards macroscopic periodicity.

We have tried to chase chance from both ends, trying to generate order out of the stochasticity of truly random systems, and attempting to create randomness from those that are deterministic. In an example of the latter, huge amounts of effort have been made to try and create random cryptographic nonces for use in secure communication [4], yet the intrinsically deterministic nature of computers has proven hard to overcome. Pseudorandom number generators have stepped in to provide an approximation of true randomness, yet von Neumann put it best: "Anyone who considers arithmetical methods of producing random digits is, of course, in a state of sin." [5]

If anything, creating order out of chaos has an even broader relevance. In the world of finance, patterns are the name of the game; in any quant shop there is no short supply of analysts who will claim to have the perfect arbitrage opportunity, yet most are likely attributing signal to the noise. Indeed, over a 40 year period the return from simply buying and holding a set of securities was within the margin of error for the return in a number of complex market timing strategies. [6] The markets are simply taking a random walk. [7]

1

So are deterministic and random behaviors at odds with one another? Can we have both? Often the answer is a matter of scale, where microscopic randomness yields macroscopic order, or the structured atomic scale yields unpredictable mesoscopic disorder. For example, there are a myriad of stochastic processes governing the earth's temperature dynamics, yet glaciation occurs with a startling regularity, yielding the infamous 100,000 year problem. [8] Similarly, each individual neuron fires stochastically, yet the ensembles of neurons in the brain can give rise to a synchronized collective response. [9] In these systems, random and deterministic character compete. Notably, in both the above systems and many others [10–13], a phenomenon called stochastic resonance can be used to probe the nature of this competition.

Stochastic resonance is a process through which a stochastically switching system can become synchronized to an external drive. [14] Notably, the drive does not attempt to overwhelm the stochastic noise in order to introduce this synchronized response, but rather cooperates with it. For specific conditions, the random noise effectively amplifies the drive, yielding the resonance-like behavior. Described as "helpful randomness" [13], the noise is no longer a hindrance to measurement, but rather an asset.

There is no fundamental reason as to why stochasticity and periodicity cannot coexist, which is what this thesis intends to shed some light on, by means of stochastic resonance experiments. We carry these experiments out using spin-polarized scanning tunneling microscopy and atom manipulation to investigate the interplay between randomness and predictability at the atomic scale. The quantum world that dictates the rules at this scale is a fruitful playground for investigations into stochasticity, as the fundamental interactions are statistical. Atom manipulation in particular allows specific atomic configurations to be generated, which present a unique coupling to both their environment and amongst the constituent atoms, and thereby a unique stochastic response. The structures can be designed such that they are more susceptible to either quantum or classical noise sources stemming from electron-spin scattering with their environment. Individually addressing these structures with the scanning tunneling microscope and driving them with either a harmonic bias voltage or magnetic field modulation promotes stochastic resonance. The stochastic resonance serves as a quantitative probe of the respective noise noise sources, giving direct access to the stochastic properties of these noisy spin systems.

This thesis begins with a discussion of open quantum systems, namely magnetic spins on surfaces. The theory of quantum stochastic resonance is then extended to model atomic spin systems, and its applications are discussed. Chapter 3 is an investigation of a nine atom nanostructure which undergoes classical stochastic resonance. In Chapter 4 a five atom structure which straddles the crossover between the classical and semi-classical noise regime is brought to stochastic resonance. Finally, in Chapter 5 a single atom is investigated, which can be brought into

both quantum stochastic resonance in a temperature-agnostic regime, and into semi-classical stochastic resonance in a temperature dependent regime. Overall, this thesis brings understanding into how the dynamic evolution of all these spin systems can be driven to different degrees of stochastic behavior. This yields insight into how these structures couple to their environment, as well as unlocking new ways of interacting with spins on surfaces.

Looking forward, stochastic resonance could not only serve as a spectroscopic tool to measure dynamic behavior, but drive non-equilibrium occupation of higher energy spin states, unlocking a path to resolving novel intra-structure dynamics. Additionally, in the limit of strong spin-bath coupling, stochastic resonance experiments could also be used to reveal the onset of non-Markovian dynamics.

REFERENCES

[1] I. Newton, *Mathematical Principles of Natural Philosophy* (Royal Society, London, 1687).

[2] A. Einstein, *Über die von der molekularkinetischen Theorie der Wärme geforderte Bewegung von in ruhenden Flüssigkeiten suspendierten Teilchen,* Ann. d. Phys. **322**, 549 (1905).

[3] M. Wakagi, H. Fujiwara, and R. W. Collins, *Real time spectroscopic ellipsometry for characterization of the crystallization of amorphous silicon by thermal annealing,* Thin Solid Films **313-314**, 464 (1998).

[4] S. Sharma, S. Jain, and B. R. Chandavarkar, *Nonce: Life Cycle, Issues and Challenges in Cryptography,* in *ICCCE 2020*, edited by A. Kumar and S. Mozar (Springer Singapore, Singapore, 2021).

[5] J. von Neumann, *Various techniques used in connection with random digits,* Nat. Bureau Standards **12**, 36 (1951).

[6] M. C. Jensen and G. A. Benington, *Random Walks and Technical Theories : Some Additional Evidence Source,* The Journal of Finance **25**, 469 (1970).

[7] M. Jensen, F. Black, and M. Scholes, *The Capital Asset Pricing Model: Some Empirical Tests,* in *Studies in the theory of capital markets* (Praeger Publishers Inc., 1972).

[8] R. Benzi, G. Parisi, A. Sutera, and A. Vulpiani, *Stochastic resonance in climatic change,* Tellus **34**, 10 (1982).

[9] B. J. Gluckman, T. I. Netoff, E. J. Neel, W. L. Spano, M. L. Spano, and S. J. Schiff, *Stochastic Resonance in a Neuronal Network from Mammalian Brain,* Physical Review Letters **77**, 4098 (1996).

[10] R. L. Badzey and P. Mohanty, *Coherent signal amplification in bistable nanomechanical oscillators by stochastic resonance,* Nature **437**, 995 (2005).

[11] I. Y. Lee, X. Liu, B. Kosko, and C. Zhou, *Nanosignal Processing: Stochastic Resonance in Carbon Nanotubes That Detect Subthreshold Signals,* Nano Letters **3**, 1683 (2003).

[12] G. Matteucci, *A study of the climatic regimes of the Pleistocene using a stochastic resonance model,* Climate Dynamics **6**, 67 (1991).

[13] M. D. McDonnell and D. Abbott, *What is stochastic resonance? Definitions, misconceptions, debates, and its relevance to biology,* PLoS Computational Biology **5** (2009).

[14] L. Gammaitoni, P. Hänggi, P. Jung, and F. Marchesoni, *Stochastic resonance,* Reviews of Modern Physics **70**, 223 (1998).

2

THEORETICAL BACKGROUND

2.1. INVESTIGATING OPEN QUANTUM SYSTEMS

Open quantum systems [1] are, by nature of their coupling to their surroundings, the most common type of quantum system by far. One could argue that they are indeed the only form of quantum system present in nature [2], as it has taken hundreds of years of technical advances to be able to sufficiently isolate a quantum system from its environment such that it evolves independently of the myriad of scattering processes presented by the world around it.

A single magnetic atom on a metallic surface is an elegant example of one such quantum system [3]. Under the right conditions, the atom can retain its magnetic moment; a partially quenched orbital moment defines the magnetic moment's orientation via spin-orbit coupling while its magnitude is governed by the electron spin moment. An external magnetic field can lift the degeneracy of the atom's discrete spin states, and interaction with electrons present in the bath of the metal surface provides a means of scattering, and thereby transitioning, between these magnetic states.

However, transitions between the states occur infrequently enough that the spin has time to reach equilibrium between subsequent transitions [4], defining the Markov property for the spin. That is, subsequent transitions of the spin state depend only on the current state, not on any past interactions. In a two-state picture of the spin, this defines a Markov chain as shown in Figure 2.1. Considering only the two lowest-lying states in energy is an approximation, but for the purposes of the transition rates it is often sufficient to describe all of the necessary statistics. Depending on the transition probabilities between the states, one can expect either fast or slow magnetization switching, which will reflect how the system couples to its environment.

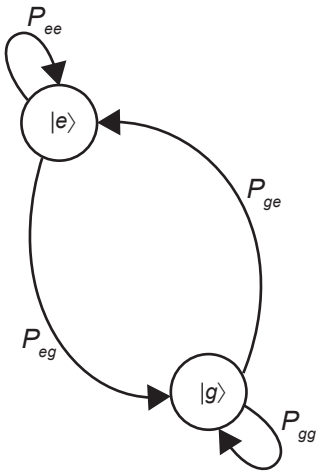

Figure 2.1. The Markov chain of a spin system with two magnetic states scattering with its environment. $|g\rangle$ is the ground state, $|e\rangle$ is the excited state, P_{ij} is the transition probability from state i to state j.

The scanning tunneling microscope [5] (STM) is naturally suited for the investigation of open quantum systems, particularly that of atoms and atomic structures coupled to a bath. It is by definition an extremely localized probe [6], and provides a means of both interacting with [7, 8] and measuring entities on surfaces. The development of spin-polarized STM [9, 10] added magnetic contrast to the capabilities of the microscope, enabling a host of experiments on magnetic entities on surfaces [11–15]. The Cu_2N [16] surface has proven a particularly fruitful playground for the investigation of magnetic nanostructures and molecules [17–21]. Structures on the surface can be interacted with via the bias voltage applied [22] as well as by a local exchange field generated by the spin-polarized tip [8], and exhibit spin lifetimes ranging from nanoseconds [23] to hours [24].

A time trace of a real open quantum system, an Fe-atom on the N-site[1] of a Cu_2N monolayer grown on Cu(100) is shown in Figure 2.2, measured with a spin-polarized tip in an STM. Two discrete states can be clearly identified, with randomly varying amounts of time spent in each. To investigate the probabilities governing transitions between the two states, a histogram can be generated (Figure 2.3), which shows the distribution of switching times. The distribution is broad, with a clear exponential behavior; the ground state and excited state each sample a Poisson distribution with a different mean, as can be seen by the good agreement with the fit curves.

[1] For details see Chapter 5.

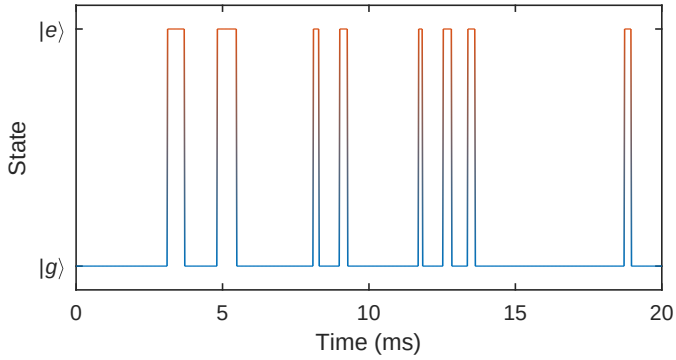

Figure 2.2. Transitions between the ground state $|g\rangle$ (blue) and excited state $|e\rangle$ (red) of a single Fe atom on the N-site of a Cu_2N monolayer grown on Cu(100). $V_{dc} = 15$ mV, $B_z = 500$ mT, $V_{set} = 15$ mV, $I_{set} = 3$ nA, $T = 0.5$ K.

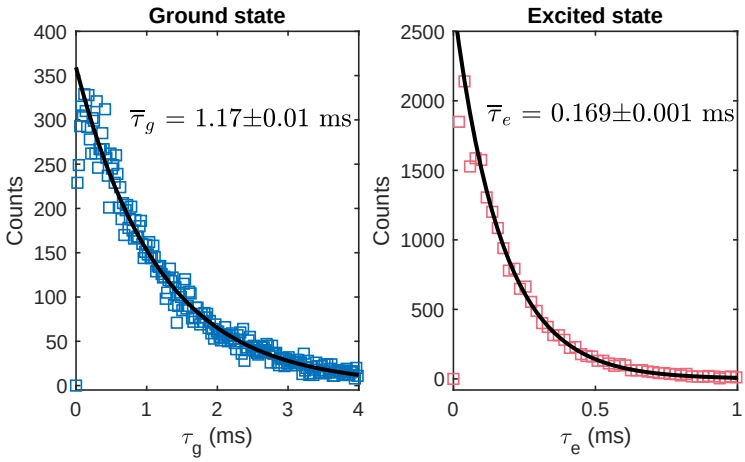

Figure 2.3. Occupation time statistics for the ground (blue) and excited state (red) of a single Fe atom on the N-site of a Cu_2N monolayer grown on Cu(100), with least-square fits to an exponential function (Equation 2.1, black). $V_{dc} = 15$ mV, $B_z = 500$ mT, $V_{set} = 15$ mV, $I_{set} = 3$ nA, $T = 0.5$ K.

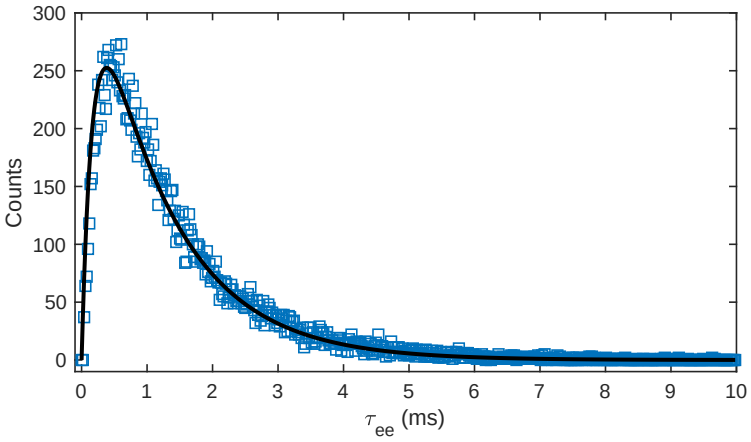

Figure 2.4. Counts of the time between two excitation events t_{ee} (one full cycle of excitation and relaxation) for a single Fe atom on the N-site of a Cu_2N monolayer grown on Cu(100), with least-square fit to a hypoexponential curve (Equation 2.2, black, using the time constants from Figure 2.3). $V_{dc} = 15$ mV, $B_z = 500$ mT, $V_{set} = 15$ mV, $I_{set} = 3$ nA, $T = 0.5$ K.

The Poisson distribution which describes the probability of remaining in the i^{th} state for a given amount of time τ_i is:

$$P(\tau_i) = ce^{\frac{-\tau_i}{\overline{\tau}_i}}, \tag{2.1}$$

where $\overline{\tau}_i$ is the characteristic parameter of the distribution, the mean residence time.

Of course, excitation and relaxation are not independent processes, they occur one after another. An excitation will always follow a relaxation, and vice versa. As such, rather than looking at the two processes independently, one can instead model their switching statistics using a hypoexponential distribution (Figure 2.4). A hypoexponential distribution describes the probability of two or more consecutive Poisson processes occurring. For an excitation that samples the Poisson distribution with characteristic $\overline{\tau}_g$ followed by a relaxation which samples the Poisson distribution with characteristic $\overline{\tau}_e$ the hypoexponential distribution is:

$$P(\tau_{ee}) = c\left[\frac{e^{\frac{\tau_{ee}}{\overline{\tau}_e}}}{\overline{\tau}_g - \overline{\tau}_e} + \frac{e^{\frac{\tau_{ee}}{\overline{\tau}_g}}}{\overline{\tau}_e - \overline{\tau}_g}\right]. \tag{2.2}$$

This hypoexponential function describes the times between two excitation events τ_{ee}, and one can see that it effectively reproduces the switching time distribution measured on the Fe atom. A system governed by such a distribution is

also sometimes said to be exhibiting "random telegraph noise" [25], as they mimic the short and long bursts of signal of a telegraph message.

It is worth noting there is a third probability distribution which we can encounter, the Erlang distribution. This distribution is similar to the hypoexponential distribution, but for the special case of two consecutive Poisson processes with equal characteristic time constants $\overline{\tau}_g = \overline{\tau}_e$, and has the form:

$$P(\tau_{ee}) = cte^{\frac{\tau_{ee}}{\overline{\tau}_g}}. \tag{2.3}$$

2.2. STOCHASTIC RESONANCE

What makes the switching of a spin stochastic? In other words, why is spin state occupation a random variable? Fundamentally, this is because transitions between the spin states are probabilistic quantum transitions. The probability to make a transition in a given time is determined by a transition matrix element between two spin states of the same nanostructure. In the context of spins on surfaces, this transition matrix element is calculated by an exchange scattering process between an electron and the spin of the atom. At this level, transitions that completely reverse the magnetic moment of the atom with just one scattering electron are possible, because of small but finite matrix elements between the states. These seemingly forbidden processes have been termed "tunneling of the magnetization" [26], and will be the primary focus of this thesis. They are intrinsically statistical.

There are different scattering processes which depend on this matrix element, we define these different processes as "noise sources", as they too will be "noisy". They result in a transition rate between ground and excited state, which is our observable. As well as a direct tunneling event between two states, there can also be indirect transitions by means of a higher energy intermediary state. Notably, transitions via higher energy intermediary state, i.e. "over" the anisotropy barrier, will depend strongly on the temperature, while direct tunneling is temperature agnostic. The distinct temperature dependence here is critical, as it allows two distinct types of processes (noise sources) to be defined. Transition rates that trend to zero as temperature goes to zero are considered to result from classical processes (classical noise source), while transition rates that remain finite as temperature goes to zero are termed quantum (quantum noise source).

Note that the scattering processes themselves can also have intrinsic sources of stochasticity. In particular, a thermal bath would still result in random spin state switching for a unit matrix element. The energies of the electrons in the bath are not constant, but rather distributed according to the Fermi-Dirac distribution [27, 28]. Coupling to a thermal bath is a unique component of classical stochastic resonance, and will be explored in detail in Chapter 3.

Historically, much work has often focused on "averaging out" this randomness, and therefore characterized open quantum systems using their average spin lifetime. However, the characterization of both spin ensembles and individual spins by their average spin lifetime omits information about the nature of the stochasticity driving the switching events. Two spins with the same average spin lifetime could be subject to wildly different scattering environments, gaining information about the scattering could only be derived by looking at the full distribution of the switching events. As an example, coherently switching spins in an ESR experiment [15] exhibit a sharp peak at their average Larmor frequency, with a width that characterizes the degree of coherence. Alternatively, a thermally driven spin switching due to coupling with a hot bath will exhibit a broad Poisson distribution in spin lifetime, mirroring the broad range of temperatures in a Boltzmann distributed bath. One prominent mechanism which can modify switching event distribution is that of stochastic resonance (SR)[29], which can be found in harmonically driven stochastic bistable systems with an inherent noise source[30–32]. SR is a widespread phenomenon, which can be observed in the periodicity of glaciation[29, 33], in the charge carrier dynamics of microstructure devices [34, 35], and even in the dynamic behavior of neurons[36]. SR harnesses the noise present in the system, be it quantum or classical, to induce a preferential switching synchronized to an external drive. By applying a modulation at the appropriate rate, SR can suggest an optimum path to the random variable, effectively adding a degree of predictability to the randomness.

In spin systems, there are two primary ways of modifying this randomness. One can change the matrix element itself, or one can change the attempt rate of the scattering process. The matrix element can be modified by changing an external parameter such as the applied magnetic field. The attempt rate can be modified by changing the applied voltage for inelastic scattering with tip electrons, or by changing the temperature of the substrate for scattering with thermal bath electrons; this is effectively modifying the noise power. This work will explore inducing stochastic resonance when a classical noise source is present, when a quantum noise source is present, as well as in a competing semi-classical crossover regime.

2.3. THEORETICAL FRAMEWORK

SR is a general phenomenon, here we will see how to apply it specifically to quantum systems. The seminal work of Coppersmith and Löfstedt [37, 38] established a theoretical framework for the modelling of quantum stochastic resonance. The theory can model the response of a finite-temperature two-state system to periodic driving using time-dependent transition rate theory. In this work, the model is extended to simulate the behavior of atomic spins and nanostructures, with the goal of describing the respective residence-time distributions of each system. There are two observable quantities that we are sensitive to: the time-dependent occupation of each state $n_a(t)$, and the time-dependent transition rate between each state

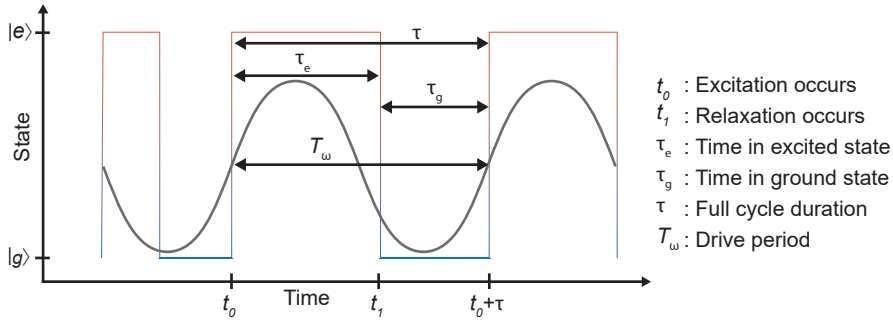

Figure 2.5. Schematic time trace showing the stochastic switching of the atom (blue $|g\rangle$ to red $|e\rangle$), the periodic drive (grey, period T_ω), with the relevant times indicated. In this example the period T_ω and the marked full cycle τ_{ee} are identical.

$W_{ab}(t)$. These are used as an input to the model in order to describe the broadband distribution of times between excitations as a function of different control parameters.

The model defines two transition rates, $W_{ge}(t)$ and $W_{eg}(t)$, which are the conditional probabilities to transition out of the ground state $|g\rangle$ and the excited state $|e\rangle$, given that the respective state is occupied. The time dependence of the transition rates is introduced by an external drive, and the transition rates are assumed to be periodic with the period T_ω of the drive. Given that the system is in a particular state, the chance that the system transitions out of the state in an infinitesimal time dt is given by the respective conditional probability multiplied by dt, i.e. $W_{ge}(t)dt$ if the system is in the ground state.

The quantity we want to model is $Q(\tau_{ee})$, the statistical distribution of τ_{ee} within a trace of the time-dependent state occupation. The distribution of τ_{ee} reflects the nature of the stochastic spin-state switching, with broadband Hypoexpoential character when the spin is switching fully randomly, and narrow-band peaked character when the spin is switching more deterministically. More specifically, $Q(\tau_{ee})$ can be used to determine the relationship between the duration of a full cycle τ_{ee}, where $\tau_{ee} = \tau_g + \tau_e$, and the duration of one period of the drive T_ω. In a fully deterministic, synchronized, system the duration of τ_{ee} would be completely locked to that of T_ω. A fully random system would exhibit no relationship whatsoever between T_ω and τ_{ee}. In intermediate cases, $Q(\tau_{ee})$ will peak at T_ω, as well as at higher multiples $2T_\omega$, $3T_\omega$, etc. For a schematic description see Figure 2.5. $Q(\tau_{ee})$ can be written as:

$$Q(\tau_{ee}) = N \int_{-\infty}^{\infty} dt_0 Z_{ge}(t_0) \int_{t_0}^{t_0+\tau_{ee}} dt_1 P_{eg}(t_1|t_0) P_{ge}(t_0+\tau_{ee}|t_1). \tag{2.4}$$

N is a normalization constant, $Z_{ab}(t)$ is the probability that a transition from state a to state b occurred at a time t, $P_{ab}(t_2|t_1)$ is the probability of leaving the state

a at time t_2 given that it was entered at time t_1. N can be fixed by imposing normalization, $\int_0^\infty d\tau_{ee} Q(\tau_{ee}) = 1$. First, an excitation occurs at a time t_0, followed by a relaxation at t_1, and a subsequent excitation at $t_0 + \tau_{ee}$. The duration of such a cycle is τ_{ee}. The first integral takes into consideration all of the different times the first excitation t_0 could occur, and the second integral takes into consideration all of the different times t_1 the relaxation could occur. The second integral is bounded by the total duration of the cycle being τ_{ee}. We now want to simplify this expression for $Q(\tau_{ee})$ such that it can be written in terms of our measured quantities $W_{ab}(t)$ and $n_a(t)$, the conditional transition rates and the time-dependent occupation.

The first piece of information that we can apply is the Markovian, and therefore periodic, nature of the transition rates. This allows a function $Y_{ab}(t^*)$ to be defined, which is the probability that state b was entered at a time t^* satisfying $t^* = t \mod T_\omega$:

$$Y_{ab}(t) = \sum_{m=-\infty}^{\infty} Z_{ab}(t + mT_\omega). \tag{2.5}$$

Here the * can be omitted because of the infinite sum. In other words, the probability to enter at a given time t relative to the drive is the sum of the probability to enter at time t, time $t + T_\omega$, time $t + 2T_\omega$, and so on. The function $Y_{ab}(t)$ is by definition periodic, that is, $Y_{ab}(t) = Y_{ab}(t + T_\omega)$, where T_ω is one period of the drive. It is also normalized such that $\int_0^{T_\omega} Y_{ab}(t) = 1$.

$Y_{ab}(t)$ can in turn be written in terms of the conditional probability $W_{ab}(t)$ by multiplying this probability by the time-dependent occupation of the respective state $n_a(t)$:

$$Y_{ab}(t) = W_{ab}(t) n_a(t). \tag{2.6}$$

This allows $Q(\tau_{ee})$ to be re-written as:

$$Q(\tau_{ee}) = N \int_0^{T_\omega} n_g(t_0) W_{ge}(t_0) \int_{t_0}^{t_0+\tau_{ee}} dt_1 P_{eg}(t_1|t_0) P_{ge}(t_0 + \tau_{ee}|t_1). \tag{2.7}$$

The first integral is now written in terms of our observables, we now proceed to re-write the second one. Moving now to the quantity $P_{ab}(t_2|t_1)$, the probability of leaving state a at time t_2 given that it was entered at time t_1. This can be written in terms of two sequential processes, first the system must remain in its current state until time t_2, and then it must make a transition in the time between t_2 and $t_2 + \delta t$. $A_a(t)$ is defined as the probability to remain in state a for a time t, which can be written as:

$$A_a(t + dt) = A_a(t)[1 - dt W_{ab}(t)], \tag{2.8}$$

i.e. to remain in state a for a time $t + dt$ it must first remain for a time t and then not make a transition in a time dt. A differential equation can then be written for A_a:

$$\frac{dA_a(t)}{dt} = -A_a(t) W_{ab}(t). \tag{2.9}$$

This equation can be solved using an integrating factor, yielding:

$$A_a(t) = e^{\int_0^t -W_{ab}(t^*)dt^*}. \tag{2.10}$$

We can use $A_a(t)$ to write $P_{ab}(t_2|t_1)$ in terms of $W_{ab}(t)$, as it can be expressed as the product between remaining in state a for the time between t_1 and t_2, followed by an excitation from a to b at time t_2:

$$P_{ab}(t_2|t_1) = W_{ab}(t_2)e^{-\int_{t_1}^{t_2} dt^* W_{ab}(t^*)}. \tag{2.11}$$

$Q(\tau_{ee})$ can now be written as:

$$Q(\tau_{ee}) = N\int_0^{T_\omega} dt_0 n_g(t_0)W_{ge}(t_0)\cdot \int_{t_0}^{t_0+\tau_{ee}} dt_1 W_{eg}(t_1)e^{-\int_{t_0}^{t_1} dt' W_{eg}(t')} W_{ge}(t_0+\tau_{ee})e^{-\int_{t_1}^{t_0+\tau ee} dt'' W_{ge}(t'')}. \tag{2.12}$$

This equation is an extension of the analogous equation 3.5 in [37], where the single integral which was used to calculate the residence time in a single state is now a double integral since here we are concerned about the probability of the full cycle time. It gives an analytic form to easily calculate the cycle time distribution from the time-dependent excitation rates and occupations, two quantities which can readily be measured using spin-polarized scanning tunneling microscopy.

2.4. CALCULATING CONDITIONAL PROBABILITIES

The conditional transition probabilities and the time-dependent occupation are the only inputs needed for the stochastic resonance model, which need to be determined experimentally from the measured transition rates. To calculate the transition rates, one treats the measured data as simply a series of times that the spin spent in a given state:

$$t = \{\tau_{g1}, \tau_{e1}, \tau_{g2}, \tau_{e2}, ..., \tau_{gN}, \tau_{eN}\}. \tag{2.13}$$

In other words, the spin was first in the ground state for a time τ_{g1}, then it was in the excited state for a time τ_{e1} and so on until the N^{th} cycle of excitation and relaxation. For the transition rates, however, the phase relationship between the modulation and the spin state occupation plays a critical role.

To obtain the transition rates, the full time trace of length t_{meas} is mapped to $\frac{t_{meas}}{T_\omega}$ segments where T_ω is the modulation period. By then defining M bins within T_ω, we can count how often the spin switching occurred in each of the M bins in each segment. c_{ai} is the number of transitions out of state a that occur in the i^{th}

bin of size $\frac{dt}{T_\omega}$ over the full measurement time t_{meas}, where $dt = \frac{T_\omega}{M}$. In other words, c_{ai} transitions occur in $\frac{1}{M}^{\text{th}}$ of the measurement time t_{meas}. This allows the discrete form of the time-dependent rates to be written as: $Y_{ab}(t)$:

$$Y_{ab}(i \cdot dt) = \frac{c_{ai}}{(\frac{t_{meas}}{M})} = c_{ai} \frac{M}{t_{meas}}. \tag{2.14}$$

$Y_{ab}(i \cdot dt)$ is then divided by the time-dependent occupation of state a: $n_a(i \cdot dt)$, which has also been binned in the same M bins, yielding the conditional transition rate:

$$W_{ab}(i \cdot dt) = \frac{Y_{ab}(i \cdot dt)}{n_a(i \cdot dt)}. \tag{2.15}$$

One could visualize this as a sort of "folding back" of the excitation events to a single period, where the subsequent division by occupation allows one to disentangle how frequently the spin is in a given state throughout one period of the modulation from the probability to make a transition at that time. For a sufficiently large M, $W_{ab}(t = i \cdot dt)$ can be linearly interpolated to yield the conditional transition rate at any arbitrary time within the period.

We now have a method of transforming a time trace showing state occupation to conditional transition rates. The rates, in turn, can then be used to simulate the excitation distribution $Q(\tau_{ee})$. To place these results into context, in the next section we look at how different transition rates can lead to different switching distributions.

2.5. ANALYTIC TRANSITION RATES

We begin with the simplest rate structure, that of a constant rate. Transitions are equally likely to occur at any point within the modulation period, and are equally likely to occur from ground to excited state as from excited to ground state. Figure 2.6 shows three different cases with constant rates. A constant rate means that the modulation has no effect on the resulting dynamics. In Panel A both the excitation rate and relaxation rate are constant and equal, $W_{ge}(t) = W_{eg}(t) = 10$ Hz. The corresponding time between excitation events (Panel D) reflects this, showing an Erlang probability distribution. The distribution peaks at $\overline{\tau}_g = \frac{1}{\overline{W}_{ge}(t)} = 0.1$ s, which is marked with a dotted line. In Panel B the relaxation rate is twice as fast as the excitation rate, which results in a hypoexponential distribution for the time between excitation events (Panel E). The peak is between $\overline{\tau}_e$ and $\overline{\tau}_g$ (each marked with a dotted line). In Panel C the relaxation rate is increased even further, to 100 Hz. Although still a hypoexponential distribution, the significantly different rates result in a line-shape that begins to resemble an exponential distribution instead. This is the natural limit of the hypoexponential distribution when one rate is much faster than the other, as eventually this will be indistinguishable from a process governed by only a single rate (the slower one) and an instantaneous rate (the fast one). Note

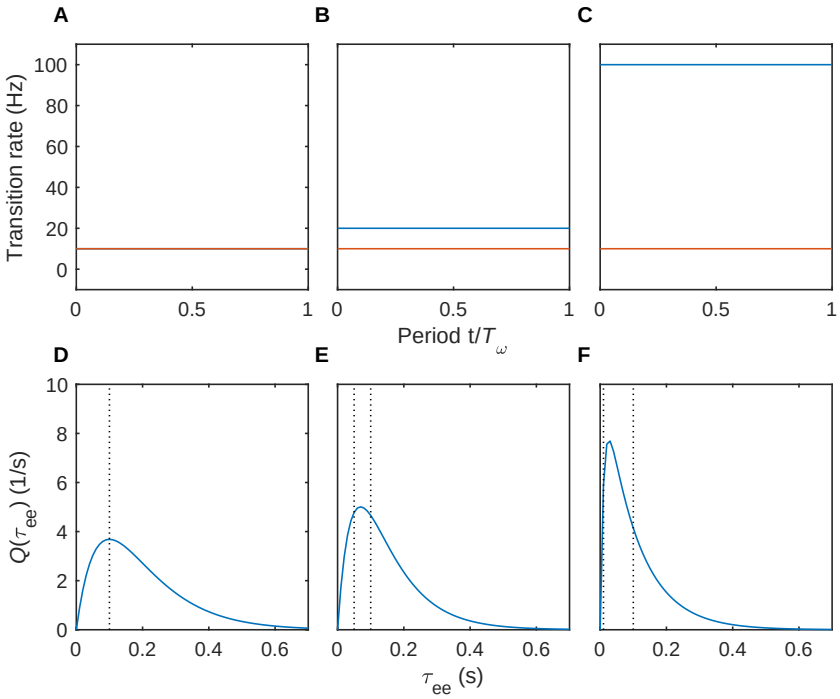

Figure 2.6. Relation between constant transition rates and switching distribution. (**A**) Constant excitation $W_{ge}(t)$ (red) and relaxation $W_{eg}(t)$ (blue) rates. $\overline{\tau}_e = \overline{\tau}_g = 0.1$ s. (**B**) Constant excitation rate $W_{ge}(t)$ (red) with $\overline{\tau}_g = 0.1$ s and constant relaxation rate $W_{eg}(t)$ (blue) with $\overline{\tau}_e = 0.05$ s. (**C**) Constant excitation rate $W_{ge}(t)$ (red) with $\overline{\tau}_g = 0.1$ s and constant relaxation rate $W_{eg}(t)$ (blue) with $\overline{\tau}_e = 0.01$ s. (**D**) Calculated distribution of τ_{ee} for the rates in A. (**E**) Calculated distribution of τ_{ee} for the rates in B. (**F**) Calculated distribution of τ_{ee} for the rates in C. Dotted lines indicates $\overline{\tau}_g$ and $\overline{\tau}_e$.

that in all three cases the behavior is broadband, this is because the rates are time-independent.

Figure 2.7 shows what happens when one of the rates is made time-dependent. In Panel A the excitation rate is weakly modulated about the relaxation rate, with an amplitude of 1 Hz. The corresponding histogram in Panel E still appears broadband and nominally hypoexponential. The modulation is increased to 2 Hz in Panel B, and the corresponding histogram in Panel F shows the onset of non-Poisson distributed behavior, with shoulders appearing at multiples of the modulation period. As the modulation amplitude is increased further, to 5 and 9 Hz in Panels F and G, respectively, the peaks at the multiples become more pronounced. In Panel G the peaks at multiples of the modulation period are clearly visible, but are roughly comparable in prominence to the broadband background. Lastly, in Panel H the peaks begin to overwhelm the background, indicating more strongly resonant behavior. This is a stochastic resonance.

There are three key features in the distribution of τ_{ee} which appear when the spin undergoes stochastic resonance:

1. Peaks at integer multiples of the drive period T_ω.

2. A broadband hypoexponential envelope.

3. A synchronization effect, expressed as the relative intensity between the peak at T_ω and the broadband background.

Figure 2.8A shows the simulated spin-state evolution and τ_{ee} histogram for a spin that perfectly tracks the modulation, i.e. is perfectly synchronized. The drive is $\omega = 10$ Hz, and $\overline{\tau}_e = \overline{\tau}_g = 0.1$ s. The sample rate for the simulation is 100 Hz, which yields a unit-area peak with height 100 in the event histogram.[2] To quantify this behavior, we define the synchronization efficiency, which is the area of the first peak divided by the area of the normalized event histogram. Because the area of the event histogram is normalized to 1, this sets an upper bound to the synchronization efficiency. For the maximally synchronized case, with no broadband background, the synchronization is 0.99.

To give some context for the simulated histograms, a Monte Carlo simulation was performed to generate exemplary time traces for differing degrees of synchronization. In this simulation, the drive is a voltage, which whenever it crosses a given threshold will sample a Poisson distribution to determine whether an excitation occurs. Relaxation events also sample a Poisson distribution, but are threshold independent. To sample the distribution, a random exponentially distributed number

[2] For a sample rate of 100 Hz, a single sample is 0.01 s. The peak is one sample wide, giving an area of 1 for a peak height of 100.

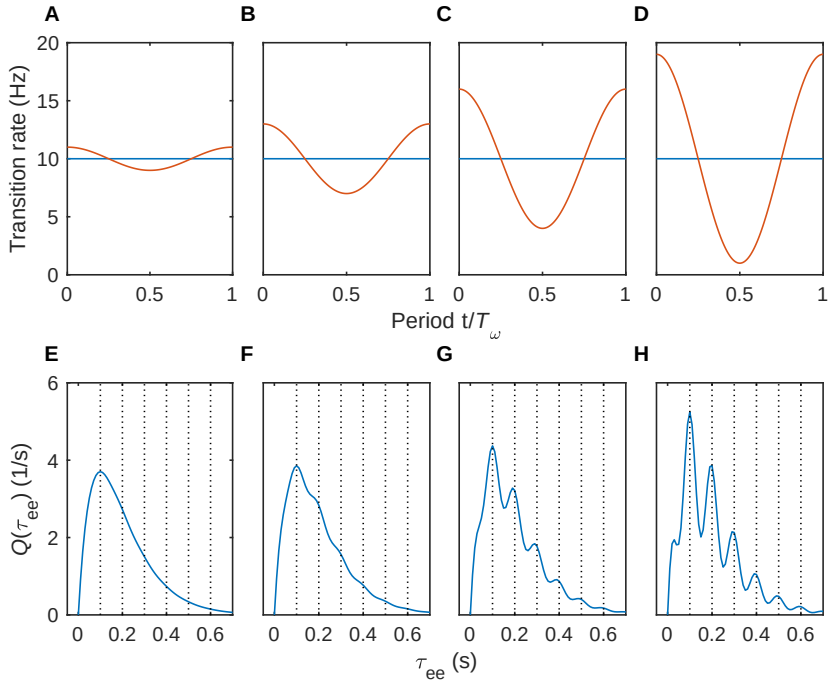

Figure 2.7. Relation between time-dependent transition rates and switching distribution. (**A**) Excitation rate $W_{ge}(t)$ modulated by 1 Hz (red) and constant relaxation $W_{eg}(t)$ (blue) rate with $\overline{\tau}_g = 0.1$ s. (**B**) Excitation rate $W_{ge}(t)$ modulated by 2 Hz (red) and constant relaxation $W_{eg}(t)$ (blue) rate with $\overline{\tau}_g = 0.1$ s. (**C**) Excitation rate $W_{ge}(t)$ modulated by 5 Hz (red) and constant relaxation $W_{eg}(t)$ (blue) rate with $\overline{\tau}_g = 0.1$ s. (**D**) Excitation rate $W_{ge}(t)$ modulated by 9 Hz (red) and constant relaxation $W_{eg}(t)$ (blue) rate with $\overline{\tau}_g = 0.1$ s. (**E**) Calculated distribution of τ_{ee} for the rates in A. (**F**) Calculated distribution of τ_{ee} for the rates in B. (**G**) Calculated distribution of τ_{ee} for the rates in C. (**H**) Calculated distribution of τ_{ee} for the rates in D. $\omega = 10$ Hz, $T_\omega = 0.1$ s for all simulations. Dotted lines are the first six multiples of the drive period.

is generated, and it is compared to the time constant for the respective process (excitation/relaxation). If it is larger than the time constant, the process occurs. This is equivalent to a constant relaxation rate and a time-dependent excitation rate. Sampling the event histogram directly does not account for the phase stability between the spin state evolution and the drive, necessitating this Monte Carlo method.

Figure 2.8B and C show the results of this simulation. To implement desynchronization between drive and spin state evolution, in Panel B the time constants governing excitation and relaxation were increased relative to that of the drive, to $\overline{\tau}_e = \overline{\tau}_g = 1$ s. In the time trace one can see that the spin state no longer perfectly tracks the drive, although excitation still preferentially occurs at the peaks of the drive. Moving to the histogram (generated from a 100 second simulation), one can see the characteristic peaked response of stochastic resonance. The first (dotted line) and second multiple of the drive frequency can be clearly identified, as well as a broadband background. The synchronization efficiency in this case is 0.36.

In Panel C the time constants have been increased further, to $\overline{\tau}_e = \overline{\tau}_g = 5$ s. Here the switching cycle duration does not track the drive well. The histogram reflects this, with a purely broadband response characteristic of random evolution. Likewise, the synchronization efficiency is very low, at 0.04. In future chapters the synchronization efficiency will be an important metric for characterizing the degree to which the spin state evolution tracks the drive.

2.6. STOCHASTIC RESONANCE IN STM EXPERIMENTS

To resolve the stochastic switching of individual spins and nanostructures using STM necessitated the development of a new measurement method, as the different structures investigated throughout this work each present unique challenges to measurement. The initial setup is analogous to that of a more conventional spin-polarized STM experiment, an external magnetic field lifts the degeneracy of the surface spins' magnetic states, a cryogenic environment reduces scattering to a degree that the spin lifetimes can be measured, and a cluster of magnetic atoms on the tip allows the magnetic states to be distinguished via tunnel magnetoresistance [9, 12]. The first extension to the setup comes in the form of a modulation source; an oscillating voltage is either applied directly to the tip, or to the z-scanner piezo. This modulation is what allows novel resonant behavior to be induced in the spins, but it also indirectly makes measuring the time-dependent spin-state significantly more difficult. For a voltage modulation the first order response is simply $I \propto V$, the current will mirror the applied voltage up to a linear scaling factor. When modulating the z-position, the first order response is $I \propto e^{\Delta z}$, due to the non-linearity of the tunnel junction. The signals of interest, namely fluctuations between the different spin states, are a perturbation on top of these linear responses, which can make resolving the time dependent spin-state difficult. Time-resolved dynamics are further obscured by both electrical and mechanical

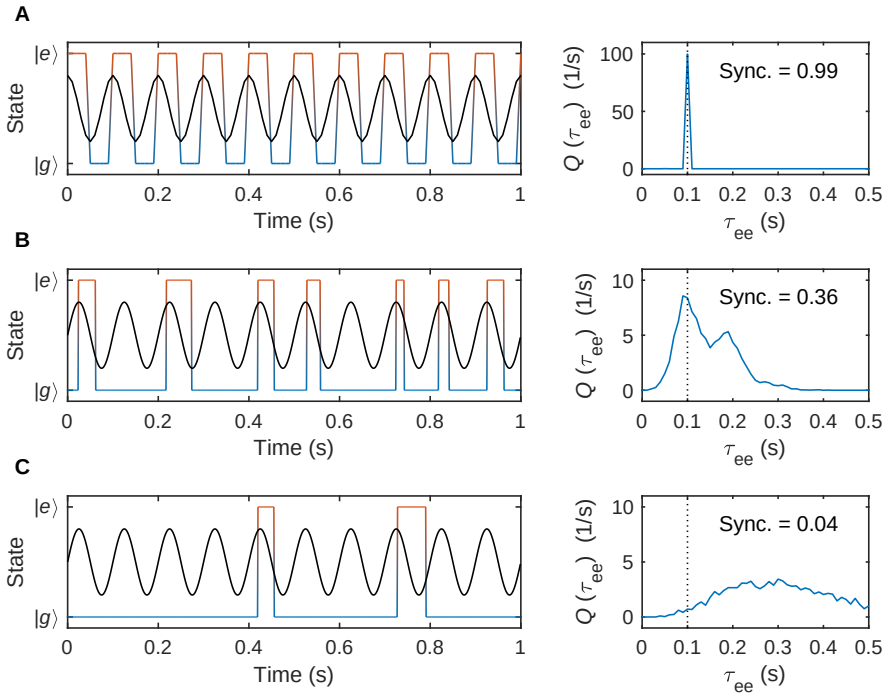

Figure 2.8. Simulations of spin state time traces (blue $|g\rangle$ to red $|e\rangle$) with corresponding switching distributions. Drive modulation $\omega = 10$ Hz (black), $T_\omega = 0.1$ (dotted lines). (**A**) Spin state deterministically tracks drive. (**B**) Monte Carlo simulation of the time-dependent spin state occupation with $\overline{\tau}_e = \overline{\tau}_g = 1$ s. (**C**) Monte Carlo simulation of the time-dependent spin state with $\overline{\tau}_g = \overline{\tau}_e = 5$ s.

noise. Attempts to address both of these difficulties led to the second significant extension in this technique: high frequency sampling of both the tunnel current and modulation source, combined with extensive post-processing of the resulting time-series data to extract the spin state. The processing encompasses both conventional signal processing techniques such as filtering and noise-whitening [39], and the application of physics-based models of the tunnel junction [6] and the dynamic conductivity of the spins [22].[3]

With this new measurement method capable of resolving switching dynamics and the theory of stochastic resonance extended to spins on surfaces, we now have a powerful tool-set for measuring the dynamics of open quantum systems. The following chapters investigate the dynamic behavior of three different structures on the Cu_2N surface, which all switch stochastically between their ground and first excited states. They have more in common than just their constituent components, in that they all, to a certain degree, exhibit "single-atom-like" behavior. The nine atom structure investigated in the context of classical stochastic resonance can be pictured as a single atom that has been "slowed down" by the fully compensated eight atom antiferromagnet beside it. Likewise the five atom structure, investigated in a semi-classical crossover regime, can be thought of as a single atom, since it is an antiferromagnet with one uncompensated atom. Lastly, a single atom is investigated directly, and driven to quantum stochastic resonance. By comparing the dynamic behavior of each of these structures, the transition between classical and quantum behavior in open quantum systems can be made clear.

REFERENCES

[1] G. Lindblad, *On the generators of quantum dynamical semigroups,* Communications in Mathematical Physics **48**, 119 (1976).

[2] H. D. Zeh, *On the interpretation of measurement in quantum theory,* Foundations of Physics **1**, 69 (1970).

[3] F. Delgado and J. Fernández-Rossier, *Spin decoherence of magnetic atoms on surfaces,* Progress in Surface Science **92**, 40 (2017).

[4] M. Ternes, *Spin excitations and correlations in scanning tunneling spectroscopy,* New Journal of Physics **17**, 63016 (2015).

[5] G. Binnig and H. Rohrer, *Scanning tunneling microscopy,* Helvetica Physica Acta **55** (1982).

[6] G. Binnig, H. Rohrer, C. Gerber, and E. Weibel, *Tunneling through a controllable vacuum gap,* Applied Physics Letters **40**, 178 (1982).

[3] The specific steps taken to process measurements on each structure are addressed in their respective chapters.

[7] D. M. Eigler and E. K. Schweizer, *Positioning single atoms with a scanning tunnelling microscope,* Nature **344**, 524 (1990).

[8] S. Yan, D.-J. Choi, J. A. J. Burgess, S. Rolf-Pissarczyk, and S. Loth, *Control of quantum magnets by atomic exchange bias,* Nature Nanotechnology **10**, 40 (2014).

[9] R. Wiesendanger, H.-J. Güntherodt, G. Güntherodt, R. J. Gambino, and R. Ruf, *Observation of vacuum tunneling of spin-polarized electrons with the scanning tunneling microscope,* Physical Review Letters **65**, 247 (1990).

[10] R. Wiesendanger, *Spin mapping at the nanoscale and atomic scale,* Reviews of Modern Physics **81**, 1495 (2009).

[11] S. Heinze, M. Bode, A. Kubetzka, O. Pietzsch, X. Nie, S. Blügel, and R. Wiesendanger, *Real-Space Imaging of Two-Dimensional Antiferromagnetism on the Atomic Scale,* Science **288**, 1805 (2000).

[12] A. J. Heinrich, J. A. Gupta, C. P. Lutz, and D. M. Eigler, *Single-Atom Spin-Flip Spectroscopy,* Science **306**, 466 (2004).

[13] T. Jamneala, V. Madhavan, and M. Crommie, *Kondo Response of a Single Antiferromagnetic Chromium Trimer,* Physical Review Letters **87**, 256804 (2001).

[14] A. A. Khajetoorians, B. Baxevanis, C. Hubner, T. Schlenk, S. Krause, T. O. Wehling, S. Lounis, A. Lichtenstein, D. Pfannkuche, J. Wiebe, and R. Wiesendanger, *Current-Driven Spin Dynamics of Artificially Constructed Quantum Magnets,* Science **339**, 55 (2013).

[15] S. Baumann, W. Paul, T. Choi, C. P. Lutz, A. Ardavan, and A. J. Heinrich, *Electron paramagnetic resonance of individual atoms on a surface,* Science **350** (2015).

[16] C. F. Hirjibehedin, C.-y. Lin, A. F. Otte, M. Ternes, C. P. Lutz, B. A. Jones, and A. J. Heinrich, *Large Magnetic Anisotropy of a Single Atomic Spin Embedded in a Surface Molecular Network,* Science **317**, 1199 (2007).

[17] A. F. Otte, M. Ternes, K. von Bergmann, S. Loth, H. Brune, C. P. Lutz, C. F. Hirjibehedin, and A. J. Heinrich, *The role of magnetic anisotropy in the Kondo effect,* Nature Physics **4**, 847 (2008).

[18] S. Rolf-Pissarczyk, S. Yan, L. Malavolti, J. A. J. Burgess, G. McMurtrie, and S. Loth, *Dynamical Negative Differential Resistance in Antiferromagnetically Coupled Few-Atom Spin Chains,* Physical Review Letters **119**, 217201 (2017).

[19] J. A. Burgess, L. Malavolti, V. Lanzilotto, M. Mannini, S. Yan, S. Ninova, F. Totti, S. Rolf-Pissarczyk, A. Cornia, R. Sessoli, and S. Loth, *Magnetic fingerprint of individual Fe4 molecular magnets under compression by a scanning tunnelling microscope,* Nature Communications **6**, 8216 (2015).

[20] B. Warner, F. El Hallak, H. Prüser, A. Ajibade, T. G. Gill, A. J. Fisher, M. Persson, and C. F. Hirjibehedin, *Controlling electronic access to the spin excitations of a single molecule in a tunnel junction,* Nanoscale **9**, 4053 (2017).

[21] L. Malavolti, G. McMurtrie, S. Rolf-Pissarczyk, S. Yan, J. A. Burgess, and S. Loth, *Minimally invasive spin sensing with scanning tunneling microscopy,* Nanoscale **12**, 11619 (2020).

[22] S. Loth, K. von Bergmann, M. Ternes, A. F. Otte, C. P. Lutz, and A. J. Heinrich, *Controlling the state of quantum spins with electric currents,* Nature Physics **6**, 340 (2010).

[23] S. Loth, M. Etzkorn, C. P. Lutz, D. M. Eigler, and A. J. Heinrich, *Measurement of Fast Electron Spin Relaxation Times with Atomic Resolution,* Science **329**, 1628 (2010).

[24] S. Loth, S. Baumann, C. P. Lutz, D. M. Eigler, and A. J. Heinrich, *Bistability in Atomic-Scale Antiferromagnets.* Science **335**, 196 (2012).

[25] S. Machlup, *Noise in Semiconductors: Spectrum of a Two-Parameter Random Signal,* Journal of Applied Physics **25**, 341 (1954).

[26] D. Gatteschi, R. Sessoli, and J. Villain, *Mesoscopic Physics and Nanotechnology* (Oxford University Press, Oxford, 2006).

[27] P. Dirac, *On the Theory of Quantum Mechanics,* Royal Society **112** (1926).

[28] E. Fermi, *Sulla quantizzazione del gas perfetto monoatomico,* Rendiconti Lincei **3** (1926).

[29] R. Benzi, G. Parisi, A. Sutera, and A. Vulpiani, *Stochastic resonance in climatic change,* Tellus **34**, 10 (1982).

[30] T. Wellens, V. Shatokhin, and A. Buchleitner, *Stochastic resonance,* Reports on Progress in Physics **67**, 45 (2004).

[31] R. R. Ernst, *Magnetic Resonance with Stochastic Excitation,* Journal of Magnetic Resonance (1969) **3**, 10 (1970).

[32] L. Gammaitoni, P. Hänggi, P. Jung, and F. Marchesoni, *Stochastic resonance,* Reviews of Modern Physics **70**, 223 (1998).

[33] G. Matteucci, *A study of the climatic regimes of the Pleistocene using a stochastic resonance model,* Climate Dynamics **6**, 67 (1991).

[34] I. Y. Lee, X. Liu, B. Kosko, and C. Zhou, *Nanosignal Processing: Stochastic Resonance in Carbon Nanotubes That Detect Subthreshold Signals,* Nano Letters **3**, 1683 (2003).

[35] T. Wagner, P. Talkner, J. C. Bayer, E. P. Rugeramigabo, P. Hänggi, and R. J. Haug, *Quantum stochastic resonance in an a.c.-driven single-electron quantum dot,* Nature Physics **15**, 330 (2019).

[36] A. Longtin, A. Bulsara, and F. Moss, *Time-interval sequences in bistable systems and the noise-induced transmission of information by sensory neurons,* Physical Review Letters **67**, 656 (1991).

[37] R. Löfstedt and S. N. Coppersmith, *Stochastic resonance: Nonperturbative calculation of power spectra and residence-time distributions,* Physical Review E **49** (1994).

[38] R. Löfstedt and S. N. Coppersmith, *Quantum stochastic resonance,* Physical Review Letters **72**, 1947 (1994).

[39] S. M. Kuo and D. R. Morgan, *Active noise control: a tutorial review,* Proceedings of the IEEE **87**, 943 (1999).

3

Classical Stochastic Resonance

3.1. The 2×4+1 Antiferromagnet

The experimental portion of this thesis begins with what at first glance may seem to be a rather complex structure comprised of nine Fe atoms subject to a static external magnetic field. But by virtue of its size it behaves more like a classical magnet, and is a natural starting point to explore the appearance of classical stochastic resonance in few-atom nanostructures.

Conceptually, it is helpful to think of this structure as an eight-atom antiferromagnet, with one additional atom weakly coupled to it. The additional atom lifts the degeneracy of the two lowest lying states, and by this also provides a means of controlling which of the two is lowest in energy. In the eight atom analogue, four of the atoms align their magnetization with the external magnetic field, and four align in the opposite direction. The two configurations which exhibit this pattern of alignment form the degenerate Néel-like states [1] (Figure 3.1 shows the characteristic checkerboard in apparent height observed when measured with a spin-polarized tip). The additional atom in the nine-atom structure (Figure 3.2), or $2 \times 4 + 1$, breaks this balance. In the ground state there are now five atoms aligned with the field, of which there is only one possible configuration. The resulting energy shift is not so drastic that the structure remains in its ground-state indefinitely. At a temperature of $T = 2.5$ K it still switches readily between its ground and first excited state (henceforth simply termed the excited state). The switching is caused by thermal bath electrons which are able to provide enough energy to induce an excitation. The switching can be measured by applying a small bias

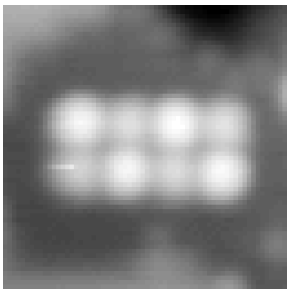

Figure 3.1. Constant-current spin-polarized topography of a 2×4 nanostructure. The scan frame is a 4.5 nm square, V_{set} = 1 mV, I_{set} = 30 pA B_x = 1 T, T = 2.5 K.

voltage of V_{dc} = 1 mV, and monitoring the resulting current. Due to the different conductivity of the ground and excited state during spin-polarized tunneling, the state-dependent current will be higher and lower, respectively.

3.2. CONTROLLING EXCHANGE FIELD WITH A SPIN-POLARIZED TIP

Recent work in spin-polarized STM has demonstrated that the STM tip can act as an effective exchange field to magnetic atoms on the surface [2, 3]. We use this exchange field to apply a local magnetic field to one of the five atoms aligned with the magnetic field in the $2 \times 4 + 1$'s ground state, which can controllably shift the ground state configuration until it is degenerate with, and even higher in energy than the first excited state (shown schematically in Figure 3.3). [1]

Because the exchange field results from direct exchange interaction between the magnetic moment of the tip and the atom on the surface its strength is strongly tip-sample distance dependent. Modulating the tip-sample distance z effectively allows the ground and excited state energy to be specified at any given point in time. Furthermore, changing the energy landscape of the $2 \times 4 + 1$'s spin state's provides a means of controlling the switching dynamics, and thereby of inducing stochastic resonance. The stochastic resonance condition is met when the spin state transitions are synchronized with an external drive, such as that provided by a time-varying tip-exchange field. What does this condition look like? When the spin is

[1] Section 3.5 contains a detailed discussion of the state configuration.

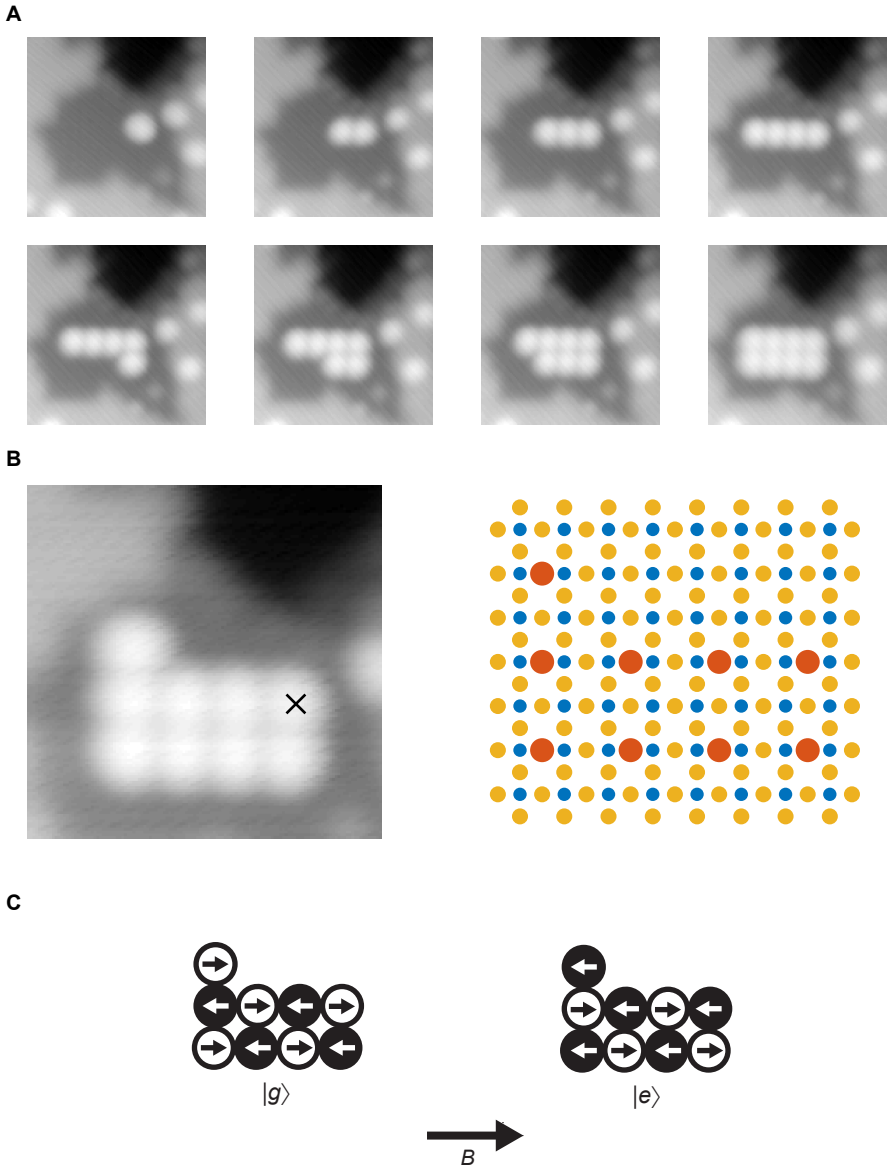

Figure 3.2. (**A**) Constant-current topographies detailing the atom-by-atom construction of a nine-Fe-atom nanostructure. V_{set} = 100 mV, I_{set} = 100 pA. (**B**) All subsequent measurements are acquired on the atom marked with a cross. The ball and stick model of the surface and structure indicates N atoms (blue), Cu atoms (orange) and Fe atoms (red). (**C**) Schematic representation of the ground state $|g\rangle$ and excited state $|e\rangle$, with the color indicating orientation of the magnetic moment, and the black arrow showing the magnetic field direction. $B_x = 1$ T, $T = 2.5$ K.

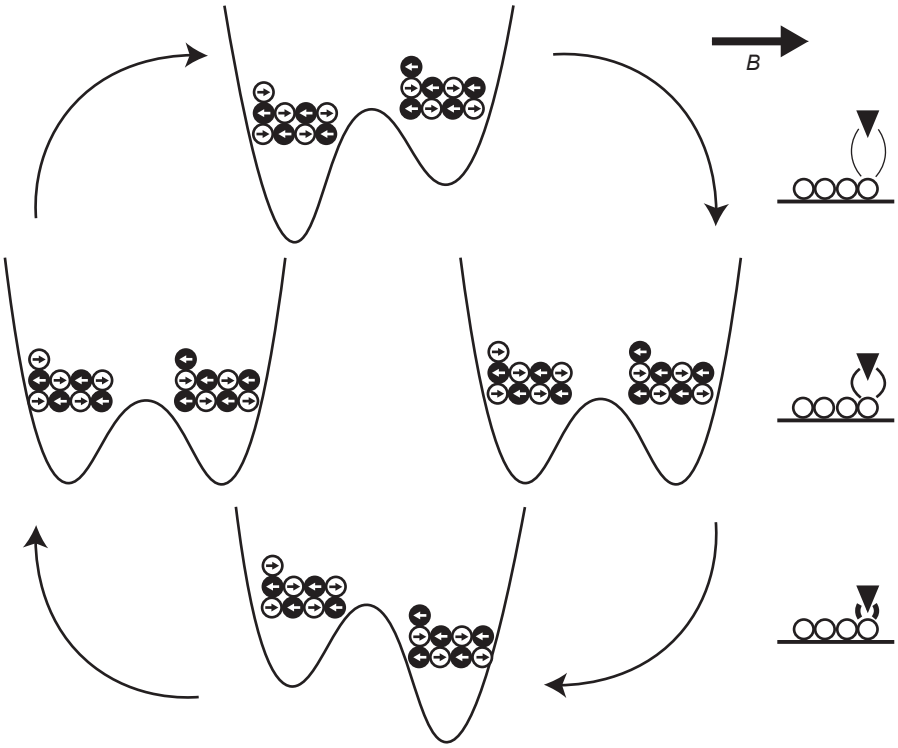

Figure 3.3. Schematic of the energy landscape due to the exchange bias modulation process. The four curves correspond to one full cycle of tip-sample distance modulation. The y-axis represents energy and the x-axis represents the spin states, with the first two states (ground and excited) explicitly drawn. The bold arrow shows the external magnetic field direction. The schematics on the right show the tip position throughout the z-modulation cycle that modulates the exchange bias field.

in its ground state, the tip exchange field lowers the energy of a transition to the excited state, and thereby makes it more likely to happen. Similarly, when the spin is in its ground state, the tip exchange field lowers the energy of a transition back to the ground state. This leads to the spin-state evolution favouring transitions which are in lockstep with the drive, and therefore to the synchronization effect.

In our experiment, we first create a spin-polarized tip by "picking-up"[4] a small cluster of Fe atoms from the surface. The magnetic atoms on the tip create an exchange field, which allows us to change the applied exchange-field by modulating the z-position of the STM tip relative to the structure sinusoidally (Figure 3.4). The $z = 0$ position is defined by the junction conductivity, $V_{set} = 20$ mV, $I_{set} = 3$ nA for this measurement. Here, the rate of modulation $\omega = 0.5$ Hz is significantly slower than the intrinsic switching rates which range from 10 to 100 Hz. During the cycle of modulation shown in Figure 3.4A the tip modulation amplitude is $dz = 50$, meaning the z-position of the piezo is extended by -50 pm, bringing the tip closer to the nanostructure, and then retracted by $+50$ pm bringing it further away. [2]

Figure 3.4B shows the resulting current measured on the structure, with clear switching between ground and excited state. There are, in effect, two sources of time-dependent conductivity. This can make the extraction of the time-dependent spin state difficult. The modulation in z not only modulates the exchange bias field but also changes the junction conductance, which likewise results in an oscillation of the current that is superimposed on the rapid changes in current that originate from spin switching.

However, the exponential distance dependence of tunnel junctions can be readily modelled. By introducing a two-conductivity model (one for each state), the respective time-dependent conductivity (red and blue curves) can be calculated. Each state will trace its respective curve in the time-dependent tunnel current; the high conductivity state will trace the blue curve, while the low conductivity state will trace the red curve. This allows the states to be distinguished at any point in time. The structure can be seen to switch between the excited and ground state, and will trace that state's respective z-dependent conductivity curve. A Schmitt trigger threshold is applied, with a dynamically varying excitation and relaxation threshold set by the respective conductivity curves. The hysteresis present in the dynamic Schmitt trigger significantly reduces false events, while using the measured z-position to calculate the threshold at each point in time ensures phase stability between the threshold and the current.

[2] Note that the measurement itself was not acquired for only the two seconds shown in the trace in Figure 3.4, but rather for six and a half minutes. This amount of time balances measuring enough counts to make conclusions about the statistics of the switching dynamics, with the necessity to measure a full modulation frequency dependence within a 12 hour measurement window. How long one needs to measure is of course a function of the typical lifetimes of the structure, as the $2 \times 4 + 1$ evolves quite slowly more measurement time is needed compared to some of the faster evolving structures measured in later chapters.

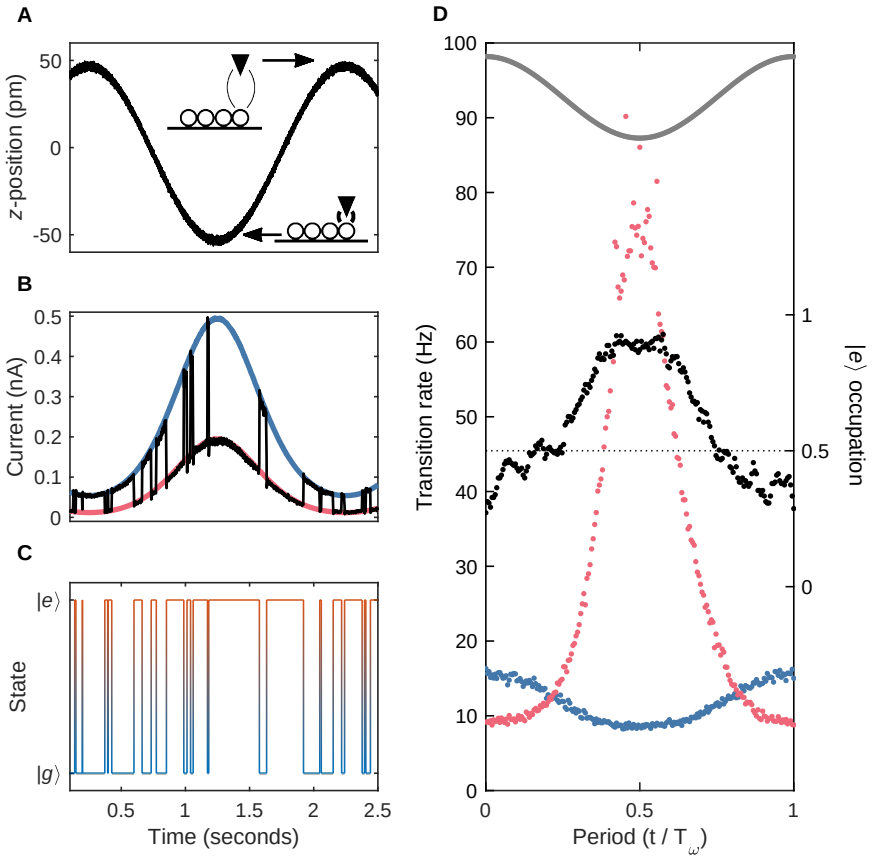

Figure 3.4. Applying an exchange bias field via a low frequency z-modulation: (**A**) Modulation of the z-position in the STM, with schematics showing the tip-sample distance (the tip is far away for positive z and closer for negative z). (**B**) Current measured during the z-modulation (black), excited state conductivity is shown in red, ground state conductivity in blue. (**C**) Occupation of the ground $|g\rangle$ and excited $|e\rangle$ state during the z-position modulation. (**D**) Time dependent conditional transition rates for transitions from the higher conductivity (ground) state to the lower conductivity (excited) state are shown in red. Transition rate from the lower conductivity (excited) to the higher conductivity (ground) state are shown in blue. The time-dependent average occupation of the excited state is shown in black, with a schematic of the tip position shown in grey. $\omega = 0.5$ Hz, $dz = 50$ pm, $V_{dc} = 1$ mV, $V_{set} = 20$ mV, $I_{set} = 3$ nA, $B_x = 1$ T, $T = 2.5$ K.

The extracted state as a function of time with z-modulation applied is plotted in Figure 3.4C. It exhibits a preference for the higher conductivity state when the tip is farther from the structure, and a preference for the lower conductivity state when the tip is closer. From this behavior one can determine that the higher conductivity state is lower in energy when the tip is further away (no exchange field applied), and the lower conductivity state is lower in energy when the tip is close (large exchange field applied). The notion of excited state and ground state can be unclear, as the energy landscape of the spin structure is constantly changing due to the tip's exchange field; for clarity we define the ground state as the state which is primarily occupied when the tip is furthest away from the structure. For this structure the high conductivity state is the ground state $|g\rangle$, and the low conductivity state is the excited state $|e\rangle$.

To more precisely understand how the modulation affects the spin dynamics, the transitions between the two states can be mapped back to a single period of modulation, yielding the time-dependent transition rates as a function of where in the period of the modulation they occur. This quantity can in turn be divided by the occupation at the respective point in time, to yield the conditional transition rates (Figure 3.4). As described in Section 2.3, the conditional rates are the probability to make a transition from one state to another, given that the respective state is occupied. The full details of how the conditional transition rates are extracted from the measurements is discussed in Chapter 2.

The measured transition rates do not depend on the modulation frequency, which we attribute to the Markovian nature of the dynamics. As such, significant improvements in signal-to-noise can be gained by averaging over all measured modulation frequencies, which yields the rate diagram in Figure 3.4D. The occupation, however, does depend on the modulation frequency, which will be further explored later. Looking at the rates, the behavior seen in the time trace becomes more clear. When the tip is far away from the structure, transitions to the ground state (blue) occur at a faster rate than transitions to the excited state (red). As such, the ground state is occupied more frequently. Conversely, when the tip is closer to the structure, transitions to the excited state are much faster (almost an order of magnitude) than transitions to the ground state. This results in a preferential occupation of the excited state when the tip is close, and therefore when the exchange field is maximal.

What is the noise source driving these transitions? There are two primary features in the rates diagram which allow this to be determined. First, the transition rates smoothly track the exchange field, with excitation and relaxation 180° out of phase with one another. Second, as the rates approach parity, the excited state occupation approaches 0.5, and indeed approaches 1 as transitions into the excited state overwhelm relaxation back into the ground state. This behavior fits to the picture of classical thermally activated transitions with a barrier height that is modulated over time.

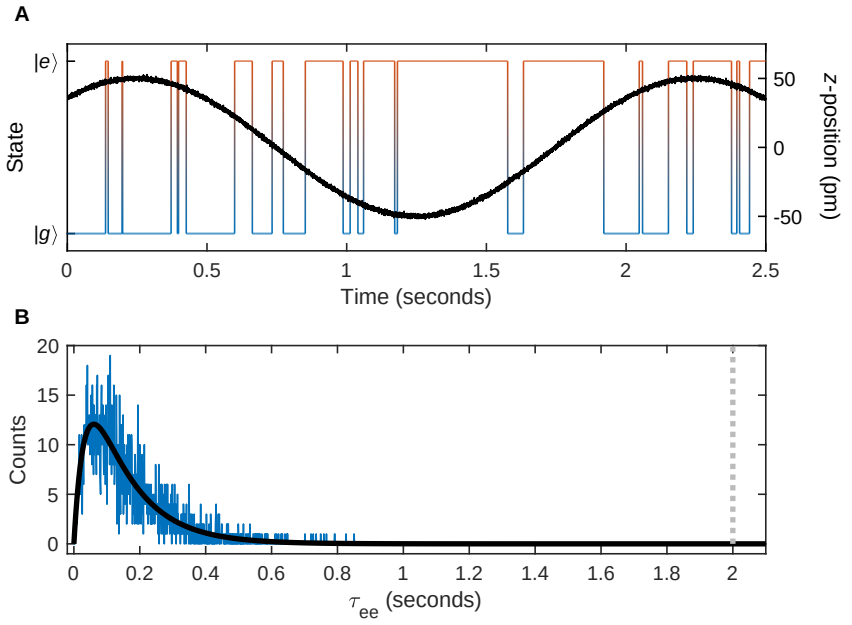

Figure 3.5. (**A**) Exemplary time trace of the z-position (black) and spin state ($|g\rangle$ blue to $|e\rangle$ red) measured with a low frequency (modulation period $T_\omega = 2$ s, grey) harmonic drive applied. (**B**) Histogram of the time between excitation events τ_{ee} (blue) least-squares fit with a hypoexponential curve (Equation 2.2, black, $\overline{\tau}_e = 33 \pm 1$ ms, $\overline{\tau}_g = 125 \pm 3$ ms, $c = 2.45 \pm 0.03$ counts·s). $\omega = 0.5$ Hz, $dz = 50$ pm, $V_{dc} = 1$ mV, $V_{set} = 20$ mV, $I_{set} = 3$ nA, $B_x = 1$ T, $T = 2.5$ K.

3.3. STOCHASTIC RESONANCE IN FREQUENCY

To learn about the full statistics of a given time trace, histograms are generated which plot the cycle duration time τ_{ee}, recalling from Chapter 2 the definition of $\tau_{ee} = \tau_g + \tau_e$. Figure 3.5 shows a histogram of τ_{ee} with a low frequency modulation of $\omega = 0.5$ Hz applied. The histogram follows a hypoexponential distribution, indicating that both excitation and relaxation are sampling Poisson distributions. At low frequencies the modulation is much slower than the time scale at which the spin switching occurs, and therefore does not affect the switching distribution.

In Figure 3.6, a higher frequency drive of $\omega = 9$ Hz is applied. The modulation of the state energies is now occurring at a time-scale comparable to that of the noise-induced transitions, resulting in resonant behavior. The observed switching is neither fully deterministic behavior, nor fully random. The state energies are modulated such that the noise induced switching will occur preferentially in sync

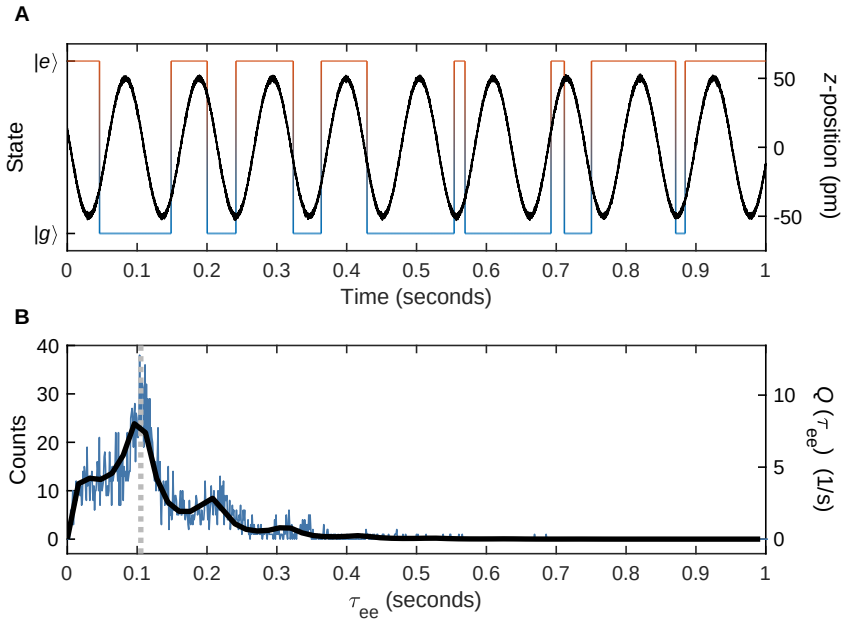

Figure 3.6. (**A**) Exemplary time trace of the z-position (black) and spin state ($|g\rangle$ blue to $|e\rangle$ red) measured with a faster harmonic drive. (**B**) Histogram of the time between excitation events (blue), analytically modelled $Q(\tau_{ee})$ using conditional transition rates (Equation 2.12, black), drive period $T_\omega = 0.11$ s (grey). $\omega = 9$ Hz, $dz = 50$ pm, $V_{dc} = 1$ mV, $V_{set} = 20$ mV, $I_{set} = 3$ nA, $B_x = 1$ T, $T = 2.5$ K.

with the drive. To model this process the time-dependent conditional transition rates are used to calculate $Q(\tau_{ee})$, an analytic function which describes the distribution of times between excitation events [3]. $Q(\tau_{ee})$ is normalized such that the integral over the distribution of switching times is 1. This can be thought of as ensuring that for long times, the system will switch with unit probability. By contrast, the integral of the measured switching time distribution is the number of switching cycles throughout the duration of the measurement, and therefore depends explicitly on the measurement duration. To quantitatively compare calculated and measured histograms, this scaling needs to be accounted for. Throughout this thesis the raw measured counts are shown on the left axis, and the normalized switching time distribution is shown on the right. Performing this scaling allows the data and the model to be superimposed on one another, and the agreement is excellent (Figure 3.6). The peak at the modulation period is reproduced, as well as the next two integer multiples. The modelled distribution shows the interplay between the stochastic switching causing the broadband hypoexponential envelope and the synchronized switching which results in peaks at the multiples of the modulation period. The peak at the 9 Hz modulation period is prominent, indicating a significant synchronization between modulation and spin state.

The measurement was repeated for a series of frequencies (Figure 3.7A), to track the appearance of the stochastic resonance. The low frequency behavior is a broadband hypoexponential distribution, as discussed previously. As the drive frequency is increased, peaks begin to appear at the drive period, as well as at integer multiples of it. The spin switching is not fully random anymore in this frequency range. For even higher frequencies, the peak density increases, until a broadband response, similar to that observed at low frequencies, is again obtained. This broadband response is characteristic of a loss of synchronization between the drive and the switching; the drive is simply too fast for the noise-induced switching to track it.

$Q(\tau_{ee})$ was calculated for the five curves in Figure 3.7A, and reproduces the results well. This confirms that the system is indeed undergoing stochastic resonance, with both the onset and disappearance of the resonance having been effectively modelled. Furthermore, Markovian spin state evolution is a fundamental assumption of the transition rate model, which by virtue of the strong agreement between the measurement and the analytic calculation allows non-Markovian dynamics to be excluded. In the context of the classical noise presented by the thermal bath, this means that the bath always reaches equilibrium between subsequent scattering event with the spin, making it effectively "memoryless".

The degree to which the spin state switching synchronizes with the drive can be quantified by comparing the time between switching events τ_{ee} to the drive period T_{ω}. The relative number of events that occur in sync, versus those that occur at other times, yields the synchronization or sync. efficiency. Figure 3.7B shows the synchronization efficiency as a function of drive frequency. The synchronization

[3] for a full derivation see Chapter 2

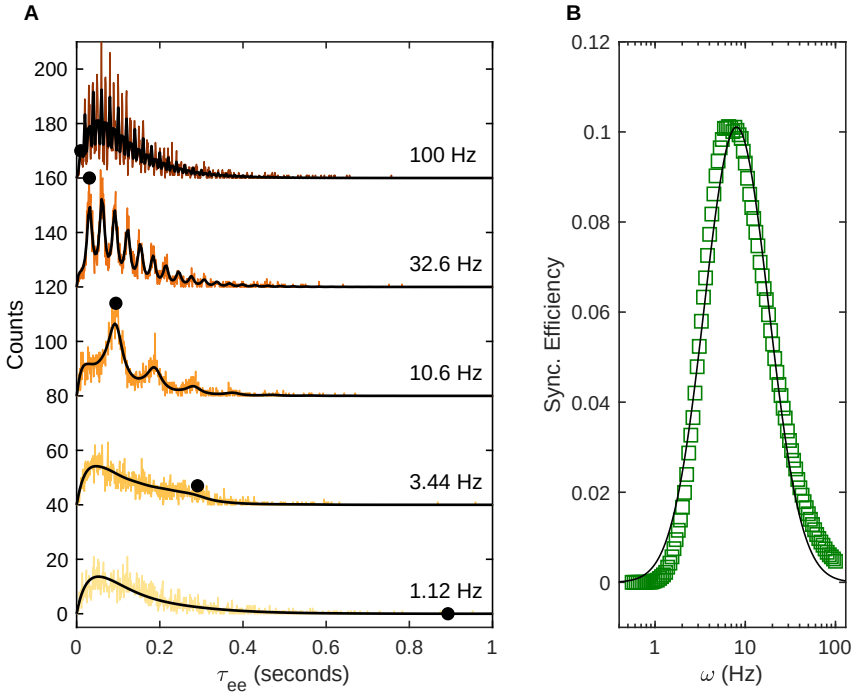

Figure 3.7. (**A**) Histograms of the time between excitation events for five frequencies (black dots indicate period), analytic model $Q(\tau_{ee})$ using conditional transition rates (Equation 2.12, black, scaled to account for measurement duration), offset for clarity. (**B**) Frequency-dependent synchronization efficiency (green) and least-squares fit to a log-normal function (Equation 3.1, black, $\omega_0 = 8 \pm 1$ Hz, $\sigma = 0.356 \pm 0.005$ $\log_{10}$·Hz, $c = 0.101 \pm 0.001$). $dz = 50$ pm, $V_{dc} = 1$ mV, $V_{set} = 20$ mV, $I_{set} = 3$ nA, $B_x = 1$ T, $T = 2.5$ K.

efficiency increases with frequency, until a maximum at 8 Hz is reached, and then decreases again. For low frequencies the drive is much slower than the noise induced transition rates, and therefore does not result in synchronization. Likewise, at high frequencies, the drive is much faster, and therefore also does not synchronize. The maximum that is observed occurs when the stochastic resonance condition is maximally satisfied. The frequency dependent form of the synchronization efficiency can be approximated with a log-normal function of the form:

$$\chi(\omega) = c \cdot e^{-\frac{1}{2}(\frac{\log_{10}(\omega)-d}{\sigma})^2}, \tag{3.1}$$

where d gives the center frequency (the stochastic resonance frequency ω_0 is defined as $\omega_0 = 10^d$ for ease of interpretability), σ gives the width, and c quantifies the strength of the synchronization effect. Fits to the measured synchronization efficiency using $\chi(\omega)$ allow ω_0 to be readily determined, here $\omega_0 = 8 \pm 1$ Hz. At this frequency the collaborative effect between the noise and the drive is strongest, resulting in a synchronized response.

It is worth noting that stochastic resonance is a particularly broadband effect, the stochastic resonance condition can be partially satisfied at frequencies well below and above the resonance frequency. Indeed, undergoing stochastic resonance also influences the average occupation of the respective spin states over a broad frequency window. Figure 3.8A shows the average occupation during one period of low frequency modulation at $\omega = 0.5$ Hz on the left, and the average occupation during a resonant modulation at $\omega = 9$ Hz on the right. The occupation changes its magnitude, shifting preferentially towards occupying the excited state. It also changes its phase relative to that of the drive. Panel B shows the full frequency dependence. The occupation is well reproduced by a Lorentzian line-shape (black) of the form:

$$\Upsilon(\omega) = L \cdot \frac{\frac{1}{\Gamma}}{1 + (\frac{\omega}{\Gamma})^2} + L_0, \tag{3.2}$$

where Γ is the width of the Lorentzian, L is the amplitude, and L_0 is the offset. The phase undergoes a characteristic shift as the modulation frequency is swept across the resonance frequency, and then changes more gradually for higher frequencies.

3.4. STOCHASTIC RESONANCE IN TEMPERATURE

As well as modifying the drive frequency such that it matches the transition rates defined by the noise, one can also analogously modify the noise itself to match the drive. Indeed, it is exactly this class of measurements which led to the original characteristic feature of stochastic resonance [5], an increase in signal-to-noise as a function of noise power. By increasing the noise power, and thereby the noise-induced transition attempt rate, the stochastic resonance condition will result in more signal at the drive frequency as the rate approaches the period of the drive (Figure 3.9).

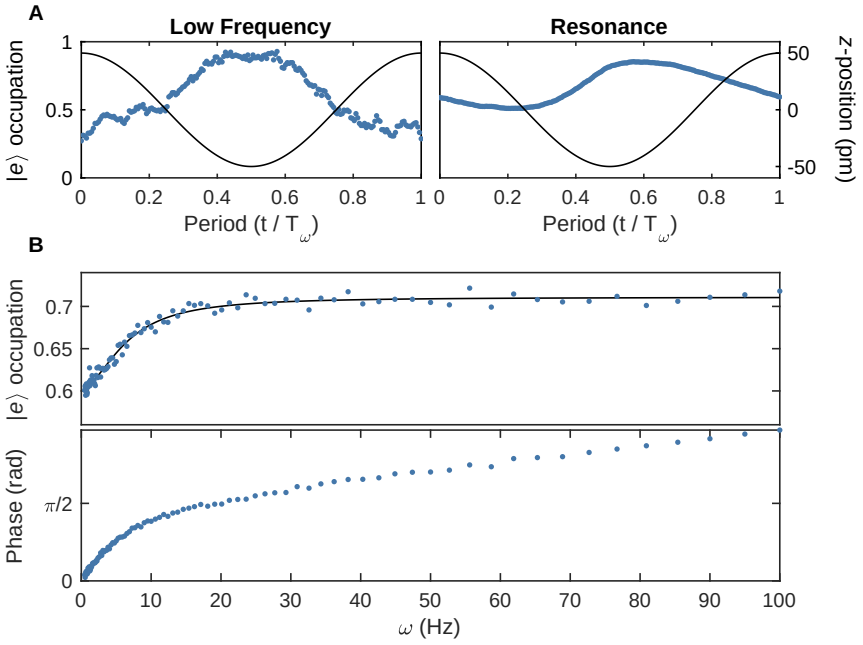

Figure 3.8. (**A**) Occupation modulation during one period of drive at $\omega = 0.5$ Hz (low frequency) and resonance ($\omega = 9.01$ Hz). (**B**) Excited state occupation as a function of modulation frequency (top, black line is a least-squares fit using Equation 3.2 with $\Gamma = 6.8 \pm 0.4$ Hz, $L = -4.7 \pm 0.4$ Hz, $L_0 = 0.711 \pm 0.001$), relative phase shift between the excited state occupation and the drive as a function of frequency (bottom). $dz = 50$ pm, $V_{dc} = 1$ mV, $V_{set} = 20$ mV, $I_{set} = 3$ nA, $B_x = 1$ T, $T = 2.5$ K.

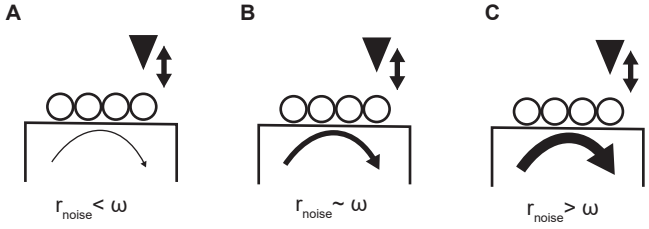

Figure 3.9. Schematic description of different stochastic resonance regime where (**A**) the noise rate is slower than modulation frequency, (**B**) the noise rate is comparable to modulation frequency, and (**C**) the noise rate is faster than modulation frequency.

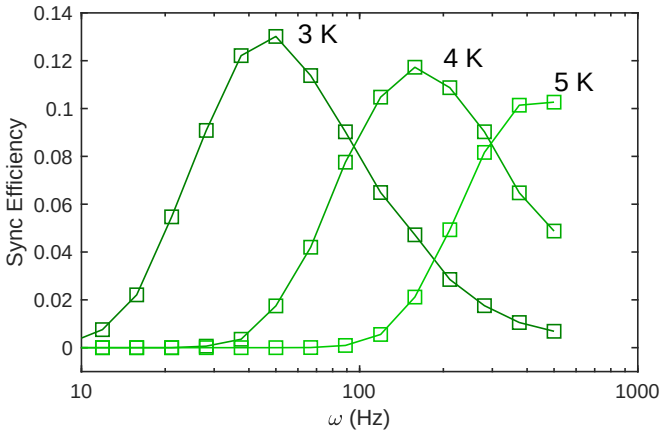

Figure 3.10. Frequency dependent synchronization efficiency, measured at three temperatures. $dz = 50$ pm, $V_{dc} = 1$ mV, $V_{set} = 20$ mV, $I_{set} = 3$ nA, $B_x = 1$ T.

Here, we use synchronization efficiency as a measure of "signal", as it quantifies how strongly the drive and the switching are synchronized. Frequency sweeps were performed at three different temperatures, in order to characterize how the stochastic resonance maximum shifts (Figure 3.10). As the temperature increases, so, too, does the stochastic resonance condition. The increased temperature effectively increase the overall noise-induced transition rate, and the drive will have to be proportionally faster in order to match its timescale.

The thermal bath is a classical noise source, as the transitions it promotes scale to zero as temperature approaches 0 K. By keeping the drive frequency fixed and sweeping the temperature (Figure 3.11), this noise source can be precisely controlled. As the noise dependent transition rate approaches the time-scale of the drive, a maximum in synchronization efficiency is observed. For a harmonic drive at $\omega = 88.9$ Hz the synchronization efficiency is maximal at around $T = 3.4$ K. For a $\omega = 281$ Hz drive, the maximum is approximately 1 K higher at $T = 4.5$ K. In general, higher drive frequencies result in a shift of the maximum to higher temperatures. This strong temperature dependence of the resonance frequency indicates that the dominant noise source is thermal noise.

The $2 \times 4 + 1$ clearly demonstrates the equivalency between changing the noise rate and the drive frequency. Just as keeping the temperature fixed and sweeping the frequency results in a maximum in synchronization efficiency, so too does keeping the drive frequency fixed and sweeping the temperature. This powerful equivalence is at the heart of stochastic resonance phenomena. The onset of in-

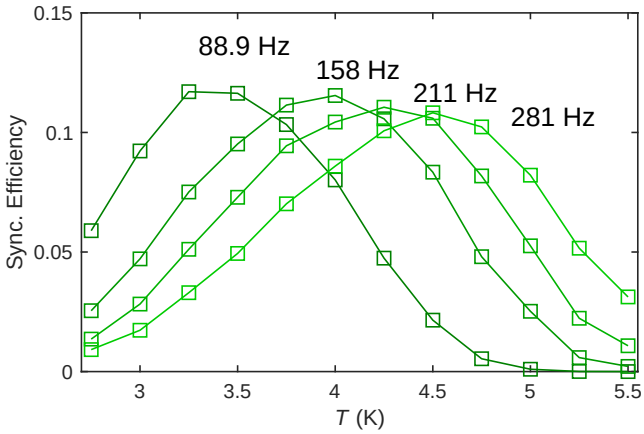

Figure 3.11. Temperature dependent synchronization efficiency, shown for four different drive frequencies. $dz = 50$ pm, $V_{dc} = 1$ mV, $V_{set} = 20$ mV, $I_{set} = 3$ nA, $B_x = 1$ T.

creasing synchronization with increasing rate was the characteristic that most intrigued the scientific community about stochastic resonance, as it had the non-intuitive characteristic of increasing signal (synchronization) when increasing noise (in this case temperature).

Let's investigate the temperature dependence of the noise more explicitly. Generally, a thermally activated process over an energy barrier can be characterized by a temperature dependent rate as:

$$r(T) = r_0 e^{\frac{\varepsilon}{k_B T}}, \tag{3.3}$$

where r_0 scales the strength of the rate, k_B is the Boltzmann constant, and ε is the barrier height. This is known as the Arrhenius equation [6]. Taking the natural logarithm yields the linear form:

$$\log r(T) = \log(r_0) - \frac{\varepsilon}{k_B}\frac{1}{T}. \tag{3.4}$$

Because stochastic resonance is a cooperative effect between the noise and the drive, the stochastic resonance frequency ω_0 mirrors the dominant noise rate. By plotting the natural logarithm of ω_0 versus inverse temperature $\frac{1}{T}$, the noise's temperature dependence can be determined. Figure 3.12 shows a clear linear dependence, with excellent agreement when fit with the Arrhenius equation. This indicates that the dominant noise-source for the $2 \times 4 + 1$ is indeed classical, namely thermal activation over a barrier with effective height $\varepsilon = 1.35 \pm 0.05$ meV. This

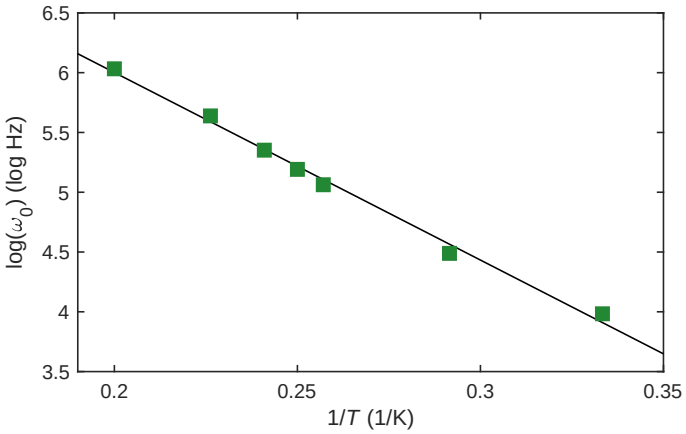

Figure 3.12. Arrhenius plot of the natural log of the stochastic resonance frequency ω_0 versus inverse temperature (green) with least-squares fit to the Arrhenius equation (Equation 3.4, $\varepsilon = 1.35 \pm 0.05$ meV, $r_0 = 9.3 \pm 0.1$ kHz). $dz = 50$ pm, $V_{dc} = 1$ mV, $V_{set} = 20$ mV, $I_{set} = 3$ nA, $B_x = 1$ T.

means that although this is quite a small structure, with clear discrete quantum spin states, its coupling to its environment yields distinctly classical behavior. From the point of view of the stochastic resonance process, this is a classical spin.

3.5. MODELLING THE SCATTERING PROCESS

To model the measured transition rates, the state structure was first calculated using a spin Hamiltonian formalism [7–9] demonstrated previously for molecular and atomic spin systems:

$$\hat{H} = \sum_{a=0}^{N-1} -g\mu_B \boldsymbol{B} \cdot \hat{\boldsymbol{S}}_{\boldsymbol{a}} + D_a(\hat{S}_{x,a})^2 + E_a(\hat{S}_{y,a}^2 - \hat{S}_{z,a}^2) + \hat{H}_J, \tag{3.5}$$

where g is the Landé g-factor, μ_B the Bohr magneton, and $\hat{S}_{i,a}$ is the spin operator in the i direction acting on the a^{th} atom (as conventionally defined [10]). N is the number of atoms in the structure, here $N = 9$. $\boldsymbol{B}$ is the magnetic field vector (B_x, B_y, B_z) and $\hat{\boldsymbol{S}}_{\boldsymbol{a}}$ is the spin operator vector $(\hat{S}_{x,a}, \hat{S}_{y,a}, \hat{S}_{z,a})$ for the a^{th} atom. The symmetry of the crystal field yields magnetocrystalline anisotropy which is modelled using uniaxial anisotropy D_a and transverse anisotropy E_a.

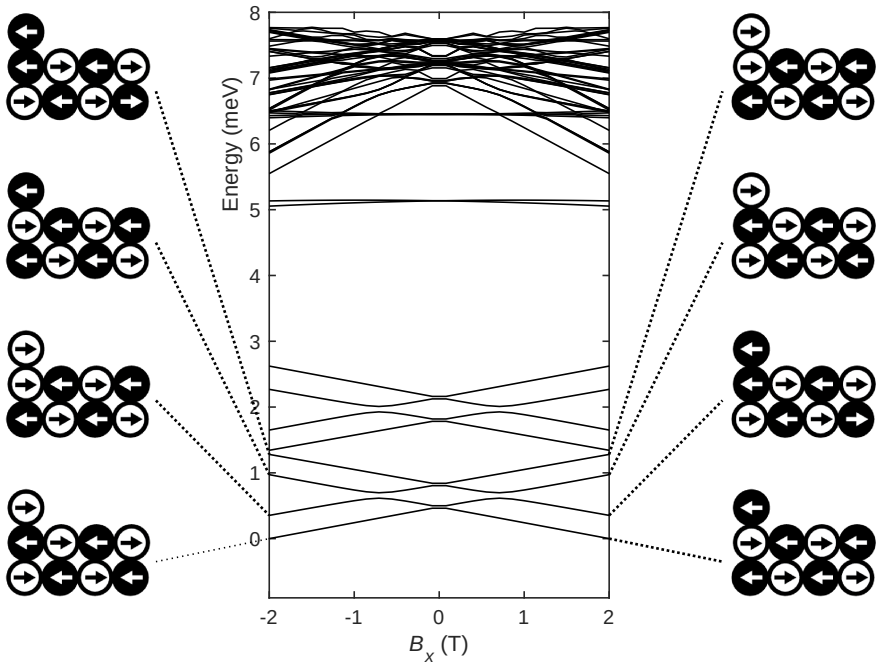

Figure 3.13. State diagram of the $2 \times 4 + 1$ structure, with schematics showing the spin structure of the four lowest lying states.

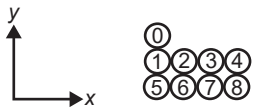

Parameter	0	1	2	3	4	5	6	7	8
S	2	2	2	2	2	2	2	2	2
g	2.05	2.05	2.05	2.05	2.05	2.05	2.05	2.05	2.05
D (meV)	-1.7	-2.0	-2.0	-2.0	-1.82	-1.82	2.0	2.0	1.82
E (meV)	0.4	0.4	0.4	0.4	0.4	0.4	0.4	0.4	0.4
J_x (meV)	-	0.76	0.76	0.76	-	0.76	0.76	0.76	-
J_y (meV)	0.042	0.042	0.042	0.042	0.042	-	-	-	-

Table 3.1. Spin Hamiltonian parameters for the $2 \times 4 + 1$ nanostructure. J_x and J_y are the Heisenberg coupling energies between the atom specified in the column header and the next atom in the $+x$ and $-y$ direction, respectively. Schematic shows the numbering system for the atoms.

$\hat{H}_J$ accounts for the Heisenberg exchange interaction between the constituent atoms of the nanostructure, which for the $2 \times 4 + 1$ is:

$$\begin{aligned}\hat{H}_j = &J_{x,1}\hat{\mathbf{S}}_\mathbf{1}\cdot\hat{\mathbf{S}}_\mathbf{2} + J_{x,2}\hat{\mathbf{S}}_\mathbf{2}\cdot\hat{\mathbf{S}}_\mathbf{3} + J_{x,3}\hat{\mathbf{S}}_\mathbf{3}\cdot\hat{\mathbf{S}}_\mathbf{4} + J_{x,5}\hat{\mathbf{S}}_\mathbf{5}\cdot\hat{\mathbf{S}}_\mathbf{6} + J_{x,6}\hat{\mathbf{S}}_\mathbf{6}\cdot\hat{\mathbf{S}}_\mathbf{7} + J_{x,7}\hat{\mathbf{S}}_\mathbf{7}\cdot\hat{\mathbf{S}}_\mathbf{8} + \\ &J_{y,0}\hat{\mathbf{S}}_\mathbf{0}\cdot\hat{\mathbf{S}}_\mathbf{1} + J_{y,1}\hat{\mathbf{S}}_\mathbf{1}\cdot\hat{\mathbf{S}}_\mathbf{5} + J_{y,2}\hat{\mathbf{S}}_\mathbf{2}\cdot\hat{\mathbf{S}}_\mathbf{6} + J_{y,3}\hat{\mathbf{S}}_\mathbf{3}\cdot\hat{\mathbf{S}}_\mathbf{7} + J_{y,4}\hat{\mathbf{S}}_\mathbf{4}\cdot\hat{\mathbf{S}}_\mathbf{8}.\end{aligned} \tag{3.6}$$

The $J_{x,a}$ terms account for interactions between atoms that are neighbors in the $\hat{x}$ direction and the $J_{y,a}$ terms account for interactions between neighbors in the $\hat{y}$ direction.

Diagonalizing the Hamiltonian with the parameters in Table 3.1 yields the state diagram in Figure 3.13. The four lowest-lying states are the two Neél like states in which every atom is aligned antiferromagnetically to it's neighboring atoms, and two states in which the additional weakly-coupled atom is anti-aligned. The close proximity of these states to one another is what allows transitions between the ground and first excited state to occur, as although these two do not have any direct overlap (a matrix element close to zero), they do overlap with these nearby states. The observed transitions are on the seconds timescale, many orders of magnitude slower than scattering with both the bath and tunnel electrons [11], meaning that only a small amount of coupling is necessary to yield the measured dynamics.

To model the scattering processes, product states $|\sigma_i, \phi_i\rangle = |\sigma_i\rangle \otimes |\phi_i\rangle$ of the spin of the scattering electron and the sample spin are used as a basis for the tunneling process (the sample spin is one of the structure's atoms). The exchange interaction is modelled as a perturbation, allowing Fermi's golden rule [12] to be applied, yielding a transition between initial state i and final state f of:

$$Y(\phi_f, \sigma_f, \phi_i, \sigma_i) = |\langle \phi_f, \sigma_f | \hat{\mathbf{S}} \cdot \hat{\boldsymbol{\sigma}} + u\mathbb{1} | \phi_i, \sigma_i \rangle|^2. \tag{3.7}$$

$\hat{\boldsymbol{S}} \cdot \hat{\boldsymbol{\sigma}}$ is the exchange interaction between the spin of the structure and the tunnel electrons, and u gives spin contrast. Calculating the transition intensity as a function of magnetic field then allows the time-dependent transition rates to be mapped back to an effective exchange field applied with the tip. The exchange field was modelled as [2]:

$$\boldsymbol{B_{exch}} = B_0(e^{-\frac{(z+z_0)}{\gamma}}) \cdot (\cos(\theta)\hat{x} + \sin(\theta)\hat{y}), \tag{3.8}$$

which yields a local field for the atom underneath the tip of:

$$\boldsymbol{B_{local}} = \boldsymbol{B} + \boldsymbol{B_{exch}}. \tag{3.9}$$

Note the use of θ to account for a misalignment between the field applied by the spin-polarized tip and the external magnetic field $\boldsymbol{B}$, which can be substantial. [3, 13]

Figure 3.15 shows the results of modelling the scattering process. The equation for $\boldsymbol{B_{exch}}$ was used to perform a least-squares fit to the time-dependent transition rates with the z-position and the modeled field-dependent scattering rates as an input, allowing the form of the time-dependent exchange field to be determined. The model reproduces both the shape and approximate magnitude of the time-dependent transition rates. To accurately model the transitions observed here $\theta = 45°$ was used. Higher-order scattering processes are the primary driver between ground and excited state for the $2 \times 4 + 1$, as there is no direct overlap between the ground and excited states. The black curves in the plot show the sum of all processes with one intermediary state.

The model indicates that the first three excited states are within a few meV window of the ground state throughout the modulation period. The effective barrier of $\varepsilon = 1.35$ meV extracted in the previous section corroborates the involvement of the lower-lying states in yielding an effectively classical behavior. The net effect of these transitions via intermediary states is equivalent to a classical transition over an energy barrier, albeit with a reduced barrier height relative to the allowed transitions for inelastic scattering with an electron. Inelastic transitions would have to go over the energy barrier via states that obey the selection rule $\Delta m = -1, 0, +1$, where m is the expectation value of the $\hat{S}_x$ operator. The classically allowed path can be visualized and compared to the measured barrier height by calculating the Néel vector for each eigenstate's spin configuration. This allows the number of spin flips necessary to perform a transition between any two states to be determined. The Néel vector is a helpful tool for analyzing compensated or nearly-compensated antiferromagnets, as the net spin does not account for the exchange interaction. Here we define the Néel operator with respect to the x-axis as the ground state magnetization points along this direction:

$$\langle \hat{S}_N \rangle = \sum_a \langle \hat{S}_{x,a} \rangle (-1)^a \tag{3.10}$$

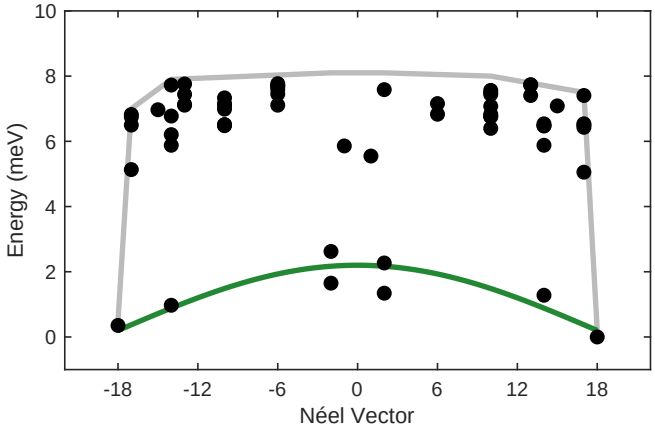

Figure 3.14. Eigenstate energy as a function of the x-axis projection of the Néel vector for the 60 lowest states in energy. The grey curve is a schematic representation of the classical energy barrier with stepwise reversal of the atom's magnetic moments. The green curve is a sketch of the effective barrier height including magnetic tunneling transitions. $B_x = 500$ mT.

where a is the a^{th} atom in the structure. The expectation value of this operator shows which states have allowed transitions between them, as the value will differ by ± 1. Figure 3.14 shows the Néel vector at $B_x = 500$ mT for the eigenstates in Figure 3.13. For nine $S = 2$ atoms in an antiferromagnet the Néel vector ranges from $+18$ to -18, at the excited and ground state, respectively. The classical anisotropy barrier between the two states is in this case approximately 8 meV (grey); the intermediary low energy states reduce the effective barrier height by approximately 6.65 meV (green).

The model slightly underestimates the amplitude of the transition rates, this is possibly due to further higher-order scattering pathways being present, such as intra-structure excitations or hot-electron injection. The curvature of the relaxation rate is also inverted, this is likely due to the approximation of the exchange-field as an external field breaking down for large fields. Overall, we can determine that the exchange field $\boldsymbol{B_{exch}}$ ranges from approximately -500 mT when the tip is further away, to -1500 mT when the tip is close (a $\boldsymbol{B_{local}}$ of 500 mT and -1000 mT, respectively).

It is worth noting that the classical behavior observed here, as demonstrated by the temperature dependence of the rates, is not only due to the $2 \times 4 + 1$'s size and lack of direct overlap between ground and excited state yielding an effectively negligible tunneling rate. Theoretical investigations into spins on surfaces that con-

sider the renormalization of transition energies between spin states as a function of coupling strength to the electron bath of the Cu substrate [14], suggest that the coupling for this nine-atom structure is so strong that magnetic tunneling is not simply small, but actually zero. This distinction may seem arbitrary, but it has significant implications regarding the nature of this nanostructure as the transition from small to zero magnetic tunneling marks a quantum phase transition. Indeed, measuring spin dynamics using stochastic resonance provides experimental access to the noise sources that act on a spin and therefore access to the processes that underlie the spin-boson coupling at the heart of open quantum systems.

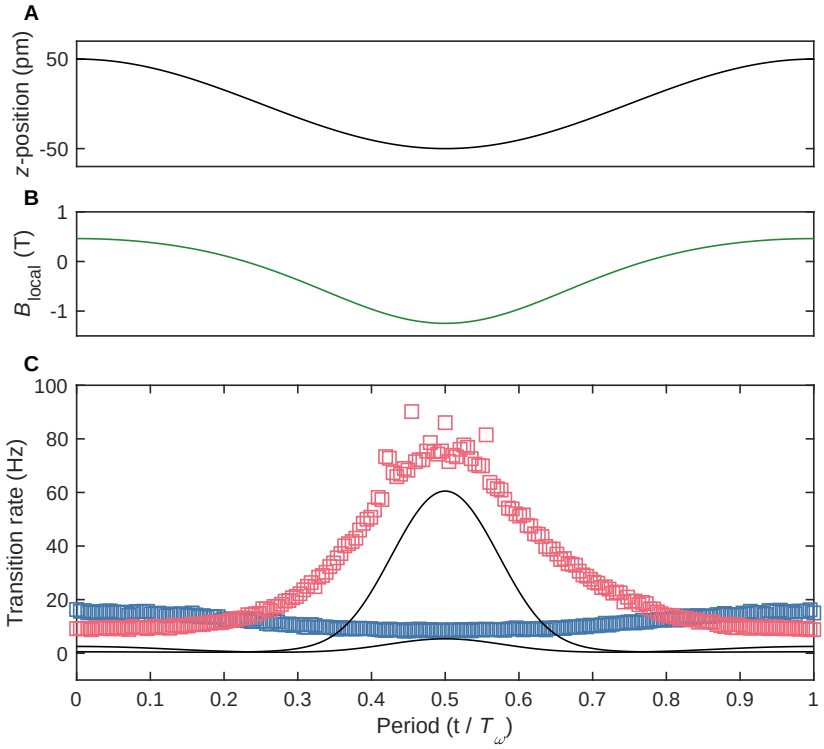

Figure 3.15. Modelling tip modulation and scattering. (**A**) Z -position during one period of modulation. (**B**) Calculated local field during one period of modulation. (**C**) Conditional transition rates calculated using Equation 3.7 (black, $\gamma = 70 \pm 5$ pm, $B_0 = 1100 \pm 10$ mT, z_0 fixed to 0), with measured excitation rate (red) and measured relaxation rate (blue).

3.6. CONCLUSION

The $2 \times 4 + 1$ exhibits a clear stochastic resonance. This extension of stochastic resonance to atomic scale spins yielded insight into the cooperative effect between a thermal noise source and a modulated magnetic exchange field. The structure's behavior is analogous to a host of classical stochastic resonance systems [5, 15] where the relative energy of two bistable states is modulated over time.

Recall there are two primary ways of inducing stochastic resonance in spin systems, modulating the transition matrix element and modulating the noise power. Here, Tesla magnitude fields could be modulated quickly by moving the STM's spin-polarized tip relative to the $2 \times 4 + 1$, shifting the relative energy of the spin states in the meV range, and thereby modulating the transition matrix element. The results of this modulation, namely the dynamic evolution of the spin as it undergoes stochastic resonance, were modelled effectively using the transition-rate theory established in Chapter 2, with both the onset at low frequencies and the disappearance at high frequencies being reproduced. Agreement with theory indicated Markovian dynamics, with the noisy bath reaching equilibrium between scattering events with the nanostructure. The synchronization effect was significant, with the spin-state locking efficiently to the drive. This yielded a direct window into the noise sources driving the stochastic behavior of this nano-antiferromagnet. The noise source was identified as thermally assisted transitions over an anisotropy barrier. Temperature-dependent measurements revealed the noise's classical character, while scattering simulations corroborated the effect of nearby low-energy spin states in lowering the effective barrier height.

REFERENCES

[1] S. Loth, S. Baumann, C. P. Lutz, D. M. Eigler, and A. J. Heinrich, *Bistability in Atomic-Scale Antiferromagnets*. Science **335**, 196 (2012).

[2] S. Yan, D.-J. Choi, J. A. J. Burgess, S. Rolf-Pissarczyk, and S. Loth, *Control of quantum magnets by atomic exchange bias,* Nature Nanotechnology **10**, 40 (2014).

[3] K. Yang, W. Paul, F. D. Natterer, J. L. Lado, Y. Bae, P. Willke, T. Choi, A. Ferrón, J. Fernández-Rossier, A. J. Heinrich, and C. P. Lutz, *Tuning the Exchange Bias on a Single Atom from 1 mT to 10 T,* Physical Review Letters **122**, 227203 (2019).

[4] D. M. Eigler and E. K. Schweizer, *Positioning single atoms with a scanning tunnelling microscope,* Nature **344**, 524 (1990).

[5] L. Gammaitoni, P. Hänggi, P. Jung, and F. Marchesoni, *Stochastic resonance,* Reviews of Modern Physics **70**, 223 (1998).

[6] S. Arrhenius, *Über die Reaktionsgeschwindigkeit bei der Inversion von Rohrzucker durch Säuren,* Zeitschrift für Physikalische Chemie **4U** (1889).

[7] S. Loth, C. P. Lutz, and A. J. Heinrich, *Spin-polarized spin excitation spectroscopy,* New Journal of Physics **12**, 125021 (2010).

[8] C. F. Hirjibehedin, C. P. Lutz, and A. J. Heinrich, *Spin Coupling in Engineered Atomic Structures,* Science **312**, 1021 (2006).

[9] D. Gatteschi, R. Sessoli, and J. Villain, *Mesoscopic Physics and Nanotechnology* (Oxford University Press, Oxford, 2006).

[10] D. Griffiths, *Introduction to Quantum Mechanics* (Prentice Hall, 2005).

[11] M. Ternes, *Spin excitations and correlations in scanning tunneling spectroscopy,* New Journal of Physics **17**, 63016 (2015).

[12] J. Appelbaum, *Exchange Model of Zero-Bias Tunneling Anomalies,* Physical Review Letters **154**, 633 (1967).

[13] P. Willke, A. Singha, X. Zhang, T. Esat, C. P. Lutz, A. J. Heinrich, and T. Choi, *Tuning Single-Atom Electron Spin Resonance in a Vector Magnetic Field,* Nano Letters **19**, 8201 (2019).

[14] F. Delgado and J. Fernández-Rossier, *Spin decoherence of magnetic atoms on surfaces,* Progress in Surface Science **92**, 40 (2017).

[15] B. McNamara and K. Wiesenfeld, *Theory of stochastic resonance,* Physical Review A **39**, 4854 (1989).

4

SEMI-CLASSICAL SR

4.1. THE 1 × 5 NANOSTRUCTURE

Having used time-resolved spin-polarized STM to see that classical stochastic resonance can indeed be induced on the atomic scale with the $2 \times 4 + 1$, we now want to explore the onset of quantum behavior. We define the two regimes by the temperature dependent behavior of the transition rates. In particular, for spin transitions, the classical region is defined as the regime where the transition rates trend to zero as the temperature goes to zero. [1] Conversely, in the quantum region investigated here, transition rates remain finite.

We investigate a structure which straddles the crossover from quantum to classical behavior. It is susceptible to scattering with tunnel electrons that result in a direct transition between the ground and excited state, as well as an indirect transition via higher energy intermediary states due to thermally excited electrons. The onset of these direct transitions is a signature of quantum systems where the eigenstates are superpositions between the integer quantum number states, and is a clear indicator of quantum behavior.

4.2. CONTROLLING THE 1 × 5 NANOSTRUCTURE

The structure investigated here (referred to as the 1×5) is comprised of five Fe atoms adsorbed on Cu-site's of the Cu_2N surface. There is one unoccupied Cu-site between each Fe atom, and they are placed evenly along the axis defined by the crystal axis of the Cu_2N surface. The structure is built along the axis with alternating N and Cu atoms (shown schematically in Figure 4.1). The exchange coupling

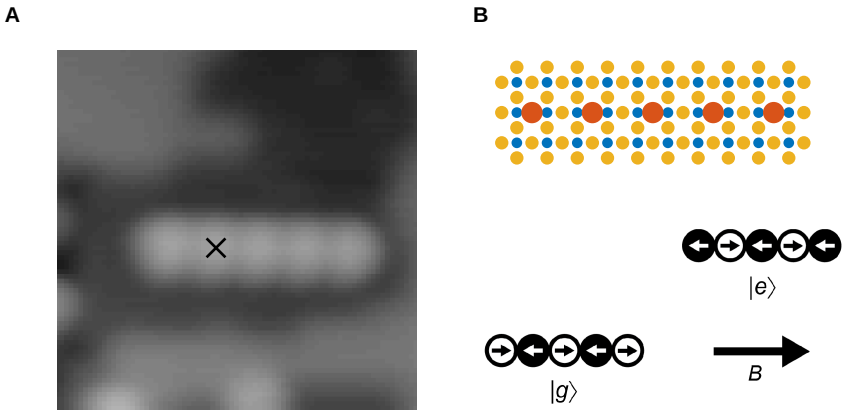

Figure 4.1. (**A**) Constant-current topography of the 1×5 nanostructure, comprised of five Fe atoms. Scan frame is 6x6 nm. All subsequent measurements are acquired on the atom marked with a cross. V_{set} = 100 mV, I_{set} = 100 pA. (**B**) Schematic representation of the ground and excited state, with the color indicating magnetic moment orientation, and the black arrow showing the external magnetic field. The ball and stick model of the surface and structure indicates N atoms (blue), Cu atoms (orange) and Fe atoms (red). B_x = 500 mT, $T = 2.5$ K.

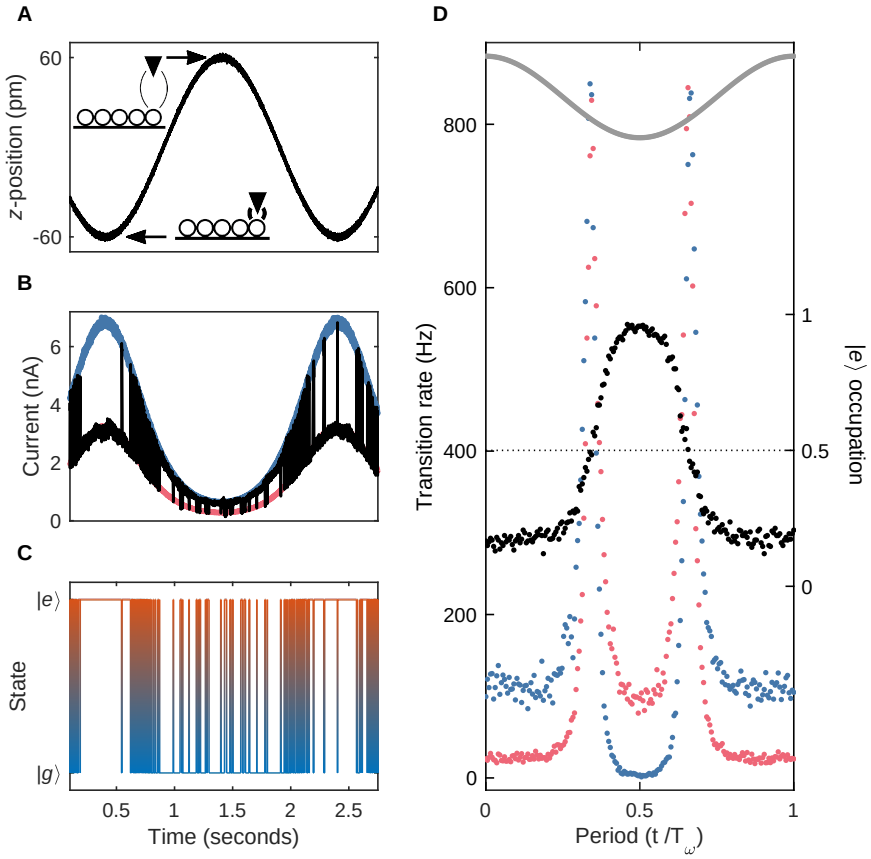

Figure 4.2. Applying an exchange bias field via a low frequency, $\omega = 0.5$ Hz tip modulation: (**A**) One period of modulation of the z-position in the STM, $dz = 60$ pm. (**B**) Current measured during the z-modulation (black), excited state conductivity is shown in red, ground state conductivity in blue. (**C**) Occupation of the ground $|g\rangle$ (blue) and excited $|e\rangle$ (red) state during the z-position modulation. (**D**) Time dependent conditional transition rates for transitions from the higher conductivity (ground) state to the lower conductivity (excited) state are shown in red. Transition rate from the lower conductivity (excited) to the higher conductivity (ground) state are shown in blue. The time-dependent average occupation of the excited state is shown in black, with a schematic of the tip position shown in grey. $V_{set} = 20$ mV, $I_{set} = 50$ nA, $V_{dc} = 1$ mV, $T = 2.5$ K, $B_x = 500$ mT.

between the atoms is antiferromagnetic, resulting in a ground state of alternating magnetic moments. In Figure 4.1B the ground state and the first excited state are shown schematically. The ground state features three atoms with magnetic moment aligned along the magnetic field direction, and two in the opposite, while the first excited state has the inverse spin texture. The chain has one magnetically uncompensated atom, making the Zeeman splitting of the two low-energy states comparable to that of a single Fe atom.[1]. Compared to a single Fe atom, the additional atoms reduce the transition matrix element between those two states, greatly reducing the "tunneling" transitions. They also provide additional scattering channels for the bath electrons, thereby increasing coupling to the noise-source presented by the bath. Conceptually, it is helpful to think of the chain as similar to one Fe atom but with reduced "tunneling" between ground and excited state, as well as a more significant coupling to the noisy thermal bath.

Analogously to the $2\times4+1$ in the previous chapter, the 1×5 structure will also be interacted with via exchange interaction with a spin-polarized STM tip. Here, the tip will again modify the relative energy between the eigenstates, which will be reflected in the dynamic evolution of the structure. Figure 4.2 shows a low frequency tip modulation (Panel A) applied to the 1×5, where the modulation rate is much slower than the structure's transition rates. When the tip is closer to the structure, the low conductivity state (red) is preferentially occupied, while the high conductivity state (blue) is favored when the tip is far away (Panels B-C). As in the previous chapter, we define the ground state $|g\rangle$ as the preferentially occupied state when the tip is far away. Here again the high conductivity state is the ground state $|g\rangle$ and the low conductivity state is the excited state $|e\rangle$.

The general behavior of these transition rates is similar to that of the $2\times4+1$, matching with thermally activated processes over a barrier. The transition rates nominally track the modulation, and the occupation crosses 0.5 when the rates cross parity. There are however two features which contrast starkly with the classical-noise model, namely the large peaks when the occupation crosses 0.5. This indicates that there are two processes at play: a thermally activated transition driven by classical noise, and a second process that dominates when the occupation of the states is approximately equal. Here we will focus on the origin of this second process and the effects it has on the dynamics of the structure.

Looking at the time-dependent conditional transition rates in Panel D, one can see that not only is there a significantly enhanced transition rate at two points in the period, they in fact are over an order of magnitude faster than during the rest of the period. These enhanced transitions occur approximately when the tip has moved about 33% through its modulation period, and again at around 66%. As the occupation crosses 0.5, the first conclusion we can draw is that the exchange field is sufficiently strong to reverse the order of the states in energy, i.e. $|g\rangle$ is lower in energy when the tip is far away and the exchange field is weak and $|e\rangle$ is lower in

[1] See Section 4.4 for more details on the energy level structure

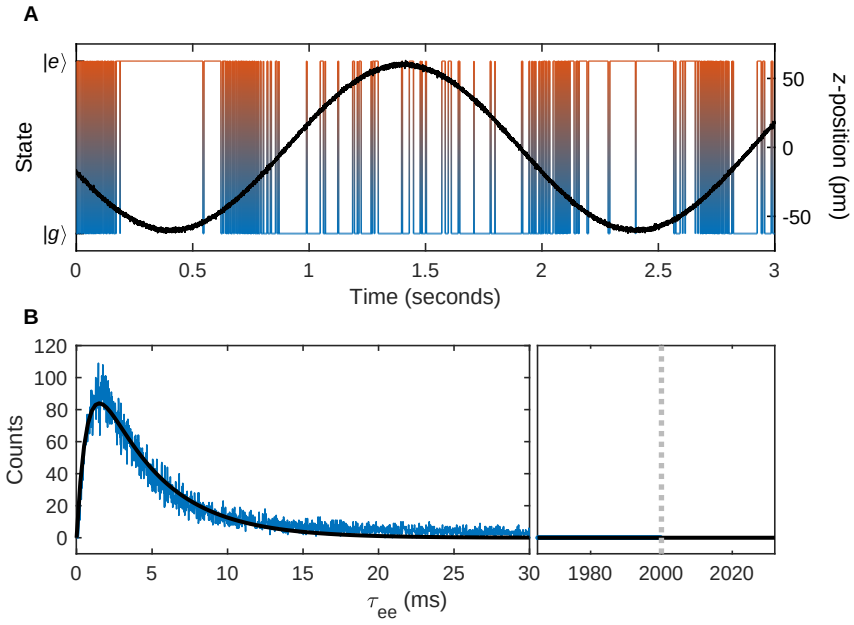

Figure 4.3. (**A**) Exemplary time trace of the z-position (black) and spin state ((|g⟩ blue to |e⟩ red)) measured with a low frequency harmonic drive . (**B**) Histogram of the time between excitation events τ_{ee}(blue) least-squares fit with a hypoexponential curve (Equation 2.2, black, $\overline{\tau}_e = 0.71 \pm 0.02$ ms, $\overline{\tau}_g = 4.07 \pm 0.05$ ms, $c = 0.494 \pm 0.003$ counts·seconds). Period of harmonic drive, $T_\omega = 2$ s, is indicated with a dotted grey line. $\omega = 0.5$ Hz, $dz = 60$ pm, $V_{dc} = 1$ mV, $V_{set} = 20$ mV, $I_{set} = 50$ nA, $B_x = 500$ mT, $T = 2.5$ K.

energy when the tip is closer and the exchange field is strong. It is exactly at the crossover between these two regimes that the switching rates drastically increase. As these increased rates are only observed at these points, this suggests that direct transitions between the two states become possible due to the mixing introduced by transverse anisotropy. In total, this indicates that the dynamics of this spin result from both classical thermally-activated processes and non-thermal quantum mechanical direct transitions.

4.3. INDUCING STOCHASTIC RESONANCE

Looking more closely at the time trace (Figure 4.3), these extremely frequent transitions can be clearly observed. At first glance, one may think that the drive has synchronized the spin state, as the excited state is indeed preferentially occupied during the extension portion of the tip modulation, and the ground state during the retraction. However, when analyzing the distribution of times between excita-

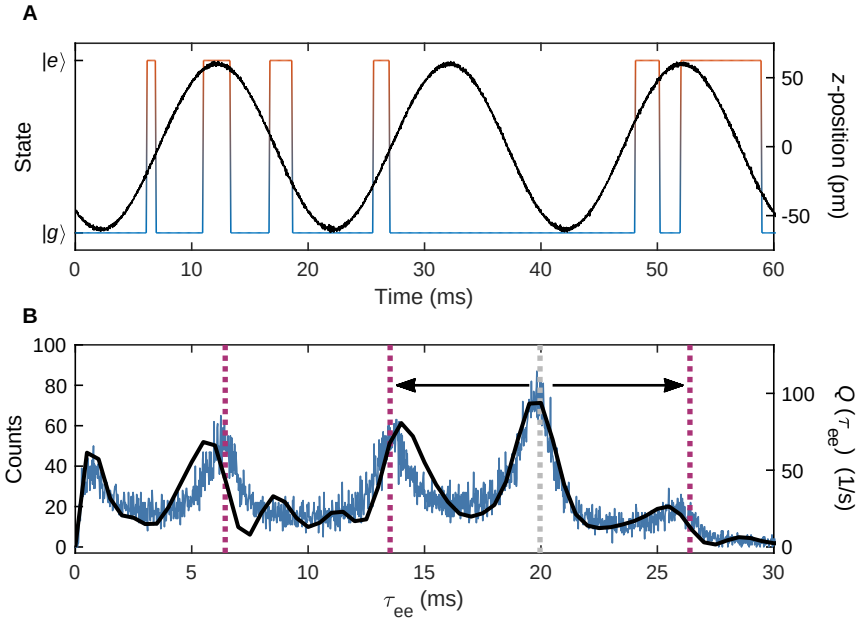

Figure 4.4. (**A**) Exemplary time trace of the z-position (black) and spin state ($|g\rangle$ blue to $|e\rangle$ red) measured with a harmonic drive. (**B**) Histogram of the time between excitation events measured (blue), and analytically modelled $Q(\tau_{ee})$ using conditional transition rates (Equation 2.12, black). Grey dotted line indicates the drive frequency $\omega = 50.1$ Hz. Purple dotted lines indicate additional peaks. $dz = 60$ pm, $V_{dc} = 1$ mV, $V_{set} = 20$ mV, $I_{set} = 50$ nA, $B_x = 500$ mT, $T = 2.5$ K.

tion's, one can see that the broadband switching introduced when the spin states are close to degenerate completely overwhelms any kind of synchronization effect. The goodness of fit when using a hypoexponential function confirms that there is no synchronization, and that both excitation and relaxation simply sample Poisson distributions with their respective time constants of $\overline{\tau}_e = 0.71 \pm 0.02$ ms and $\overline{\tau}_g = 4.07 \pm 0.05$ ms.

In Figure 4.4 the drive frequency is increased to 50 Hz. For comparison, the excitation rate is approximately 25 Hz when the tip is far away, while the relaxation rate is around 110 Hz. The switching behavior here contrasts strongly with that of typical classical systems that undergo stochastic resonance. Usually, these systems preferentially switch to one state during one half wave of the modulation, and preferentially switch to the other state in the other half wave. Here we have a strongly enhanced switching when the states are degenerate, which does not favor a particular state, but rather mostly acts as a randomizer, as exemplified by the even occupation of both states at this point in the period.

Looking at the blue histogram data in Panel B, one can see a highly structured curve with several pronounced peaks. The largest peak is indeed at the modulation period of 20 ms (dotted light grey line). It is remarkable that stochastic resonance can emerge in this system, despite the strong randomization happening twice per modulation period. There are however, additional peaks both below and above the modulation period (marked with purple dotted lines). The peaks contrast with the typical structure of a stochastic resonance histogram in that the peak above the modulation period is not an integer multiple thereof, as well as the presence of multiple peaks below the modulation period. They are reproduced by the stochastic resonance model[2] applied to the rates structure, suggesting that they are indeed a consequence of the underlying physics, rather than any sort of measurement artifact. The peaks can be found at approximately 6, 14, 20 (the modulation period), and 26 ms. The region where direct transitions dominate is roughly one third of the modulation period (more precisely, 6.4 ms), which results in a peak at $\frac{T_\omega}{3}$, as well as side bands at the sum (20+6.4=26.4 ms) and difference (20-6.4=13.6 ms) with the modulation period (indicated with arrows in Figure 4.4). The stochastic resonance model for $Q(\tau_{ee})$ is able to reproduce this response, but slightly under-estimates the location of the higher-multiple peak, and therefore the peaks are slightly shifted relative to the measured data.

This behavior can be confirmed by looking at selected curves in a frequency sweep (Figure 4.5A). The curve measured at 199 Hz shows this behavior most clearly. One can see the typical series at integer multiples of the modulation period (5, 10, 15 ms,...), and each peak has side-bands at roughly 1.7 ms above and 1.7 ms below the primary peaks. Not only does the synchronization effect have to compete with the broadband stochasticity, it also competes with these "side-bands" driven by direct transitions between the spin states.

[2] See Section 2.3 for derivation

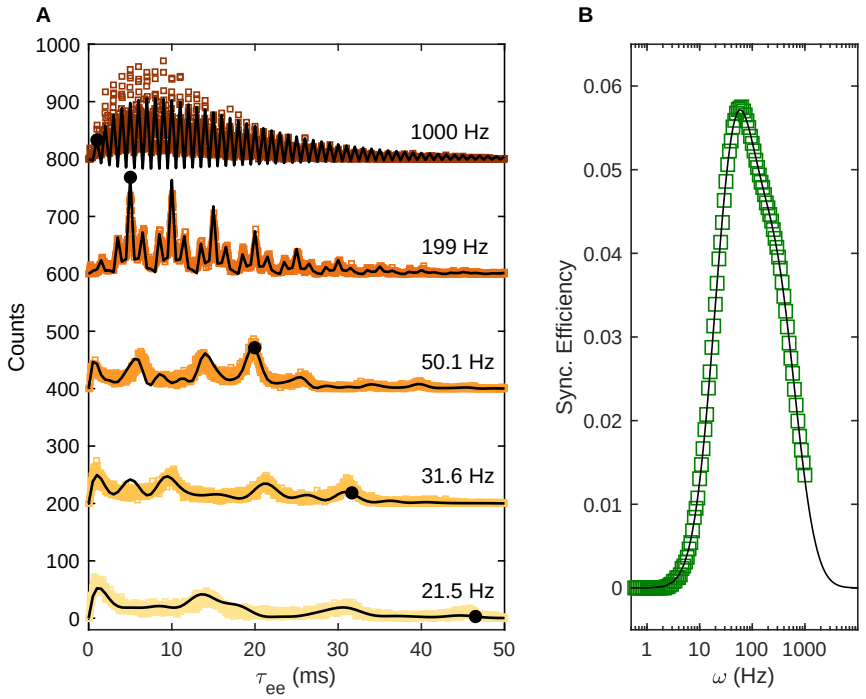

Figure 4.5. (**A**) Histograms of the time between excitation events for five frequencies (black dots indicate period), offset for clarity. The black curves are analytically modelled $Q(\tau_{ee})$ (scaled to account for measurement duration) using the measured conditional transition rates. (**B**) Frequency dependent synchronization efficiency (green) with a least-squares fit to Equation 4.1 (black, $\omega_0 = 48 \pm 1$ Hz, $\sigma_0 = 0.41 \pm 0.01$ $\log_{10}$·Hz, $c_0 = 0.053 \pm 0.001$, $\omega_1 = 305 \pm 1$ Hz, $\sigma_1 = 0.37 \pm 0.01$ $\log_{10}$·Hz, $c_0 = 0.032 \pm 0.001$). $dz = 60$ pm, $V_{dc} = 1$ mV, $V_{set} = 20$ mV, $I_{set} = 50$ nA, $B_x = 500$ mT, $T = 2.5$ K.

Looking at the synchronization efficiency in Figure 4.5B (relative intensity at the black dots in Panel A), at first glance one sees the typical log-normal peak characteristic of undergoing stochastic resonance. On further inspection, one can also see different slopes where the synchronization efficiency deviates from a log-normal curve, in particular right after the stochastic resonance condition is met, at around 50 Hz. Between 50 and approximately 300 Hz, the synchronization effect decreases faster than the slope suggested by a single log-normal curve. There appears to be a shoulder at 300 Hz, which could be a consequence of competition between the different noise sources. As the drive de-synchronizes with the dominant noise peaking at 50 Hz, it has a window in which it synchronizes with a weaker noise source peaking at 300 Hz. To model this behavior, a modified version of Equation 3.1 was used, which is the sum of two log-normal functions:

$$\chi_2(\omega) = c_0 \cdot e^{-\frac{1}{2}\left(\frac{\log_{10}(\omega)-d_0}{\sigma_0}\right)^2} + c_1 \cdot e^{-\frac{1}{2}\left(\frac{\log_{10}(\omega)-1_0}{\sigma_1}\right)^2}. \tag{4.1}$$

Analogously to ω_0, ω_1 is defined as 10^{d_1}. The black curve in Figure 4.5 is a least-squares fit to $\chi_2(\omega)$, which was able to quantitatively reproduce the form of the frequency-dependent synchronization efficiency for this structure. The fit found resonance frequencies at $\omega_0 = 48 \pm 1$ Hz and at $\omega_1 = 305 \pm 1$ Hz, in agreement with the picture of two competing noise sources at different time-scales.

Synchronization to the drive also has consequences for the average occupation of the spin states. Figure 4.6 shows snapshots of the time-dependent occupation (within one period of modulation) both for low frequency (Panel A left) and resonant (right) modulation. For the low frequency modulation one can see that the occupation clearly tracks the modulation one-to-one, it is in phase (see Panel B for the phase as a function of frequency). As the frequency increases, there are two prominent effects: the average occupation of the excited state increases, and the phase shift (Panel B) between the drive and the spin state increases asymptotically. In addition, there is a third notable feature at low frequencies which can be seen in the occupation, namely a dip at around 20 Hz. This can be pictured as a sort of stochastic resonance in which the slow excitation rate (also approximately 20 Hz when the tip is far away) is in synchronization with the modulation, and the fast excitations at the zero-field crossings are simply "noise". Although this effect modulates the occupation, the synchronization efficiency is unaffected by this (Figure 4.5B), due to the de-synchronization caused by the fast transitions.

4.4. MODELLING THE SCATTERING

Let's take a closer look at the underlying scattering process. First, the state diagram was modelled using the Spin Hamiltonian formalism described in previous chapters with the parameters shown in Table 4.1. Parameters were determined iteratively, starting with values for similar structures from literature [2, 3], and performing successive least-squares fits to the measured transition rates using the modelled tip interaction as in Section 3.5.

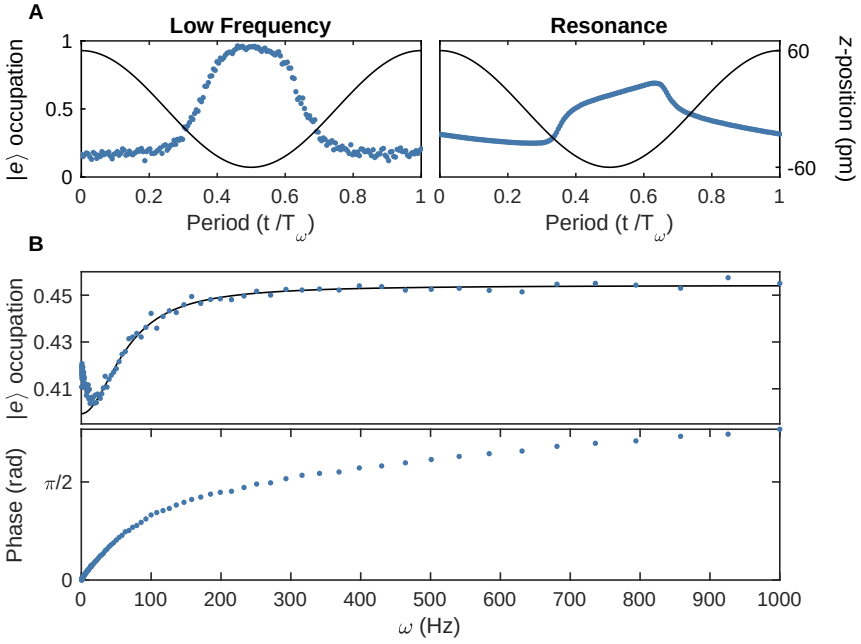

Figure 4.6. (**A**) Occupation modulation during one period of drive at low frequency ($\omega = 0.5$ Hz) and at resonance ($\omega = 50.1$ Hz). (**B**) Top: excited state occupation as a function of modulation frequency (blue). Black line is a least-squares fit to Equation 3.2 with $\Gamma = 64 \pm 3$ Hz, $L = -22 \pm 2$ Hz, $L_0 = 0.454 \pm 0.001$). Bottom: Relative phase shift between the excited state occupation and the drive. $dz = 60$ pm, $V_{dc} = 1$ mV, $V_{set} = 20$ mV, $I_{set} = 50$ nA, $B_x = 500$ mT, $T = 2.5$ K.

Parameter	atom 1	atom 2	atom 3	atom 4	atom 5
S	2	2	2	2	2
g	2.05	2.05	2.05	2.05	2.05
D (meV)	-1.82	-2.0	-2.0	-2.0	-1.82
E (meV)	0.217	0.217	0.217	0.217	0.217
J_x (meV)	0.76	0.76	0.76	0.76	-

Table 4.1. Spin Hamiltonian Parameters for the 1×5 nanostructure. J_x is the coupling between the atom specified in the column header and the next atom in the $+x$ direction (see Equation 4.2).

For this structure the Heisenberg exchange interaction has the form:

$$\hat{H}_j = J_{x,1}\hat{\mathbf{S}}_\mathbf{1} \cdot \hat{\mathbf{S}}_\mathbf{2} + J_{x,2}\hat{\mathbf{S}}_\mathbf{2} \cdot \hat{\mathbf{S}}_\mathbf{3} + J_{x,3}\hat{\mathbf{S}}_\mathbf{3} \cdot \hat{\mathbf{S}}_\mathbf{4} + J_{x,4}\hat{\mathbf{S}}_\mathbf{5} \cdot \hat{\mathbf{S}}_\mathbf{6}. \tag{4.2}$$

The atom's are modelled as effective spin S=2, and g-factor 2.05 as in literature [2, 3]. Spin-orbit-coupling is accounted for by means of the anisotropy parameters symmetry and the effective g-factor [4]. D is different for the atoms at the edge of the nanostructure (atom's 1 and 2) as they experience an effectively modified crystal field, and therefore different uniaxial anisotropy, due to their location. Figure 4.7 shows the resulting spin state eigenenergies, for an external magnetic field ranging from -2 to $+2$ T. Within this band, the ground and first excited state are well separated from any higher lying states, by approximately 5 meV. As the magnetic field approaches zero, so too does the separation between ground and excited state.

This state diagram shows the effect of an external magnetic field B_x, and can be used to simulate the excitation and relaxation rates as a function of field using Equation 3.7. To do this, we want to determine the time-dependent exchange field applied by the tip. Panel A of Figure 4.8 shows the z-position during one period of modulation. This is mapped to a time-dependent magnetic field (Panel B) by performing a least-squares fit of Equation 3.9 to the transition rates measured on atom 2 (Panel C) with the z-position and modelled scattering rates as input.

The simulation yielded a tip exchange field of up to -2.5 T. The curvature and onset of the increased transition rates was well reproduced by the model, but similar to the $2 \times 4 + 1$ the high-field behavior (when the tip is closest to the structure) was difficult to quantitatively replicate. This is likely due to approximating the local field as a field experienced by the whole structure, which breaks down for large local fields. A further correction could be introduced by the presence of the electron-bath of the tip itself. When the tip is very close to the structure, it can act similarly to the substrate, and present a noisy thermal bath that scatters with the spin. This second bath could drive the observed increase in both excitation and relaxation rates.

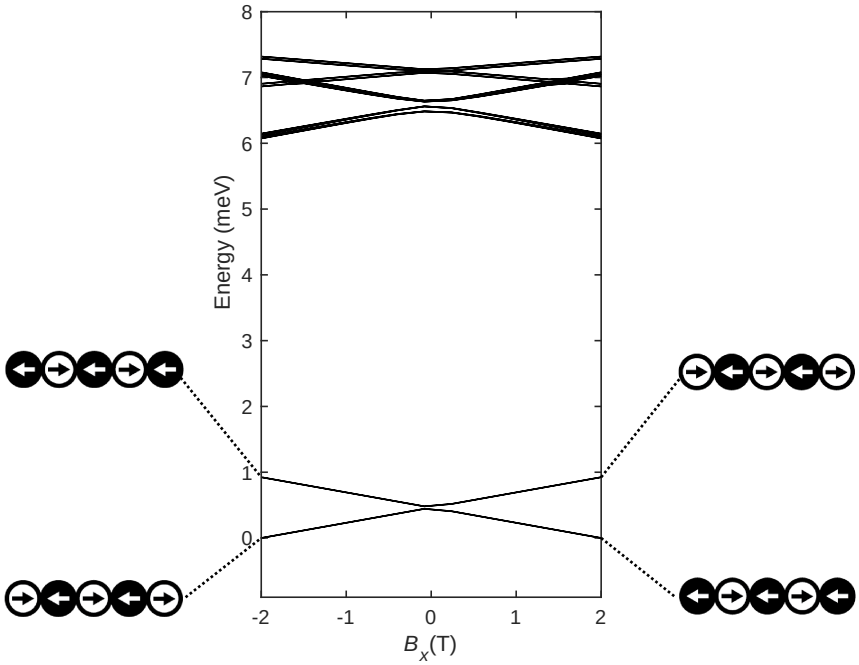

Figure 4.7. State eigenenergies as a function of external magnetic field, calculated by diagonalizing the localized spin system Hamiltonian. Schematic annotations show the magnetic moment of each state.

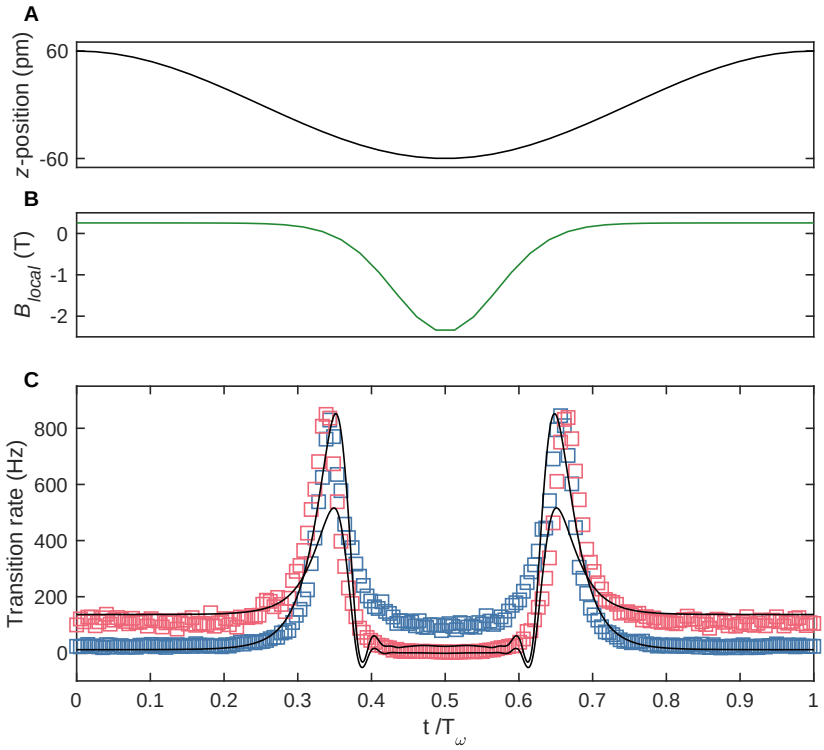

Figure 4.8. Modelling tip modulation and scattering (**A**) z-position during one period of modulation. (**B**) Calculated exchange field during one period of modulation. (**C**) Conditional transition rates calculated using Equation 3.7 (black, $\gamma = 11.8 \pm 0.35$ pm, $B_0 = 1.7 \pm 1$ mT, $z_0 = -27 \pm 1$ pm), with measured excitation rate (red) and measured relaxation rate (blue).

4.5. CONCLUSION

We found both classical and quantum transitions within a single structure, which acted as two simultaneous sources of noise. Thermally assisted transitions over an effective barrier dominate the noise when the states are well separated in energy, while direct quantum tunneling transitions across the barrier dominate when the states are close to degenerate. The classical transitions appeared as a smooth tracking of the tip exchange field, while quantum transitions resulted in sharp peaks at two points during the modulation cycle. The simultaneous presence of both these effects led to our characterization of this structure as semi-classical.

Notably, this structure which exhibits both quantum and classical effects can be brought into resonance. The drive itself is introducing a strong randomization of the spin twice per drive period by enabling these fast tunneling transitions, yet synchronization can still be achieved. The synchronization peaks at the characteristic frequency of these fast transitions driven by quantum noise, rather than the slower classical ones, as these have such a strong effect on the stochasticity. If the drive is not cooperating with the fast noise, it will be strongly hindered by it.

The stochastic resonance behavior was reproduced by the transition rate theory derived in Chapter 2, including the appearance of side-bands not present in the $2\times4+1$ structure. The overall synchronization efficiency is significantly smaller than that of the $2\times4+1$ but is nonetheless present. Here too, similar to the $2\times4+1$, the excellent agreement with the transition rate model indicates Markovian dynamics. Neither the classical transitions over the barrier or direct transitions across have any "memory" of previous transitions. The drive frequency dependent occupation was purely Lorentzian-shaped for the $2\times4+1$, whereas the 1×5 had a low-frequency feature characteristic of a weak synchronization with the classical noise.

This demonstrates that stochastic resonance is sensitive to the presence of more than one noise source, extending the generality of this effect from a cooperative effect with a single source of noise, to one with multiple.

REFERENCES

[1] L. Bokacheva, A. D. Kent, and M. A. Walters, *Crossover between Thermally Assisted and Pure Quantum Tunneling in Molecular Magnet Mn12-Acetate,* Physical Review Letters **85**, 4803 (2000).

[2] S. Yan, L. Malavolti, J. A. J. Burgess, A. Droghetti, A. Rubio, and S. Loth, *Nonlocally sensing the magnetic states of nanoscale antiferromagnets with an atomic spin sensor,* Science Advances **3**, e1603137 (2017).

[3] L. Malavolti, G. McMurtrie, S. Rolf-Pissarczyk, S. Yan, J. A. Burgess, and

S. Loth, *Minimally invasive spin sensing with scanning tunneling microscopy,* Nanoscale **12**, 11619 (2020).

[4] S. Loth, C. P. Lutz, and A. J. Heinrich, *Spin-polarized spin excitation spectroscopy,* New Journal of Physics **12**, 125021 (2010).

5

QUANTUM TO CLASSICAL CROSSOVER IN A SINGLE ATOM

5.1. A "SLOW" SINGLE ATOM

Fe atoms preferentially adsorb above the Cu atoms (Cu-site) in the Cu_2N lattice, of which there are two distinct types with respect to an external magnetic field. These are characterized by whether there are N atoms in the $\pm x$ direction, or the $\pm y$ direction (see axis in Figure 5.1). Both the nanostructures discussed in this thesis, as well as many others in literature, are composed of one or more Fe atoms adsorbed on one of these two types of adsorption sites. There is, however, a third meta-stable adsorption site, above the N atoms (N-site, the red Fe atom in the overlay is adsorbed on this site). First discussed in [1], this adsorption site was effectively discarded as a platform for magnetism experiments, as it is both difficult to ensure the Fe atoms remain there, and no inelastic magnetic signals had been detected. Indeed, measurement with a non spin-polarized tip show no characteristic magnetic features (Figure 5.1). In Rejali's 2020 work [2] an analogous adsorption site was re-visited, leading to the experiments performed here. When a sufficiently spin-polarized tip is used to measure an Fe atom on the N-site, distinct features in the mV regime appear,and stochastic switching can be induced. Of particular relevance for stochastic resonance experiments, is that this switching occurs on the ms-timescale. Up until this point in the thesis, the anti-ferromagnetic exchange interaction between the Fe atoms on the surface was used to slow-down their dynamic evolution. The collective motion brings the dynamics into the few-kHz window set by the transimpedance amplifier used to amplify the tunnel current. Single Fe atoms on the same Cu-site, on the other hand, have switching in the pico- to nanosecond range [3]. The stochastic switching observed on the N-site, however,

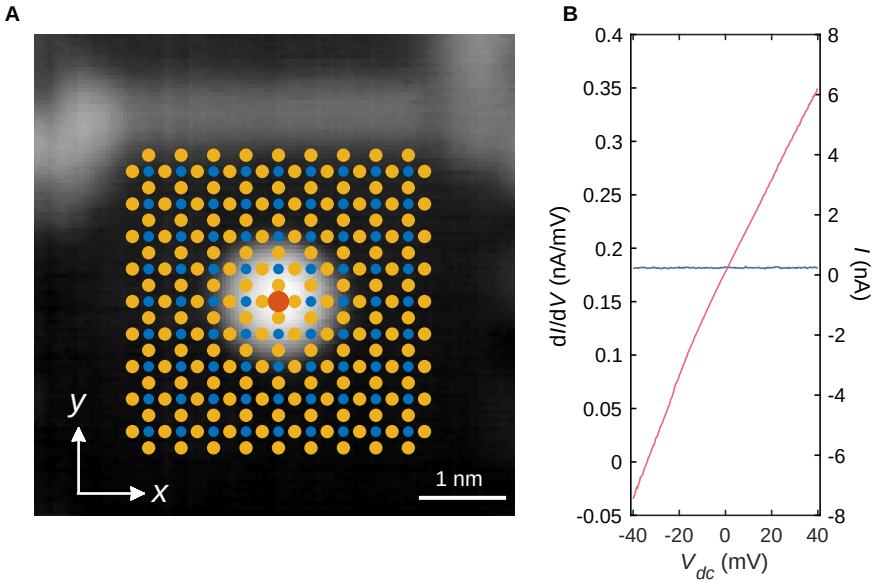

Figure 5.1. (**A**), Constant current topography of an Fe atom adsorbed on the N-site of Cu_2N (I_{set} = 100 pA, V_{set} = −100 mV, color scale from low (black) to high (white)). The overlay indicates N atoms (blue), Cu atoms (orange) and an Fe atom (red). (**B**), Current (red), and spectrum (blue) of the Fe atom on the N-site measured with a non spin-polarized tip and an out-of-plane magnetic field. B_z = 0.5 T, V_{set} = 40 mV, I_{set} = 6 nA, T = 0.5 K.

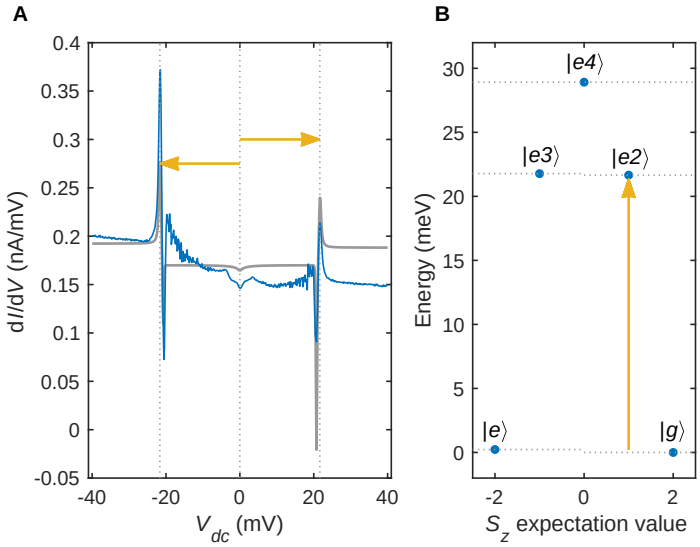

Figure 5.2. (**A**) Differential conductivity spectrum (blue) of the Fe atom on the nitrogen site measured with a spin-polarized tip and an out-of-plane magnetic field of $B_z = 0.5$ T ($V_{set} = 40$ mV, $I_{set} = 6$ nA, $T = 0.5$ K). Grey curve is a fit using the spin Hamiltonian model (see Section 3.5). (**B**) Energy spectrum determined from the fit to the differential conductivity. The yellow arrow indicates the first allowed transition. Anisotropy Parameters: $B_2^0 = -2.4 \pm 0.05$ meV, $B_4^0 = 1.1 \pm 0.3$ neV, $B_4^4 = -0.9 \pm 0.2$ neV. Reproduced from [3].

is orders of magnitude slower than the switching which occurs for single atoms on the Cu sites, and is readily observable in real-time. This eliminates the need for neighboring atoms which slow-down the dynamics. Control of this stochastic switching, the induction of quantum stochastic resonance, as well as the onset of a semi-classical crossover regime is the subject of this chapter. The following sections were adapted from our Science Advances publication [3].

5.2. SPIN-POLARIZED DIFFERENTIAL CONDUCTIVITY SPECTRUM

As the N-site adsorption site is meta-stable, Fe atoms are rarely found on this site directly after deposition. An Fe atom adsorbed on a Cu-site however, can be picked up and placed on the N-site (Figure 5.1) using vertical atom manipulation [4] with a Pt/Ir tip. The N-site yields a larger apparent height compared to the Cu-site (which itself can be occupied by hopping the atom in the four different directions defined by the crystal symmetry using a small voltage pulse). We obtain a spin-polarized

STM tip by picking up a cluster of Fe atoms, around 3-5. The magnetic field is applied along the out-of-plane direction, parallel to the easy-axis [5] of the N-site Fe atom.

In contrast to the non-spin-polarized spectra, the $\mathrm{d}I/\mathrm{d}V$ spectra recorded with a spin-polarized tip (Figure 5.2A) reveal an excitation localized at 21 mV that is affected by the applied magnetic field. Just below 21 mV an initial lowering of the conductance is observed followed by a sharp peak for larger bias magnitude. Modelling the spin using the spin-Hamiltonian formalism described in previous chapters yielded the state structure in Figure 5.2B. For the N-site Fe atom the symmetry of the binding site is four-fold, necessitating the use of higher order magnetic anisotropy, which we describe here using Stevens operators, rather than D and E. The Hamiltonian is then:

$$\hat{H} = B_2^0 \hat{O}_2^0 + B_4^0 \hat{O}_4^0 + B_4^4 \hat{O}_4^4 + g\mu_B \hat{\boldsymbol{S}} \cdot \boldsymbol{B}, \tag{5.1}$$

where $\hat{O}_k^q$ are the Stevens operators and B_p^q are their associated coefficients. The feature at 21 mV can be attributed to spin pumping into a long-lived excited state $|e2\rangle$ (the lifetime is roughly on the order of the tunnel current, in the tens of picoseconds). This occurs at 21 mV because allowed transitions ($m = \pm 1$) can be performed by scattering with tunnel electrons, and the tunnel rate is comparable to the time this state is occupied. Between 5 mV and 20 mV increased current noise is observed in the spectrum. This noise results from stochastic switching of the Fe atom's magnetic moment induced by tunneling of the magnetization between excited $|e\rangle$ and ground state $|g\rangle$ that can occur below the excitation threshold. It appears as noise in the spectrum because the millisecond switching is on a timescale comparable to that of the measurement time for each point in the spectrum. The noise is the primary aspect of interest, as it can provide a platform for stochastic resonance.

5.3. DYNAMIC RESPONSE TO STATIC VOLTAGE

First, we characterize this sub-threshold excitation mechanism by performing real-time measurements of the response of the atom's spin states to a static bias voltage V_{dc} (Figure 5.3). The Fe atom on the four-fold symmetric N-site (Figure 5.1A) has millisecond spin lifetimes when the magnetic field is applied along the spin's easy axis and it switches spontaneously between two spin states [1, 2, 6–8]. These states can be distinguished with a spin-polarized tip as the tip-atom conductance is spin-dependent due to tunneling magnetoresistance [9]. As such, time traces of the tunnel current at fixed tip-sample distance yield real-time observations of the spin state. These slow spin transitions enable real-time resolution which is typically not possible for individual magnetic atoms on surfaces. They show frequent transitions between two states that occur at voltages significantly below the first inelastic excitation threshold (21 mV), consistent with a classically forbidden transition across the magnetic anisotropy barrier.

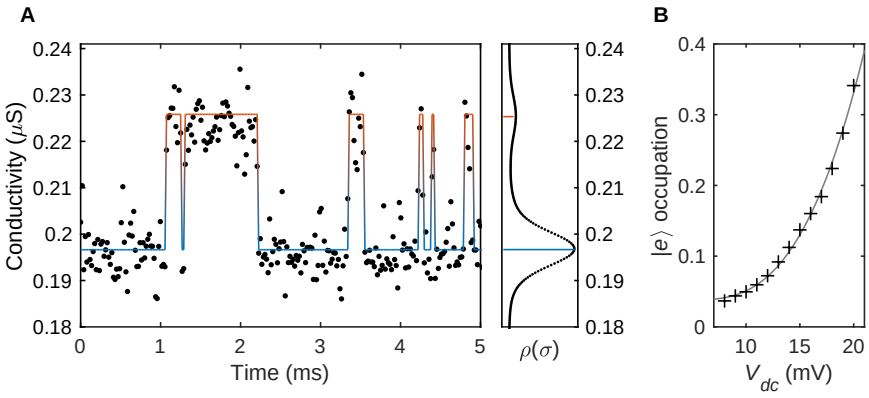

Figure 5.3. (**A**) Telegraph noise of the conductance (black points) observed when applying a constant bias voltage (V_{dc} = 15 mV) between tip and sample. The corresponding spin state is indicated by a solid line ($|g\rangle$ blue to $|e\rangle$ red). Right panel: histogram of the conductance. (**B**) Average occupation of the excited spin state as a function of V_{dc}; measured (crosses) and fit by a power law function (solid line). B_z = 0.5 T, V_{set} = 15 mV, I_{set} = 3 nA, T = 0.5 K. Reproduced from [3].

The voltage dependence of the excited state occupation, n_e, was fit using a power law of the form:

$$n_e = m(x - x_0)^{\alpha} + k, \tag{5.2}$$

x_0 defines the onset of the non-linear response, α gives the strength of the effect, and k is the occupation for low voltages. The exponent of a power law fit $\alpha = 2.9 \pm 0.2$ indicates that higher energy states contribute significantly to the excitation mechanism [10, 11]. Analogously to non-linear optics experiments, the exponent can roughly indicate the number of participating particles per excitation. This strongly non-linear avenue of controlling the atom's spin transition rates using the externally applied voltage provides an alternative means to drive the stochastic resonance.

5.4. MEASURING THE DYNAMIC RESPONSE

In the preceding chapters, we modulated the relative positions of the spin-states in energy by using a time-dependent exchange field applied via a spin-polarized tip. The voltage sensitivity of transitions in the Fe atom presents the opportunity to modulate the transition rates themselves, rather than the state's relative alignment, a predicted mode of inducing quantum stochastic resonance [12].

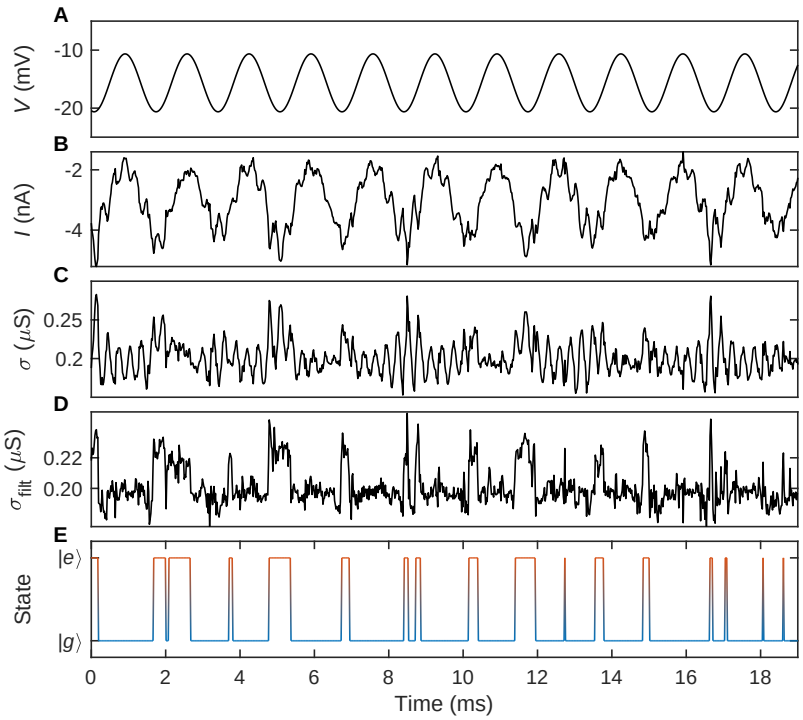

Figure 5.4. Spin state acquisition method for the N-site Fe atom. (**A**) Measured voltage applied to the spin. (**B**) Measured current flowing through the spin. (**C**) Calculated demodulated conductivity. (**D**) Conductivity with noise-whitening algorithm applied. (**E**) Time-dependent spin-state (blue to red) extracted using a Schmitt-trigger function. $\omega = 600$ Hz $V_{ac} = 5$ mV, $V_{dc} = 15$ mV, $V_{set} = 15$ mV, $I_{set} = 3$ nA, $B_z = 0.5$ T, $T = 0.5$ K.

Figure 5.4 shows how the time traces were measured for the N-site Fe atom. The conductivity of the junction is fixed before the measurement, by first applying $V_{set} = -15$ mV and allowing the feedback loop to settle with a current setpoint of $I_{set} = 3$ nA. This yields a junction conductivity of $\sigma = |\frac{I_{set}}{V_{set}}| = 0.2\ \frac{\text{nA}}{\text{mV}}$, after which the feedback loop is disengaged. The modulation voltage and the resulting current are then simultaneously measured using a 52 kHz sample rate analog to digital converter (ADC). The measured data is in Figure 5.4A and B. Panel A is a measurement of the modulation source, in this case an oscillating voltage applied directly to the sample, with $V_{dc} = -15$ mV [1] and $V_{ac} = 5$ mV. The resulting measured current is shown in Panel B. The most prominent effect that can be seen in the current is a time-dependent modulation, corresponding to the frequency of the applied voltage. On top of this linear response to the voltage, there are also higher frequency oscillations and short transient responses visible. Measurements without modulation applied, such as the trace shown in Figure 5.3, show that for an applied voltage of 15 mV the excited state lifetime is significantly shorter than that of the ground state. This allows the conductivity with the modulation applied to be well approximated as constant, and equal to that measured without the modulation. This conductivity can simply be multiplied by the measured voltage, and then subtracted from the measured current, yielding the trace shown in Panel C, the demodulated conductivity.

After applying demodulation, there are still both high frequency signals and low frequency modulations to contend with. Because the noise evolves on a similar time-scale to the spin-switching a low-pass filter would distort the spin signal, necessitating a more sophisticated noise removal method. We use a technique analogous to what is referred to in the professional audio sphere as noise-whitening [13]. In audio applications, knowledge about background noise is used to allow its removal. The method applied here is similar, but involves knowledge about the signal that is being measured. Telegraph noise has a distinct signature in Fourier space [14], a broadband Lorentzian line-shape. By taking the Fourier transform of the trace in Panel C, shown in Figure 5.5, the narrow-band noise peaks can be distinguished from the broadband spin-switching response. By first fitting a Lorentzian line-shape to the spin-switching and removing it from the Fourier transform, an impulse response filter (IRF) can be generated which only removes the noise (Figure 5.5 inset). The noise has distinct origins, ranging from electrical noise introduced by electronic devices, vibration introduced by ambient sources to transient effects such as a door-slamming in the building, reflected in the many-featured shape of the convolution feature. The noise-whitening method is most effective at removing coherent vibrations, because they will appear more readily in the Fourier transform, compared to a transient response which will be removed by averaging. Applying this filter to the trace in Figure 5.4C yields the trace in Panel D, where the spin-state switching can now be readily measured.

[1] Note that in this chapter, in contrast with the previous two, V_{set} and V_{dc} are always equal

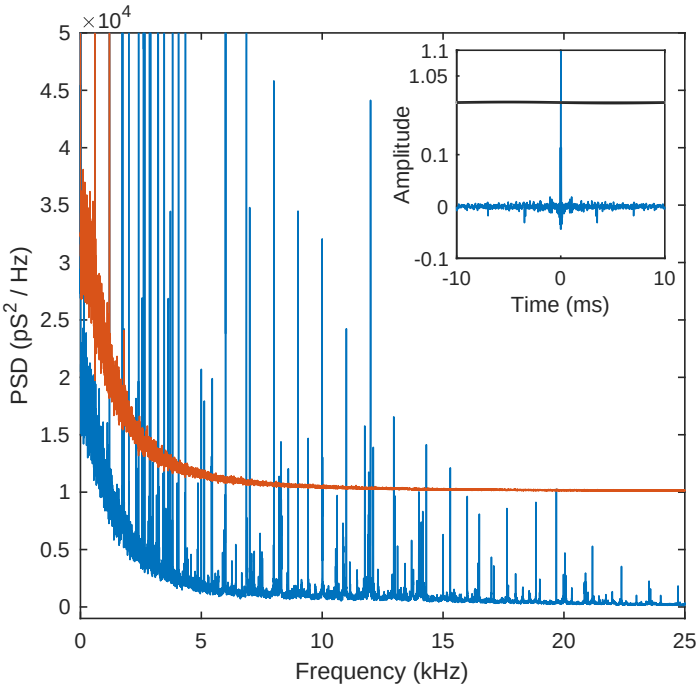

Figure 5.5. Power spectrum of the conductivity without filter applied (blue), and power spectrum of the resulting event trace after filtering and applying the Schmitt trigger thresholds (red). Offset for clarity. The inset shows the convolution filter used to remove instrument noise. $\omega = 600$ Hz $V_{ac} = 5$ mV, $V_{dc} = 15$ mV, $V_{set} = 15$ mV, $I_{set} = 3$ nA, $B_z = 0.5$ T, $T = 0.5$ K. Reproduced from [3].

The last step is to apply a Schmitt-trigger threshold function, with the threshold for excitation slightly below the higher current measured when the excited state is occupied, and the threshold for relaxation slightly above the lower current measured when the ground state is occupied. This threshold function allows the current trace to be converted into a binary trace which shows the time-dependent occupation of the ground and excited state, as shown in Figure 5.4E. Having established a method for extracting event traces from voltage-modulated traces, we can now proceed to investigate the dynamic response of the N-site Fe atom to harmonic voltages.

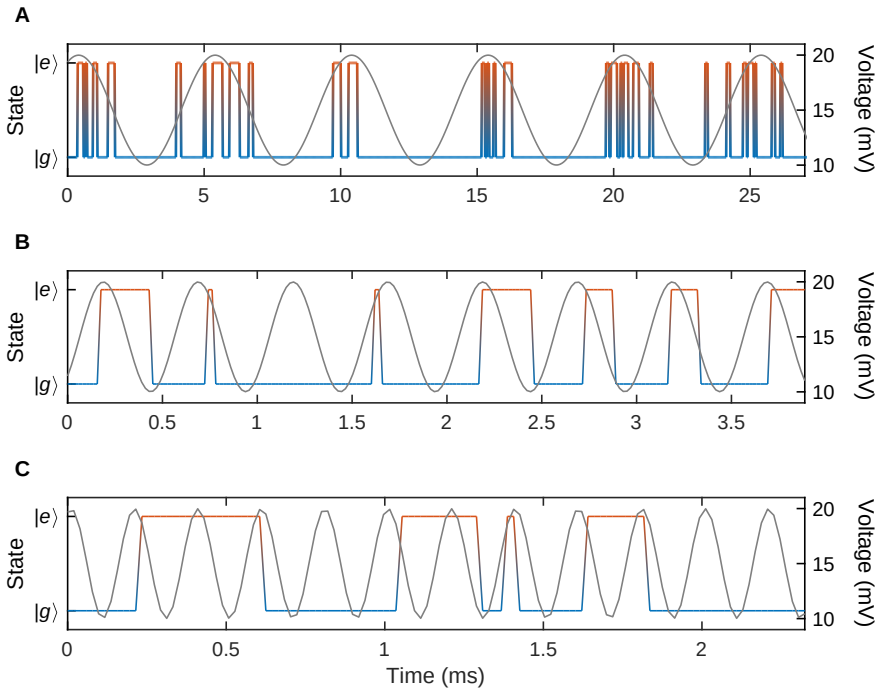

Figure 5.6. Measured time traces of the N-site Fe atom's spin state (blue to red) for different driving frequencies. (**A**) $\omega = 0.2$ kHz, (**B**) $\omega = 2$ kHz. (**C**) $\omega = 5$ kHz. The measured voltage is shown in grey. $V_{ac} = 5$ mV, $V_{dc} = 15$ mV, $V_{set} = 15$ mV, $I_{set} = 3$ nA, $B_z = 0.5$ T, $T = 0.5$ K. Reproduced from [3].

5.5. DYNAMIC RESPONSE TO HARMONIC VOLTAGE

We now introduce a harmonic drive voltage V_{ac} that modulates the excitation probability periodically in time. Figure 5.6 shows the spin state's response at three different drive frequencies, demonstrating that the switching can synchronize to the applied periodic drive, seen as the spin undergoing one cycle of excitation and relaxation in one period of the drive. This is most prominent at approximately 2 kHz (Panel B).

Stochastic resonance manifests in a profound modification of the switching statistics, which can be quantified by making a histogram (Figure 5.7A) of the times between excitations. With a static bias voltage applied (non-driven case), the counts exhibit a hypoexponential distribution, in agreement with the expectation of a non-resonant stochastic process governed by telegraph noise of two consecutive Poisson point processes (with Poisson-distributed excitation and relaxation processes with different characteristic times) [15]. With an $\omega = 2$ kHz $V_{ac} = 5$ mV drive signal added to the constant bias voltage (driven case), the counts peak at integer multiples of the excitation period $T_\omega = 0.5$ ms. The peak at T_ω is almost three times larger than the non-driven case, and counts for times above 1 ms are strongly suppressed. The transitions are now synchronized to the oscillating drive. As the counts deviate from a hypoexponential distribution, either the excitation or the relaxation (or both) are no longer Poisson distributed. Thus, driving fundamentally changes the dynamics of the spin.

The individual switching events in the time traces occur much faster than the time between successive spin state transitions, so it is reasonable to assume that the conditional probability of a transition out of a state, given that it is occupied, depends only on the instantaneous values of the drive voltages. Since spin correlations have extremely short lifetimes [8, 11, 16], we can consider that no correlations between spin and electron bath exist on the time-scale of the N-site Fe atom spin switching, therefore we model all transitions as Markovian, i.e., memoryless. In this Markovian limit transition-rate theory is applicable [17] and the theoretical methods used to characterize quantum SR in Ref. [12] can be generalized to calculate the switching time distribution nonperturbatively for any prescribed periodic time-dependence of the conditional probabilities [2]. Unlike in conventional stochastic resonance, the individual spin states could couple differently to their environment (tunneling-current and electron-spin scattering from the bath), which would effectively make the spin states experience different levels of noise. To account for this possibility, we model the excitation and relaxation rates separately.

We extract the conditional probabilities directly from the measured time traces by evaluating the probability to switch between spin states, relative to the drive cycle (Figure 5.7B). We find the relaxation rate to be constant, but the excitation rate is voltage-dependent and thus varies throughout the drive cycle. Relaxation is dom-

[2] For a full derivation see Chapter 2.

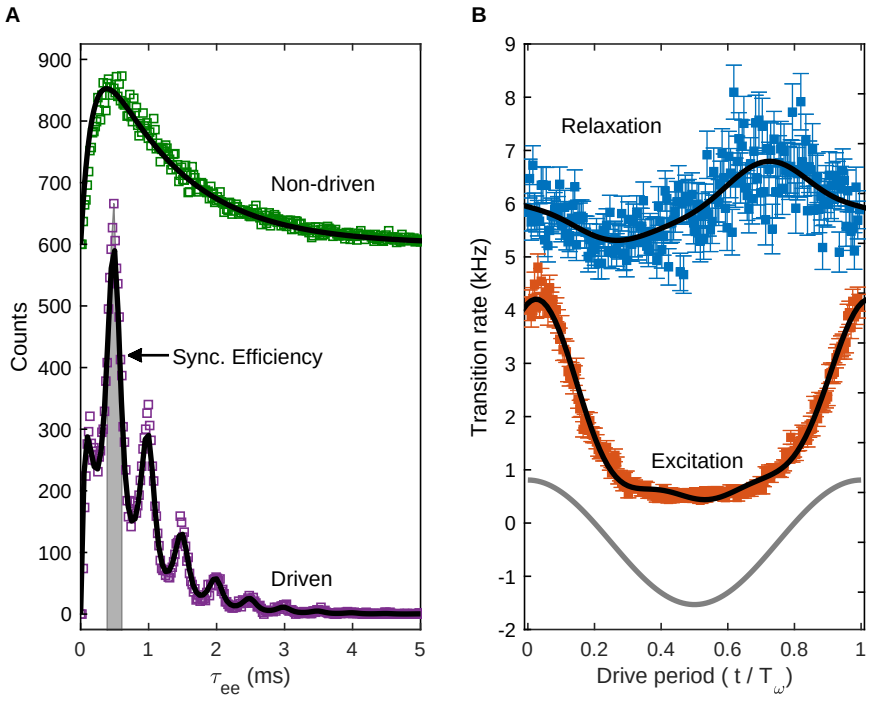

Figure 5.7. (**A**) Event histogram of τ_{ee} for a constant bias voltage (non-driven, green) and for a driving harmonic signal with $\omega = 2$ kHz (driven, purple). The ratio of grey shaded counts to total counts is the synchronization efficiency. The histogram for the constant bias voltage case is fit with a hypoexponential function (black, $\overline{\tau}_e = 0.17 \pm 0.01$ ms, $\overline{\tau}_g = 1.17 \pm 0.01$ ms, $c = 0.41 \pm 0.01$ counts·ms), while the histogram for the driven case was calculated analytically using the time-dependent transition rates (black). (**B**) Time-dependent excitation (red) and relaxation (blue) rates plotted over one period, the black line is the fit used as input to the SR model. The corresponding voltage is shown in grey. $T_\omega = 0.5$ ms, $V_{ac} = 5$ mV, $V_{dc} = 15$ mV, $V_{set} = 15$ mV, $I_{set} = 3$ nA, $B_z = 0.5$ T, $T = 0.5$ K. Reproduced from [3].

inated by scattering with bath electrons and therefore remains constant over one period of the drive, while excitation is mediated by voltage-dependent inelastic-electron tunneling from the tip via the Fe atom to the substrate. This is in contrast to the tip-modulation driven experiments in earlier chapters, where both the excitation and relaxation rate are significantly modulated by the drive.

With the relaxation and excitation rates as the only inputs and no fitting parameters, the theory quantitatively reproduces the experimentally obtained switching time distribution in Figure 5.7A (driven case, black curve). This confirms the prediction that stochastic resonance can be induced by modulating only one of the transition rates rather than the state energies [18] and demonstrates that the voltage-dependent synchronization of the Fe atom's dynamics is caused by quantum stochastic resonance.

5.6. SYNCHRONIZATION EFFICIENCY AND RESONANCE IN CONTROL PARAMETERS

The full frequency dependent event histograms are plotted as an image plot in Figure 5.8. The relative intensity of the harmonic peak (marked with a black dotted line) and the background demonstrate the degree of synchronization between the modulation and the spin switching. This plot clearly shows the broadband nature of stochastic resonance, a degree of synchronization is achieved over a majority of the measured frequencies, albeit with a varying efficiency. To quantify the synchronization of the Fe atom's spin to the harmonic drive, we define the synchronization efficiency as the number of counts in the harmonic peak in the switching time distribution normalized by the total number of counts (see gray area highlighted in Figure 5.7). The plot of synchronization efficiency versus frequency in Figure 5.9 has a prominent resonant peak centered at 1.4 kHz. Note that this peak arises solely from the statistics of the system, it does not rely on a resonator [19]. Looking at the histogram's in the inset of Figure 5.9, one can see the harmonic peak is very strong, almost overwhelming the broadband background. Not only can a voltage drive modulate the transition rates directly, it can in fact do so to such a degree that the synchronization is very efficient.

Investigating the resonance further, one can see that the modulation amplitude also has an effect on the synchronization efficiency. To quantify this effect, the frequency sweep was repeated for a series of V_{ac} ranging from 1 to 5 mV (Figure 5.10). Looking at the log-normal fits in Panel B, the peak frequency begins to exhibit an amplitude dependence at around 5 mV, before this it is relatively flat. The synchronization efficiency as a function of modulation amplitude peaks at 6 mV. There is a trade-off between increasing the synchronization efficiency by applying larger amplitude modulations, and shifting the resonance frequency away from the value set by the environmental noise due to the effectively larger noise power experienced by the atom. For the majority of measurements V_{ac} was fixed at 5 mV as a compromise which balances these two effects.

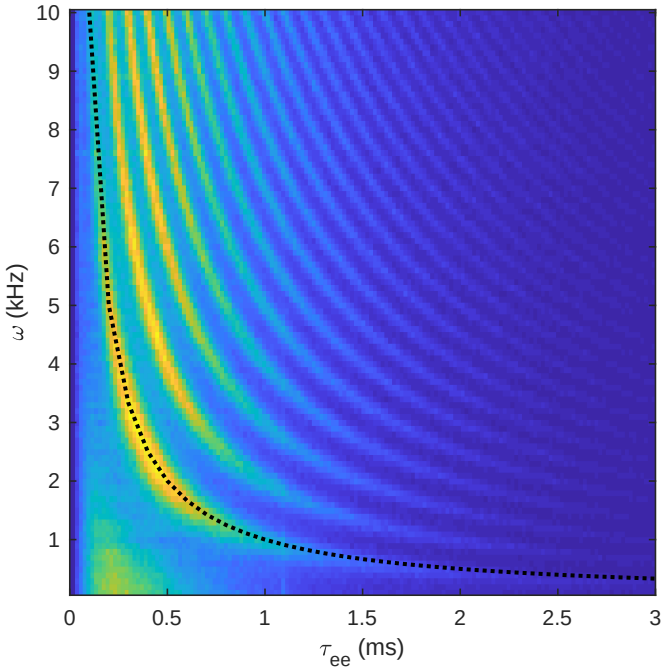

Figure 5.8. Image plot of τ_{ee} event histograms as a function of modulation frequency (the modulation period is marked with a black dotted line). V_{ac} = 5 mV, V_{dc} = 15 mV, V_{set} = 15 mV, I_{set} = 3 nA, B_z = 0.5 T, T = 0.5 K.

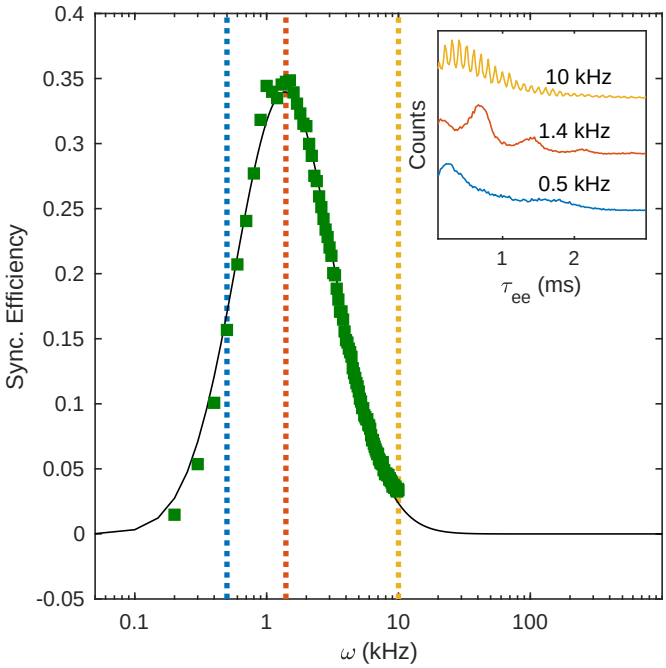

Figure 5.9. Synchronization efficiency (green) versus drive frequency, with a log-normal fit (black line, Equation 3.1 with $\omega_0 = 1.38 \pm 0.03$ kHz, $\sigma = 0.373 \pm 0.002$ $\log_{10}$·kHz, $c = 0.340 \pm 0.002$). Error bars are comparable to marker size. The inset shows the corresponding event histograms at the frequencies indicated by the vertical dotted lines. $T = 0.5$ K, $V_{set} = 15$ mV, $B_z = 500$ mT, $I_{set} = 3$ nA, $V_{ac} = 5$ mV. Reproduced from [3].

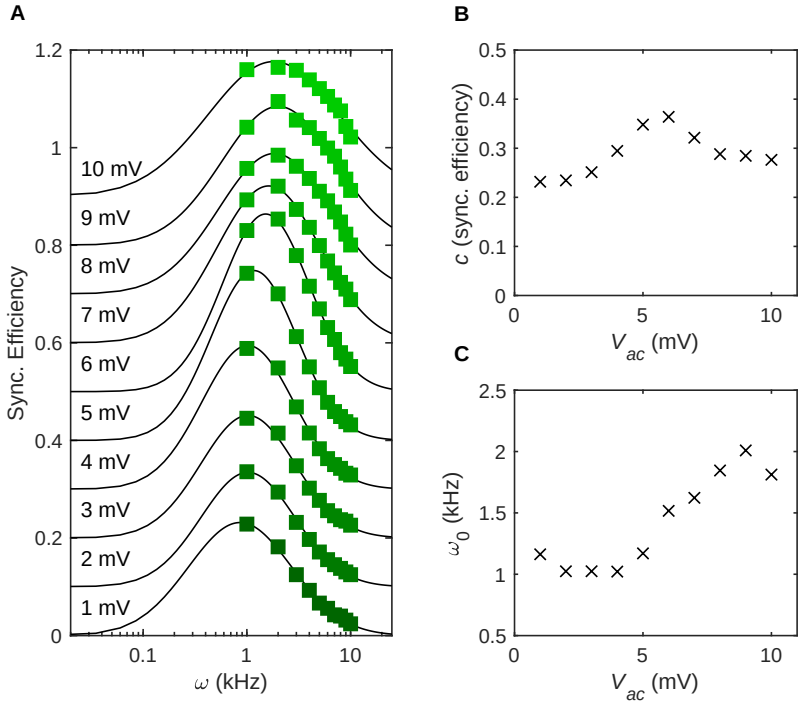

Figure 5.10. (**A**) Frequency dependent synchronization efficiency for varying V_{ac} (green, labels show V_{ac}). (**B**) Amplitude c of log-normal (Equation 3.1) fit to sync efficiency vs. V_{ac}. (**C**) Peak frequency ω_0 of log-normal fit to synchronization efficiency vs. V_{ac}. $V_{dc} = 15$ mV, $I_{set} = 3$ nA, $V_{set} = 15$ mV, $B_z = 500$ mT, $T = 0.5$ K.

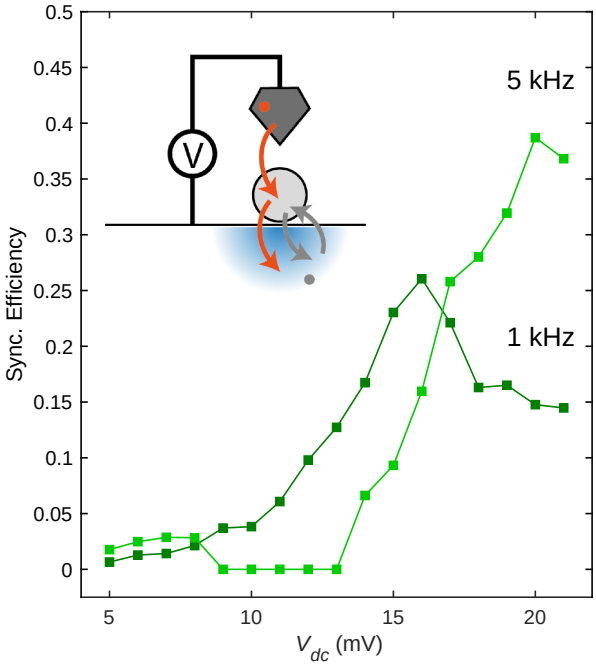

Figure 5.11. Synchronization efficiency versus V_{dc} for 1 and 5 kHz (green and light green markers, respectively). The inset shows a schematic description of the scattering process. $B_z = 500$ mT, $I_{set} = 3$ nA, $V_{ac} = 5$ mV. Reproduced from [3].

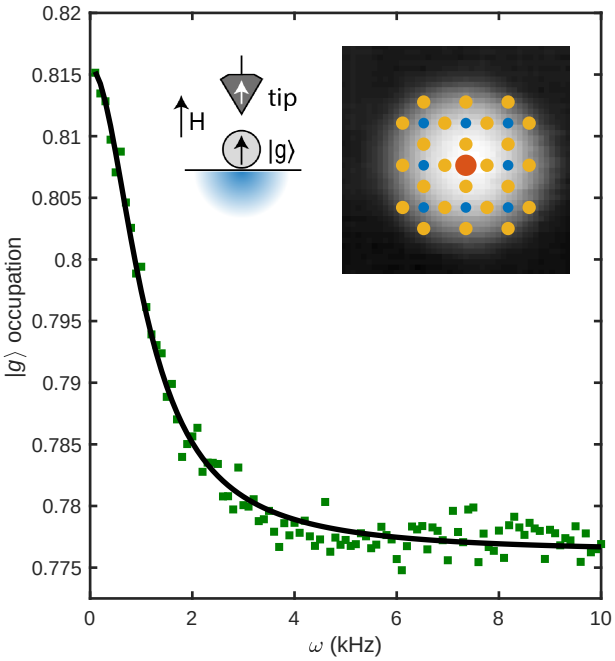

Figure 5.12. Average occupation of the nitrogen site atom's ground state as a function of the driving frequency along with a Lorentzian fit (black line, $\Gamma = 1.08 \pm 0.03$ kHz, $L = 4 \pm 1$ Hz, $L_0 = 0.776 \pm 0.001$), $B_z = 500$ mT. Inset shows a constant current topography acquired at $I_{set} = 100$ pA, $V_{set} = 100$ mV with a corresponding overlay of the atomic structure (Cu orange, N blue, and Fe red). Reproduced from [3].

An important characteristic of SR is its strong dependence on the timescale of the noise. In our experiment we can independently tune quantum noise by varying the electron tunneling with the tip, and thermal noise by increasing scattering with thermally excited bath electrons.

By sweeping the applied voltage V_{dc} at constant drive frequency (Figure 5.11), we tune the Fe atom's excitation rate from evolving slower than the drive to evolving faster. A clear maximum in synchronization efficiency is observed at 16 mV for a 1 kHz drive. Increasing the drive frequency to 5 kHz shifts the maximum to higher voltages.

Stochastic resonance actively modifies the ground state occupation as a function of drive frequency (Figure 5.12); the dependence is well-approximated by a Lorentzian line-shape centered at 0 Hz. Additionally, due to the difference in con-

ductance between the ground and excited state when observed with a spin-polarized tip the time averaged tunnel current directly maps the frequency dependent occupation n_g via the relation:

$$\overline{I} = \left[n_g \sigma_g(\eta) + (1 - n_g)\sigma_e(\eta) \right] V_{dc},$$

where V_{dc} is the bias voltage, η is the spin-polarization of the tip, and σ_g and σ_e are spin-polarization-dependent conductivities of the ground and excited states, respectively. This unlocks access to the stochastic dynamics of quantum spins that evolve at timescales faster than the real-time limit of the STM, which is explored in our science advances publication [3].

5.7. QUANTUM TO SEMI-CLASSICAL CROSSOVER

Keeping V_{dc} constant, and increasing the temperature, yields thresholding behavior (Figure 5.13). The synchronization efficiency remains constant for all measured frequencies up to 2.5 K. For temperatures beyond 2.5 K, with a 1 kHz drive the synchronization efficiency decreases with increasing temperature, at 2 kHz a maximum is found at 4.5 K, and at 5 kHz it continually increases over the observed temperature range.

This behavior is consistent with the crossover regime between quantum and semi-classical stochastic resonance, where thermal excitations and quantum tunneling become comparable. At low temperatures the stochastic resonance is generated by the quantum noise of electron tunneling for which the synchronization efficiency peaks at 1.4 kHz. Above 2.5 K thermally excited electrons begin to participate significantly in the scattering and increase the spin switching rate, moving the stochastic resonance away from its quantum limit.

5.8. CONCLUSION

The Fe atom on the four-fold symmetric nitrogen site was brought into stochastic resonance using a harmonic voltage applied with a spin-polarized STM tip, yielding a strong synchronization between spin state and drive. Rather than directly modulating the transition matrix element of the electron-spin scattering transitions as we did for the $2 \times 4 + 1$ and 1×5 structures, here we effectively modulate the noise intensity directly. The drive-frequency-dependent response for the single atom is similar to that observed for the other structures, with synchronization increasing up to a critical value, and then de-synchronizing. Here, the voltage-driven time-dependent transition rates were used to model the switching time distributions using the transition rate theory established in Chapter 2. The agreement

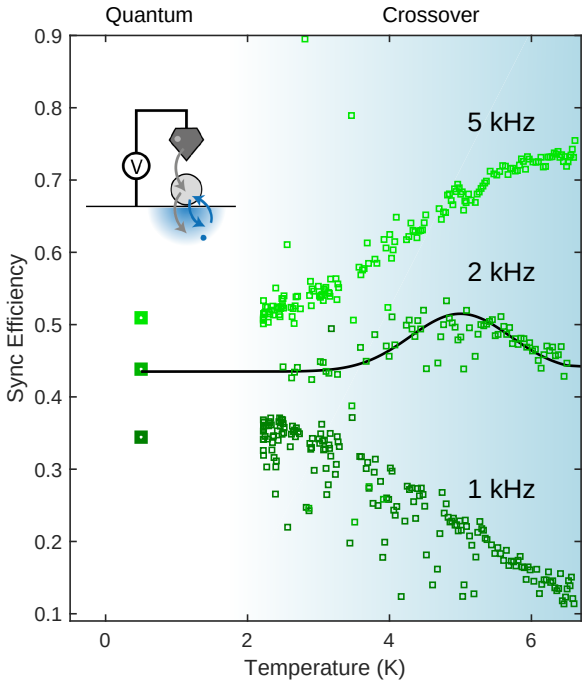

Figure 5.13. Synchronization efficiency versus temperature for 1, 2, and 5 kHz (dark green, green and light green markers, respectively; offset for clarity). The inset shows the relevant scattering process. The color gradient indicates the crossover from quantum to semiclassical stochastic resonance. The black line is a guide to the eye. $B_z = 500$ mT, $I_{set} = 3$ nA, $V_{ac} = 5$ mV, $V_{set} = 15$ mV. Reproduced from [3].

between the model and the measurement was excellent, indicating that the transitions are Markovian, and confirming the noise-intensity modulation as a viable path to stochastic resonance.

The temperature dependence measured in this chapter is distinctly different from that of the $2 \times 4 + 1$ explored in Chapter 3. The N-site Fe atom exhibits an initial regime of pure quantum character, where the dynamics are effectively temperature agnostic. This contrasts with the $2 \times 4 + 1$ structure, in which the stochastic resonance was found to follow to Arrhenius law, and is therefore strongly temperature dependent. Above 3 K temperature the stochastic resonance on the N-site Fe atom develops a temperature dependence, indicating that classical transitions similar to those observed on the $2 \times 4 + 1$ become the stronger noise source. This demonstrates that the N-site Fe atom can be tuned to either transition due to purely quantum noise, or to transition in a regime where both the classical noise source presented by the bath and the pure quantum tunneling noise compete.

The transition with the most clear quantum character is the relaxation, which is drive independent. Rather than randomizing the spin state at specific points in time, as in the 1×5, here the randomization effect is present throughout the entire drive cycle. The initial theory of quantum stochastic resonance put forth by Löfstedt and Coppersmith [18] predicts that stochastic can occur in a quantum system even if only a single rate is modulated, the measurements on the N-site Fe confirm this prediction experimentally.

REFERENCES

[1] T. Choi and J. A. Gupta, *Building blocks for studies of nanoscale magnetism: adsorbates on ultrathin insulating Cu_2N,* Journal of Physics: Condensed Matter **26**, 394009 (2014).

[2] R. Rejali, D. Coffey, J. Gobeil, J. W. González, F. Delgado, and A. F. Otte, *Complete reversal of the atomic unquenched orbital moment by a single electron,* npj Quantum Materials **5**, 1 (2020).

[3] M. Hänze, G. McMurtrie, S. Baumann, L. Malavolti, S. N. Coppersmith, and S. Loth, *Quantum stochastic resonance of individual Fe atoms,* Science Advances **7** (2021).

[4] D. M. Eigler and E. K. Schweizer, *Positioning single atoms with a scanning tunnelling microscope,* Nature **344**, 524 (1990).

[5] D. Gatteschi, R. Sessoli, and J. Villain, *Mesoscopic Physics and Nanotechnology* (Oxford University Press, Oxford, 2006).

[6] F. Donati, S. Rusponi, S. Stepanow, C. Wäckerlin, A. Singha, L. Persichetti, R. Baltic, K. Diller, F. Patthey, E. Fernandes, J. Dreiser, Šljivančanin, K. Kum-

mer, C. Nistor, P. Gambardella, and H. Brune, *Magnetic remanence in single atoms,* Science **352**, 318 (2016).

[7] W. Paul, K. Yang, S. Baumann, N. Romming, T. Choi, C. P. Lutz, and A. J. Heinrich, *Control of the millisecond spin lifetime of an electrically probed atom,* Nature Physics **13**, 403 (2016).

[8] J. Hermenau, M. Ternes, M. Steinbrecher, R. Wiesendanger, and J. Wiebe, *Long Spin-Relaxation Times in a Transition-Metal Atom in Direct Contact to a Metal Substrate,* Nano Letters **18**, 1978 (2018).

[9] R. Wiesendanger, H.-J. Güntherodt, G. Güntherodt, R. J. Gambino, and R. Ruf, *Observation of vacuum tunneling of spin-polarized electrons with the scanning tunneling microscope,* Physical Review Letters **65**, 247 (1990).

[10] S. Rolf-Pissarczyk, S. Yan, L. Malavolti, J. A. J. Burgess, G. McMurtrie, and S. Loth, *Dynamical Negative Differential Resistance in Antiferromagnetically Coupled Few-Atom Spin Chains,* Physical Review Letters **119**, 217201 (2017).

[11] M. Ternes, *Spin excitations and correlations in scanning tunneling spectroscopy,* New Journal of Physics **17**, 63016 (2015).

[12] R. Löfstedt and S. N. Coppersmith, *Quantum stochastic resonance,* Physical Review Letters **72**, 1947 (1994).

[13] S. M. Kuo and D. R. Morgan, *Active noise control: a tutorial review,* Proceedings of the IEEE **87**, 943 (1999).

[14] S. Machlup, *Noise in Semiconductors: Spectrum of a Two-Parameter Random Signal,* Journal of Applied Physics **25**, 341 (1954).

[15] M. Albert, C. Flindt, and M. Büttiker, *Distributions of waiting times of dynamic single-electron emitters,* Physical Review Letters **107**, 1 (2011).

[16] S. Loth, C. P. Lutz, and A. J. Heinrich, *Spin-polarized spin excitation spectroscopy,* New Journal of Physics **12**, 125021 (2010).

[17] B. McNamara and K. Wiesenfeld, *Theory of stochastic resonance,* Physical Review A **39**, 4854 (1989).

[18] R. Löfstedt and S. N. Coppersmith, *Stochastic resonance: Nonperturbative calculation of power spectra and residence-time distributions,* Physical Review E **49** (1994).

[19] L. Gammaitoni, F. Marchesoni, and S. Santucci, *Stochastic Resonance as a Bona Fide Resonance,* Physical Review Letters **74**, 1052 (1995).

6

CONCLUSION

This work investigated tailored open quantum systems through the lens of stochastic resonance. The scanning tunneling microscope allowed structures to be assembled, atom-by-atom, and individually addressed and measured. Two different pathways to stochastic resonance were explored, first the magnetic exchange field which modulated the relative positions of the structures' spin states in energy, and second the bias voltage which directly modulated the transitions rates. The pivotal role played by noise in inducing stochastic resonance allows the system's resonant behavior to be used to identify the dominant noise sources and elucidate their character. Competition between quantum noise sources such as quantum tunneling, and classical noise sources like scattering with a thermal bath, traced the onset and evolution of quantum behavior.

We used Fe atoms to build three magnetic nanostructures that feature different stochastic behavior caused by their size and by their coupling to the bath electrons of the Cu substrate. The largest nanostructure, referred to as the $2 \times 4 + 1$, is an antiferromagnetic array four atoms wide and two atoms tall with an additional atom to give a net magnetic moment. It made clear how classical behavior can arise even in a few-atom nanostructure, and demonstrated how a dynamic exchange field can synchronize spin state evolution. The structure underwent classical stochastic resonance, with a significant synchronization between the drive and the time-dependent spin state. The temperature-dependent noise-synchronized dynamics indicated thermally-activated transitions across a barrier as the dominant noise source. Transitions via nearby low-energy states lowered the effective barrier height, demonstrating how discrete quantum states can still yield effectively classical behavior. As transitions only occurred over a barrier, we concluded this structure is exclusively classical.

The second magnetic structure, referred to as the 1×5, is a linear chain of five Fe atoms. It was subject to both classical and quantum noise, and demonstrated how stochastic resonance can interact with multiple noise sources simultaneously. The tip-induced exchange field synchronized this structure's dynamics, exposing both classical and quantum features. There were two possible pathways for transitions, either thermally activated transitions over a barrier, or direct temperature-independent transitions through the barrier. The former is classical behavior, while the latter is distinctly quantum. When the states had a larger energy separation, the classical thermal pathway drove the transitions, whereas direct quantum transitions dominated when the states were close to degenerate.

Lastly, an individual Fe atom was investigated in two different regimes, one in which quantum tunneling was the dominant noise source, and a second in which thermally excited bath-electrons participate significantly in the scattering. The atom was driven with a harmonic voltage, which modulates the noise power itself, rather than the transition matrix element. This alternate path to stochastic resonance yielded synchronization with quantum noise, namely magnetic tunneling, at temperatures below 2.5 K. Above this range, a second regime of synchronization was identified, where the drive cooperates with the classical noise presented by the thermal bath. This allowed a quantum to classical transition to be observed for a single spin.

The extension of the quantum stochastic resonance model to spins on surfaces in this work yielded a highly accurate method for modelling stochastic spin dynamics. We were able to model the spin dynamics in both classical and quantum regimes, and to explore the onset of resonant behavior. A spin Hamiltonian accounting for magnetic anisotropy and exchange interaction among the atoms was used to calculate the eigenstates of the nanostructures, yielding their relative energy as a function of magnetic field. Electron-spin scattering inducing transitions between the states were treated using perturbation theory. The resulting field-dependent transition rates could then be mapped to the measured transition rates by modelling the tip-induced exchange field. By asserting Markovian dynamics, transition rate theory was, in turn, used to calculate the distribution of times between excitations. The calculated distributions quantitatively reproduced the dynamic response of all three structures as they underwent stochastic resonance.

In summary, this thesis extended stochastic resonance to atomically small magnetic systems, not confined to just the classical world of paleontology and neurons, but also succeeding in synchronizing the dynamics of a single atom. So where do we go from here? Although not discussed extensively in this work, stochastic resonance can be used as a highly selective spectroscopic tool. The high frequency spin dynamics in [1] demonstrate this concept using both the picosecond-scale dynamics of a single Fe atom and the collective nanosecond-scale dynamics of a two-Fe-atom dimer. Pushing this further, we have already carried out preliminary work on resolving different regimes of intra-structure dynamics in larger nanostructures.

Moving beyond spins, preserving repeatable dynamics in the face of random noise is a wide-spread goal in both science and engineering. Biological systems in particular have developed a high-degree of noise robustness. The omnipresence of stochastic resonance across length and time scales, from the geological to the quantum, points to the fundamental role it plays in making the stochastic more predictable.

REFERENCES

[1] M. Hänze, G. McMurtrie, S. Baumann, L. Malavolti, S. N. Coppersmith, and S. Loth, *Quantum stochastic resonance of individual Fe atoms,* Science Advances **7** (2021).

ACKNOWLEDGEMENTS

First, I thank my supervisor Sebastian Loth. He has been pivotal in my development both professionally and personally; I would not be the scientist I am today without him.

Next, I thank Max Hänze, for being an excellent collaborator and mentor over the past years, and for the critical role he played in the design and execution of all the experiments in this work. I thank Susanne Coppersmith, for opening the door to a true understanding of stochastic resonance with her help in extending the stochastic resonance model to quantum spins. I thank Susanne Baumann for her excellent scientific discussions and feedback, as well as both present and past members of the Loth group: Luigi Malavolti, Mohamad Abdo, Lukas Arnhold, Nicolaj Betz, Jacob Burgess, Steffen Rolf-Pissarczyk, Mahdieh Schmidt, Shaoxiang Sheng, Michael Schäfer, Stephan Spieker and Shichao Yan.

I am also indebted to my family and friends for their constant support over these last years, and extend my gratitude to them all.

A

SAMPLE GROWTH AND PREPARATION

The experiment was performed in a sub-Kelvin Unisoku ^{3}He vector magnetic field ((2,2,9) T) STM, model USM 1300 ^{3}He. The sample preparation was done in ultra-high vacuum, where we prepared a Cu(100) single crystal with repeated Ar+ sputtering (ion energy of 1 keV) and annealing (850 K) cycles. A monolayer of Cu_2N [1] was grown by N_2 sputtering (ion energy of 1 keV) at an N_2 partial pressure of 5×10^{-6} mbar and consecutive annealing to 600 K. The sample was pre-cooled to approximately 20 K and Fe atoms were deposited by positioning the cold sample in a low flux of Fe vapor from a Knudsen cell for 8 seconds.

REFERENCES

[1] C. F. Hirjibehedin, C.-y. Lin, A. F. Otte, M. Ternes, C. P. Lutz, B. A. Jones, and A. J. Heinrich, *Large Magnetic Anisotropy of a Single Atomic Spin Embedded in a Surface Molecular Network,* Science **317**, 1199 (2007).

CURRICULUM VITÆ

GREGORY MCMURTRIE
Bodoweg 12, 70327 Stuttgart, Germany
Email: gregorymcmurtrie@gmail.com, Phone: (+49) 173 667-5917

skills

- **Experiment Design** – Mechanical (Solidworks, Inventor) and electrical (Qucs) design under tight constraints (1e-12 mBar vacuum, 9 T magnetic field, temperature <100 mK, low noise, EM frequencies up to 20 GHz).
- **Analytics** – Noise mitigation techniques, predictive modelling, time-series analysis, instrument calibration, handling noisy and incomplete data, efficient parallelized simulation, natural language processing (hobbyist).
- **Programming** –Extensive simulations and analysis in MATLAB, experiment automation and scripting in LabView, UX design, software architecture development, automation in Python, version control (Git, SVN).
- **Languages** – English (native), Spanish (native), German (proficient, C1 equivalent 17/20 testDAF).
- **Public Speaking** – Presented at over 20 conferences in: Canada, Germany, Italy, Korea, Netherlands, and Spain.

experience

2017 - 2021 **UNIVERSITY OF STUTTGART – Research Assistant** **STUTTGART, DE**

- Developed a modular automatization architecture for time-resolved atomic-scale experiments which reduced the turn-around between brainstorming and measurement from 2-3 months to under a week, as well as significantly reducing opportunities for user error, increasing efficiency, and mitigating down-time.
- Created a software suite for iterative reporting during dynamic quantum magnetism measurements, combining MATLAB and C to identify critical events in noisy data by applying both signal processing techniques (convolution filtering, dynamic thresholding, noise whitening), and physical models (Monte Carlo, stochastic dynamics).
- Led the information technology infrastructure design and procurement, deploying both hardware and software solutions for a team of 20 scientists working in quantum technology and sensing research.

2015-2017 **MAX PLANCK INSTITUTE FOR SOLID STATE PHYSICS – Research Assistant** **HAMBURG, DE**

- Synchronized the stochastic response of a single atom's dynamic magnetism to a microwave frequency voltage source, yielding a mechanism for controlling quantum objects that was previously only a theoretical prediction.
- Increased the performance of a €2M state-of-the-art microscope by an order of magnitude, through optimization of both the analog signal path (filtering, relays, mixing) and digital signal generation (reducing aliasing, increasing signal to noise, pre-compensating for frequency dependent response) in the GHz regime.

2010 - 2014 **UNIVERSITY OF BRITISH COLUMBIA – Research Assistant** **VANCOUVER, BC**

- Built and commissioned a microsecond-precise molecular beam epitaxy system for the growth of technologically-relevant advanced materials such as superconductors, topological insulators, and correlated electron systems.
- Designed and assembled a fully automated graphene growth system, significantly improving available sample quality, and leading to the development of novel solar cells using graphene.

education

2017 - 2021 **DOCTORATE OF PHILOSOPHY – PHYSICS - UNIVERSITY OF STUTTGART** **STUTTGART, DE**

- Developed novel methods for investigating magnetic nanostructures at the atomic length and picosecond time scale, unraveling the transition between classical and quantum behavior, co-authored 4 peer-reviewed publications.
- Co-founded the "Brunch Talks" program to facilitate interdisciplinary university-wide collaboration (~50 academics) as lead PhD student representative in the Integrated Quantum Science and Technology graduate school.
- Wrote and presented a guest-lecture series in German on fluid mechanics, teaching over 400 undergraduate students with both experimental and theoretical approaches (received extensive positive feedback in end of year comments).

2015 - 2017 **MASTERS OF SCIENCE – PHYSICS - UNIVERSITY OF HAMBURG** **HAMBURG, DE**

- Graduated with distinction (maximum grade), focus in Condensed Matter and Optics.
- Awarded €15,000 International Max Planck Research School for Condensed Matter Science stipend.

2010 – 2014 **BACHELOR OF SCIENCE – PHYSICS - UNIVERSITY OF BRITISH COLUMBIA** **VANCOUVER, BC**

- 81% (A) average over upper-level physics courses (88% Computational Physics, 90% Statistical Mechanics)
- Awarded "Best student oral presentation" at the undergraduate pacific physics and astronomy conference (300-400 participants) for research on novel graphene growth methods conducted during first year of university.

personal

- **Music Production:** Songwriting, synthesis, and sampling in Hip-Hop / Electronic / Pop genres.
- **Cooking:** Latin, SE Asian, and Korean cuisine with classical French sensibilities.
- **Powerlifting:** Hobbyist powerlifter, squat 170 kg.

List of Publications

4. **Max Hänze, Gregory McMurtrie[1], Susanne Baumann, Luigi Malavolti, Susan N. Coppersmith, and Sebastian Loth**, *Quantum stochastic resonance of individual Fe atoms,* Science Advances **7**, (2021).

3. **Luigi Malavolti, Gregory McMurtrie, Steffen Rolf-Pissarczyk, Shichao Yan, Jacob A. J. Burgess, and Sebastian Loth**, *Minimally invasive spin sensing with scanning tunneling microscopy,* Nanoscale **12**, (2020).

2. **Luigi Malavolti, Matteo Briganti, Max Hänze, Giulia Serrano, Irene Cimatti, Gregory McMurtrie, Edwige Otero, Philippe Ohresser, Federico Totti, Matteo Mannini, Roberta Sessoli, and Sebastian Loth**, *Tunable Spin-Superconductor Coupling of Spin 1/2 Vanadyl Phthalocyanine Molecules,* Nano Letters **18**, (2018).

1. **Steffen Rolf-Pissarczyk, Shichao Yan, Luigi Malavolti, Jacob A. J. Burgess, Gregory McMurtrie, and Sebastian Loth**, *Dynamical Negative Differential Resistance in Antiferromagnetically Coupled Few-Atom Spin Chains,* Physical Review Letters **119**, (2017).

[1] Co-first author.

ERKLÄRUNG

Schriftliche Bestätigung der eigenständig erbrachten Leistung gemäß § 6 Absatz 2 der Promotionsordnung der Universität Stuttgart
Die vorstehende, eingereichte Dissertation stellt meine eigenständig erbrachte Leistung dar. Ich habe ausschließlich die angegebenen Quellen und Hilfsmittel benutzt. Wörtlich oder inhaltlich aus anderen Werken übernommene Angaben habe ich als solche kenntlich gemacht. Die Richtigkeit der hier getätigten Angaben bestätige ich und versichere, nach bestem Wissen die Wahrheit erklärt zu haben.

Stuttgart, den _____ _____

Gregory McMurtrie